Final Report to the Department of Energy Inertial Confinement Fusion Team for the Period November 1, 1993 – October 30, 1997 on Contract No. DE-AS08-88DP10754

P. Cousseau, R. Engelstad, D.L. Henderson, D. Kaap, G.L. Kulcinski, J.J. MacFarlane, E.A. Mogahed, G.A. Moses, C. Nin, R.R. Peterson, J.F. Santarius, M. Sprague, I.N. Sviatoslavsky, P. Wang, P.P.H. Wilson

October 1997

UWFDM-1059

FUSION TECHNOLOGY INSTITUTE

UNIVERSITY OF WISCONSIN

MADISON WISCONSIN

Final Report to the Department of Energy Inertial Confinement Fusion Team for the Period November 1, 1993 – October 30, 1997 on Contract No. DE-AS08-88DP10754

P. Cousseau, R. Engelstad, D.L. Henderson, D. Kaap, G.L. Kulcinski, J.J. MacFarlane, E.A. Mogahed, G.A. Moses, C. Nin, R.R. Peterson, J.F. Santarius, M. Sprague, I.N. Sviatoslavsky, P. Wang, P.P.H. Wilson

Fusion Technology Institute
University of Wisconsin
1500 Engineering Drive
Madison, WI 53706

http://fti.neep.wisc.edu

October 1997

UWFDM-1059

Final Report to the Department of Energy Inertial Confinement Fusion Team for the Period November 1, 1993 - October 30, 1997 on Contract No. DE-AS08-88DP10754

P. Cousseau, R. Engelstad, D.L. Henderson, D. Kaap,
G.L. Kulcinski, J.J. MacFarlane, E.A. Mogahed, G.A. Moses,
C. Nin, R.R. Peterson, J.F. Santarius, M. Sprague,
I.N. Sviatoslavsky, P. Wang, P.P.H. Wilson

Fusion Technology Institute
University of Wisconsin-Madison
1500 Engineering Drive
Madison WI 53706

October 1997

UWFDM-1059

U.S. Department of Energy

Contract No. DE-AS08-88DP10754

The Development and Application of
Advanced Analytical Methods
to Commercial ICF Reactor Chambers

Task 1
Final Report

Multi-Dimensional Radiation Hydrodynamics Computer Code Development

Fusion Technology Institute
University of Wisconsin-Madison

1. Multi-Dimensional Radiation-Hydrodynamics Code Development

The effort to develop a multi-dimensional radiation hydrodynamics computer code with realistic equations of state and opacities has consisted of several activities:

- evaluate candidate programs,
- select one code for development,
- implement multiple materials,
- include multigroup frequency dependence, and
- add table lookup of detailed opacities and equations of state.

Starting with a survey of available hydrodynamics codes, both with and without radiation, we selected three for a more extensive evaluation: CTH, MACH2, and ZEUS-2D. These were run with some simple hydrodynamics test cases and, for MACH2 and ZEUS-2D, which have a rudimentary radiation hydrodynamics (RHD) capability, some simple RHD test cases. Based on several considerations, the ZEUS-2D code was chosen as the foundation of our 2-D radiation hydrodynamics code development effort.

2. Candidate Radiation Hydrodynamics Code Evaluation

The key considerations used in evaluating the three main candidate codes for our purposes are briefly summarized in Table 1.

The ZEUS-2D code was chosen for our development purposes because:

- ZEUS-2D already contained a simple (single frequency) radiation hydrodynamics capability, the extension of the algorithms to multiple frequencies is straightforward, and a ZEUS-3D version exists for both vector and parallel computers that we anticipate would expedite developing a 3-D RHD capability.
- CTH can be used for multiple materials and shock waves impacting structures, but it will be difficult to add radiation transport because it is coded with explicit numerical sweeps in alternating directions, while the radiation transport intrinsically requires an implicit solution.
- MACH2 contains rudimentary radiation diffusion and multi-material zones, but we judged it to be difficult to modify, and Lagrangian mesh tangling will be a serious issue for the types of 2-D calculations we need to run.

Table 1. Key Considerations for the Main Codes Evaluated for Development into a Two-Dimensional Radiation Hydrodynamics Code

	CTH	MACH2	ZEUS-2D & 3D
Main applications	Projectiles; explosives	Compact toroid MHD	Astrophysics
Originator	Sandia	Phillips Laboratory	NCSA (NSF)
Restrictions	Proprietary	Proprietary	Public Domain
Language	Fortran 77 and C	Fortran 77 and C	Fortran 77 and C
Radiation diffusion	No	Yes (cooling or optically thick)	Yes (2-D)
Multi-material	Yes	Yes, in distinct regions	No
Magnetic field	No	Yes	Yes
Eulerian or Lagrangian	Eulerian (Lagrangian step and remap)	Arbitrary Lagrangian Eulerian (ALE)	Eulerian
Numerical method	Explicit	Implicit (SOR)	Explicit hydro and transport; Implicit radiation diffusion (ICCG)
Mesh	1 block	Multiple blocks	Ragged boundary
Geometry	Rectangular (3-D) Cylindrical (2-D) Spherical (1-D)	Rectangular (2-D) Cylindrical (2-D)	Rectangular (3-D) Cylindrical (2-D) Spherical (2-D)

2.1. Testing the Unmodified ZEUS-2D Radiation Hydrodynamics Code Development Status

Having selected a code, some simple but relevant ZEUS-2D test cases were run at high energy density. These cases were:

1. Spherical and cylindrical explosions at high energy density,
2. Radiation impinging on a gold slab, and
3. Spherical and cylindrical explosions within hohlraums.

Our earliest attempts at running hohlraum cases experienced difficulty due to the time step dropping to very small values (10^{-30} s). This appeared to be due to the coupling of the target explosion with the wall, so we investigated the simpler problems of an isolated target explosion and of the slab-geometry interaction of radiation with a gold wall. By varying the zoning, profiles, initial conditions, and background conditions, each of these problems was successfully attacked. The problems were explored up to hohlraum-relevant energy densities. That is,

- High-energy-density cases were run for cylindrical and spherical target explosions in rectangular (x,y), cylindrical (r,z), and spherical (r,θ) geometry with
  - radiation energy density $\lesssim 10^{21}$ erg/cm^3, and
  - plasma energy density $\lesssim 2.5 \times 10^{16}$ erg/cm^3.
- Blackbody radiation diffusing through a gold slab was run with
  - radiation energy density $\lesssim 2 \times 10^{11}$ erg/cm^3, and
  - plasma energy density $\lesssim 4 \times 10^{14}$ erg/cm^3.

Attacking these problems separately allowed us to develop the experience and techniques necessary to run the combined problem of the hohlraum. Hohlraum cases were run, and results reported at the American Physical Society–Division of Plasma Physics meeting in Louisville, Kentucky, November 6-11, 1995. Based on these results, we began implementing various capabilities of the UW 1-D radiation hydrodynamics code, BUCKY, in ZEUS-2D.

3. ZEUS 2-D Radiation Hydrodynamics Code

The ZEUS-2D radiation-magnetohydrodynamics code [1, 2, 3] is being augmented to add the key capabilities of the University of Wisconsin's 1-D BUCKY code, including:

- Multiple materials,

- Multigroup frequency dependence,
- Table lookup of detailed opacities and equations of state.

ZEUS-2D is a two-dimensional, Eulerian-mesh code, written in covariant orthogonal coordinates and solved by finite differences with operator splitting into implicit source and explicit transport steps. The fundamental hydrodynamic equations can be solved alone or with magnetohydrodynamics, radiation, or both. The finite-difference mesh can be modified dynamically, although ZEUS-2D is not an adaptive-mesh code, and the mesh spacing can be varied independently in both dimensions.

The unmodified ZEUS-2D code has been tested on simple radiation diffusion, microexplosion, and hohlraum test problems, and it appears to be a suitable code upon which to base the desired modifications. Multiple materials have been implemented by including the solution of a separate equation of continuity for each species. The modifications to the difference equations required to add multigroup frequency dependence have been developed and tested in a small auxiliary code, and added to ZEUS-2D. The table lookup subroutines from the BUCKY code for equations of state and opacities have been merged with the ZEUS-2D code.

Testing of ZEUS-2D has proceeded in four independent areas:

1. multimaterial model
2. equation of state and opacity table lookup
3. multigroup radiation diffusion
4. hydrodynamics.

ZEUS has a recently added model that tracks the flow of different materials. The flow of different materials in ZEUS-2D is modeled by solving the advection problem separately for each material. The partial pressure in each zone for each material is calculated from the density of that material and the temperature in the zone. The total pressure is the sum of all the partial pressures in each zone. This is tested by running a standard problem in two ways. The problem, shown in Figures 1 and 2, is a shock driven by a mass density step. In one case, the mass is all a single material. In the other, a second material with identical properties replaces the first material in a region traversed by the shock. In the figures, the short dashed lines are the second material, the long dashes are the first material. The final total mass density profiles are compared, and the relative differences between the two calculations are found to be very small.

The use of realistic equations of state has been added to ZEUS-2D. This has been tested with a problem where temperature boundary conditions are applied to 2 planes bounding a slab and the temperature and densities are allowed to seek equilibrium. The ideal gas model in ZEUS-2D for one run, and the lookup of the same values in a table are used for the other. The results were essentially identical.

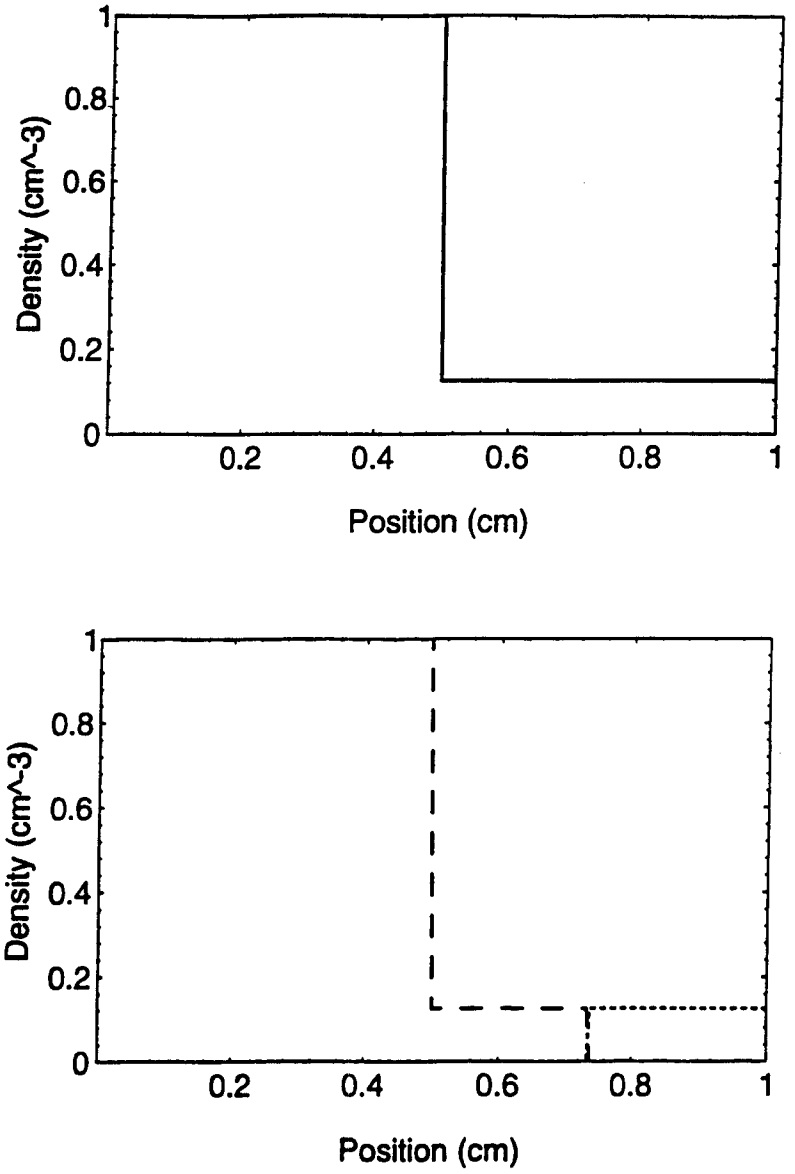

Figure 1. Initial condition of multimaterial test problem. The top figure is the mass density profile for a single material. The second figure shows the mass density split between two materials.

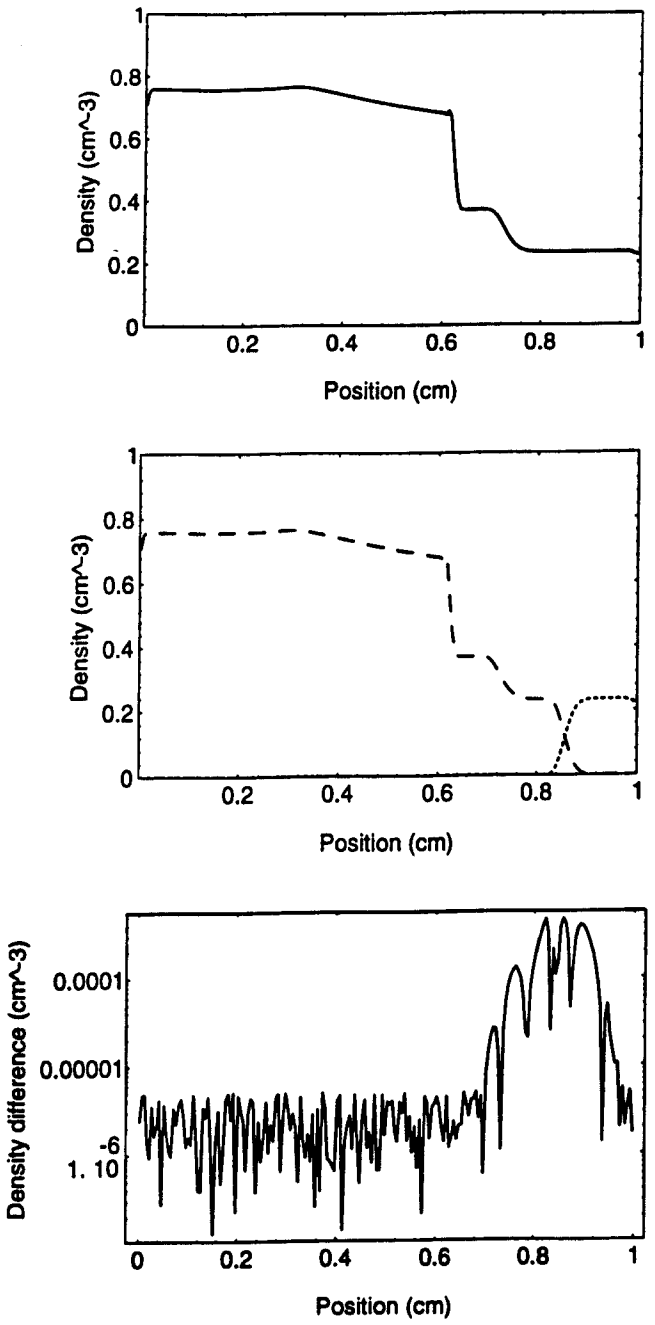

Figure 2. Condition of multimaterial test problem at time after the shock has passed into the second material. The top figure is the mass density profile for a single material. The second figure shows the mass density split between two materials. The bottom figure is the difference in total mass density between the two calculations.

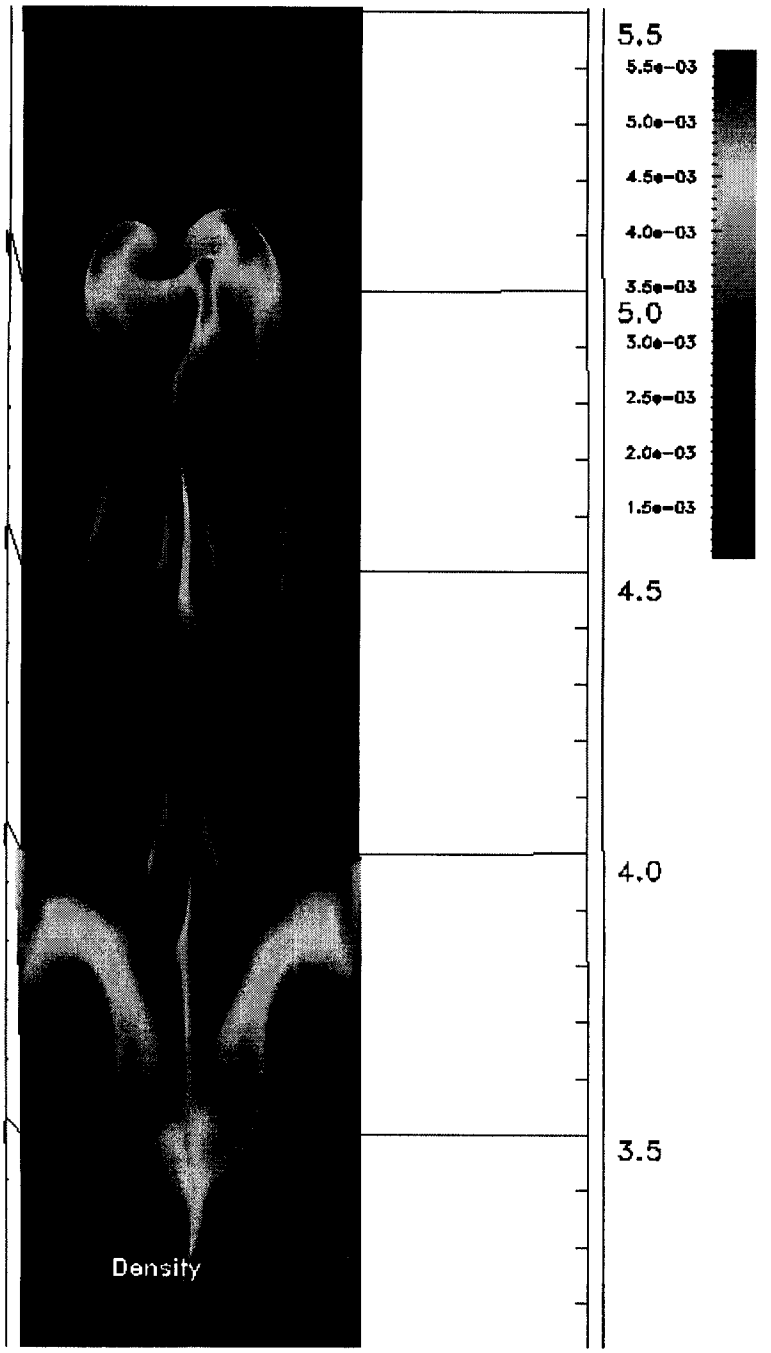

Figure 3. Density contours from ZEUS-2D simulation of shock driven Richtmyer-Meshkov instabilities in a liquid curtain.

The radiation transport via multigroup diffusion has been added to ZEUS-2D. It has been tested with a simple 1-D slab problem, with radiation energy density boundary conditions applied at two surfaces. The energy radiation density relaxes over time to a linear profile as it should.

The hydrodynamics of ZEUS-2D have been used in many astrophysical contexts. We have also tested the use of the code on pure hydrodynamic problems. We have gotten the expected results for hydrodynamic stability problems, where a shock is driven through a rippled high density curtain and becomes Richtmyer-Meshkov unstable. The results of such a simulation are shown in Figure 3. We have plans to perform simulations of shock tube experiments, with the multimaterial model and the table lookup of equations of state.

It has taken us much more effort to reach this stage than we originally thought, so we have just now started testing the code with integrated benchmarking. We have not been able to obtain results from the MULTI-2D code in Europe that are suitable for benchmarks. We have decided that it makes more sense to compare with experiments when they are available. Gold burnthrough experiments reported below have been used to benchmark the BUCKY code, so we are trying the same for ZEUS-2D. This will test hydrodynamics, radiation transport, and opacity lookups in an integrated way. At the time of this report, we have a bug in these calculations that is yet unresolved. We will report on these tests at a later date.

In summary, the status of the modifications to ZEUS-2D as of the writing of this report is that (1) multiple materials have been implemented and are working; (2) table lookup has been implemented, the data is properly being read by ZEUS-2D, and the interpolation routines are working; and (3) a relatively simple multigroup frequency algorithm has been implemented and is working with ideal equations of state. The main difficulty at present is that running the multigroup frequency version of ZEUS-2D with table lookup of the equations of state and opacities does not give results that benchmark with the well-tested BUCKY 1-D radiation hydrodynamics code. Present efforts are focused on resolving this difficulty and benchmarking the modified ZEUS-2D code against both BUCKY and experiments.

Acknowledgement

The bulk of this work was supported by Lawrence Livermore National Laboratory under contract # B310594. Part of the work done on the ZEUS code was supported by the U.S. Department of Energy on a separate contract. The debris damage experiments are being supported by Sandia National Laboratories.

References

[1] J.M. Stone and M.L. Norman, "ZEUS-2D: A Radiation Magnetohydrodynamics Code for Astrophysical Flows in Two Space Dimensions. I. The Hydrodynamic Algorithms and Tests," *Astrophysical J. Suppl.* **80**, 753 (1992).

[2] J.M. Stone and M.L. Norman, "ZEUS-2D: A Radiation Magnetohydrodynamics Code for Astrophysical Flows in Two Space Dimensions. II. The Magnetohydrodynamic Algorithms and Tests," *Astrophysical J. Suppl.* **80**, 791 (1992).

[3] J.M. Stone, D. Mihalas, and M.L. Norman, "ZEUS-2D: A Radiation Magnetohydrodynamics Code for Astrophysical Flows in Two Space Dimensions. III. The Radiation Hydrodynamic Algorithms and Tests," *Astrophysical J. Suppl.* **80**, 753 (1992).

U.S. Department of Energy

Contract No. DE-AS08-88DP10754

The Development and Application of
Advanced Analytical Methods
to Commercial ICF Reactor Chambers

Task 2
Final Report

2D Radiation-Hydrodynamics Code Development

Fusion Technology Institute
University of Wisconsin-Madison

THE BUCKY AND ZEUS-2D COMPUTER CODES FOR SIMULATING HIGH ENERGY DENSITY ICF PLASMAS

Robert R. Peterson, Joseph J. MacFarlane, John F. Santarius, Ping Wang, and Gregory A. Moses
Fusion Technology Institute, University of Wisconsin-Madison
1500 Engineering Drive
Madison, WI 53706-1687
(608) 263-5646

ABSTRACT

BUCKY and ZEUS-2D are two radiation hydrodynamics codes under development at the University of Wisconsin for the simulation of the behavior of high energy density plasmas found in ICF targets and target chambers. The ZEUS-2D code was originally developed at the National Center for Supercomputer Applications. BUCKY is a 1-D Lagrangian code which models many physical phenomena. Verification of these models in BUCKY with experiments is in progress. ZEUS-2D is a 2-D Eulerian radiation magnetohydrodynamics code written for astrophysical applications. It contains relatively simple radiation physics models which are being enhanced by implementing models from the BUCKY code.

I. INTRODUCTION

This paper describes the present state of ICF radiation hydrodynamics code development at the University of Wisconsin. Computer codes for the study of ICF plasma physics and radiation transport have been under development at the University of Wisconsin for about twenty years. Presently, two radiation hydrodynamic computer codes and an atomic physics code are being used, maintained and improved upon. BUCKY[1] is a 1-D radiation-hydrodynamics computer code. ZEUS-2D, written at NCSA, is a 2-D radiation MHD code.[2,3,4] EOSOPA[5] is an atomic physics computer code for calculation of equations-of-state and opacities for BUCKY and ZEUS-2D.

BUCKY[1] is a 1-D Lagrangian radiation-hydrodynamics computer code in slab, spherical, and cylindrical geometry. BUCKY uses table lookups for detailed equations-of-state and opacities from EOSOPA[5] or SESAME.[6] Radiation transport is calculated several possible ways, including multigroup diffusion and CRE line transport. Thermonuclear burn, neutron and fusion product transport, laser, thermal radiation, and ion source deposition are modeled. BUCKY calculates the response of a solid surface to x-rays and ions including vaporization and melting.

ZEUS-2D is a two-dimensional, Eulerian-mesh radiation-magnetohydrodynamics code.[2] The fundamental hydrodynamic equations can be solved separately or augmented with magnetohydrodynamics, radiation, or both. In its published condition, ZEUS-2D had single group radiation transport, ideal gas equations-of-state and minimal energy source physics. ZEUS-2D is being modified to include the physics capabilities of BUCKY.

BUCKY has been used in the simulation of high and moderate energy density plasma phenomena. BUCKY has been used to model ICF target implosions and explosions. It has been useful in the study of ion beam driven physics experiments on PBFA-II at Sandia National Laboratories[7] and on KALIF at Forschungszentrum Karlsruhe.[8] Laser driven physics experiments on Nova at Lawrence Livermore National Laboratory have also been studied with BUCKY. Moderate energy density applications of BUCKY include fireballs in gases, and vaporization and melting of solids by x rays and ions. These applications are often related to an ICF target chamber, such as in power plant concepts and in the National Ignition Facility.[9]

Recently, there has been significant development of the BUCKY 1-D radiation-hydrodynamics code. The ZEUS 2-D radiation-magnetohydrodynamics

code is still in development and has not yet been used for problems of interest to ICF. BUCKY results have been compared with experiments at high and moderate energy densities, that are relevant to ICF targets and target chambers. These are discussed in this paper.

II. BUCKY 1-D CODE

A. Radiation Transport and Hydrodynamics

The BUCKY code has been compared with radiation burnthrough experiments performed on the Nova laser at LLNL.[10] In these experiments, x rays produced in a gold Hohlraum with the Nova laser beams are allowed to burn through a thin gold foil. The Hohlraums are cylinders 0.16 cm in diameter and 0.275 cm long with walls 25 μm thick. Gold foils and observation holes are placed in the Hohlraum walls near the center. Ten laser beams enter the Hohlraums through holes at each end of the cylinder and shine on the inside of the walls. The laser pulse shape is assumed to be trapezoidal, with a 0.8 ns flat top. The x rays create a Marshak wave in the gold, whose speed is a function of the opacity and equation of state of the gold. The transit time of the Marshak wave is measured for foil thicknesses from 1 to 3 μm by observing the history of the x-ray emissions from the back of the foils with a Streaked X-ray Imager (SXI). Simultaneously, the drive radiation inside the Hohlraum is measured with the DANTE x-ray diode array. DANTE observes the x-ray power emitted by a given area on the inside of the Hohlraum wall in several energy channels. This can be converted into an effective wall temperature that is reported as a function of time.[10]

These experiments have been modeled with the BUCKY code in 1-D. The Nova Hohlraum is modeled as two slabs of solid gold separated by 0.15 cm of low density gold vapor. BUCKY models the deposition of the laser in the vapor and on the inside edge of one of the walls, assuming that the beams are incident at 45°. By simulating the laser deposition, the radiation burning into the gold is in a spectrum calculated by the code and is not assumed to be Planckian. Radiation transport is modeled with 100 energy group flux-limited diffusion. Equations-of-state come from SESAME tables, and opacities from tables generated with the EOSOPA code, where the Unresolved Transitions Array method is used to calculate high atomic number opacities.

The proper intensity of the laser is uncertain, because in a Hohlraum the lasers are focused in distinct spots which is a 3-D problem. The intensity has been varied until the code predicts the wall temperature measured by DANTE. The wall temperature is calculated as the blackbody temperature that would create the emitted flux predicted by the BUCKY simulations. The simulations used flux limited diffusion for the radiation transport, which only provides the net flux across the wall surface, so the emitted flux is calculated as the difference between the net flux and the flux from the center of the Hohlraum, σT_r^4 (center). The radiation temperature in the center of the Hohlraum or drive temperature, the calculated wall temperature, and the DANTE measured wall temperature are plotted in Fig. 1 for a laser intensity of 150 TW/cm^2. One can see that this intensity is close to agreeing with the DANTE measurements. The effect of losses on the holes is accounted for through the adjustment of the laser power. A 1-D model like this is only useful when it is tied to a measurement of the wall temperature. The advantage of modeling the laser, as it has been in these calculations, over modeling the drive radiation as a blackbody spectrum is the inclusion of non-Planckian features. Because the calculated wall temperatures are forced to agree with the measure values, the drive fluxes on the sample foil are correct, and the spectrum is closer to correct than a Planckian would be.

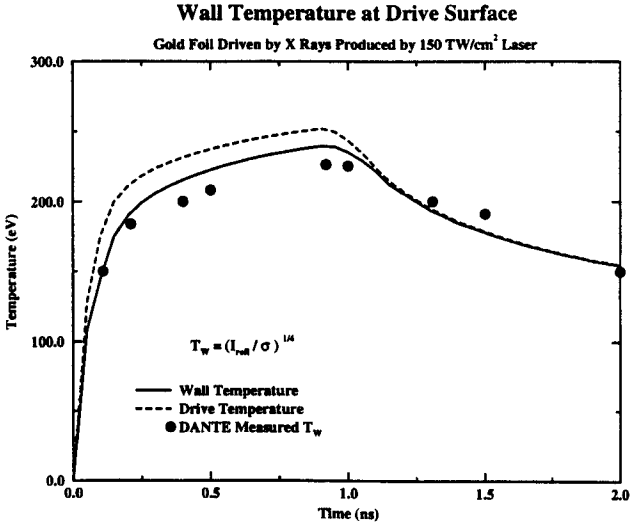

Fig. 1. Wall and drive temperatures in Nova Hohlraums. Drive and wall temperatures calculated by BUCKY for 150 TW/cm^2 laser. Wall temperatures are measured with DANTE.

Using 150 TW/cm^2 as a laser intensity, the burnthrough of various thicknesses of the gold foils has been simulated with BUCKY. The burnthrough time is defined as the time between when the drive flux reaches 10% of its maximum and when the flux at the back of the foil reaches 50% of its peak. The SXI measures the flux in channels between 210 and 240 eV and 430 and 570 eV. BUCKY group structure allows channels between 208 and 236 eV and 451 and 547 eV. The comparisons of the burnthrough times for radiation in these channels are shown in Fig. 2, plotted against foil thickness. One can see that the BUCKY simulations show excellent agreement with the experimental results. This is a confirmation of the radiation diffusion method in BUCKY and the opacities calculated by EOSOPA for use in the simulation of radiation transport in dense high atomic number plasmas.

B. Ion Stopping, Vaporization and Melting

The calculation of the deposition of ions in solids by the BUCKY code has been improved. The code divides material into two parts: hydrodynamic regions where the material is allowed to move and solid or liquid regions, where hydrodynamic motion does not occur. Heat transfer is calculated in both parts, though radiation transport is not calculated in solids. Photons reaching the interface between vapor and solid are deposited in the first solid zone. The ion deposition is calculated in the solid material as a function of distance using the Bethe model at high particle velocity and the Lindhard model at low velocities, with a transition region that smoothly transfers between the two models. BUCKY uses a model which is an improvement over Mehlhorn's[11] model by improving the smoothness of the transition region. Also, BUCKY calculates the charge state of the ions during their transit. The ion stopping in BUCKY has been compared favorably with experiments in hot stopping media.

The ion stopping in BUCKY has been compared with the TRIM code[12] for cold stopping media, relevant in target chamber walls. The TRIM code uses fits to measured cold stopping results to obtain range as a function of energy, while BUCKY is an ab initio calculation. TRIM does a 3-D Monte Carlo calculation of ion trajectories, including direction change scattering, while BUCKY assumes 1-D normal incidence ion trajectories and does a deterministic calculation. Therefore, TRIM can include the straggling effect while BUCKY cannot.

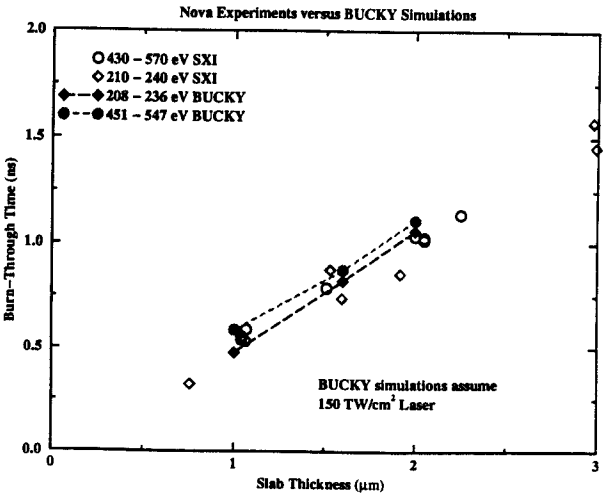

Fig. 2. X-Ray burnthrough times in gold versus thickness. Radiation flux is measured with the SXI and calculated with BUCKY at the back of a gold foil in two photon energy bands.

Vaporization is calculated in BUCKY by determining the rate that atoms leave the surface, as a function of surface temperature and lattice separation energy. This is offset by the rate that vapor atoms near the surface are condensed, as determined by the properties of the vapor when enough mass has been converted to vapor, additional vapor Lagrangian zones are created. The ability of BUCKY to model the vaporization of materials by ions has been tested by comparing a simulation with an experiment performed at Sandia National Laboratories. Tim Renk of SNL has irradiated a pure aluminum sample with 4 J/cm^2 of mixed carbon ions and protons and has measured the melt depth. The experiment was performed with a light ion diode focusing a beam onto a sample across a distance of 25 cm. This produces a beam of mixed protons and carbon ions, each with a maximum energy of 500 keV. The carbon ions carry most of the energy (3.40 J/cm^2). The carbon ions arrive after the protons because they are moving more slowly. The experiment yields a 5 μm thick melt layer.

The results of a BUCKY simulation of this experiment show that the peak surface temperature is about 2800 K and is reached at 160 ns after the start of the protons reaching the sample. The temperature profile at 60 ns is due to the protons, which have a range of a few μm in aluminum. The profile has a temperature peak of 770 K about 2.1 μm into the material. The melting temperature of aluminum is 933 K, so the

protons do no melting. The profile at 100 ns is dominated by carbon ions. The peak in temperature is at the surface because the range of carbon is so much shorter. The melt depth is estimated by just considering all material above the melting temperature to be melted. This ignores the effect of latent heat in melting. Latent heat is included in vaporization. The results are summarized in Fig. 3, where the temperature profiles in the material are plotted against position at various times. The melt depth at 100 ns is about 3 μm. The maximum temperature is reached at 160 ns and the melt depth at this time is about 5 μm. At 400 ns, the maximum melt depth of about 7 μm is released. The density of beam ions in the aluminum builds throughout the shot due to deposition. The carbons are much closer to the surface. This is compared with the TRIM code densities where 500 keV protons and carbons (monoenergetic) are deposited in aluminum. TRIM calculations include the effects of straggling, which are seen to be important for 500 keV carbon. The maximum ranges predicted by BUCKY and TRIM are quite close.

The BUCKY calculations agree reasonably well with the TRIM calculations and with the SNL experiments. BUCKY predicts 0.05 μm of vaporization. This has not been detected in the SNL experiments.

C. X-ray Vaporization

X-ray vaporization is predicted by the BUCKY code. The time-dependent deposition of a multigroup spectrum of x rays is calculated in the solid and vapor materials, using cross sections from fits to experimental values.[13] Heat transfer in the materials is simultaneously performed. Vaporization is modeled by converting zones of solid into zones of vapor. The zones of vapor are Lagrangian and exhibit hydrodynamic motion; the solid zones do not move. A zone makes this conversion either when the zones have sufficient internal energy to overcome the sensible heat and latent heat of vaporization, or when the surface vapor pressure has been high enough for a long enough time that the zone has evaporated. This model assumes that mass is lost as individual atoms or molecules, not as large chunks.

The x-ray vaporization in BUCKY has been compared with experiments done on the Helen laser. In these experiments, a laser strikes a foil, creating x rays with approximately a 160 eV blackbody spectrum. At this photon energy, most of the x-ray attenuation of Al_2O_3 is due to the Al,[13] so BUCKY uses the x-ray stopping power of Al at 3.9 g/cm^3. The x rays are assumed to be emitted in a Gaussian pulse 1 ns wide.

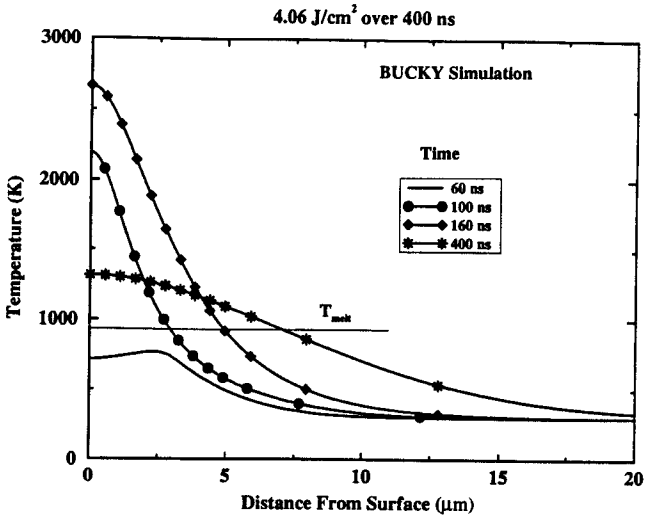

Fig. 3. Temperature profiles in aluminum plotted against depth at various times. SNL experimental conditions are assumed.

The fluence on a sample material is adjusted by varying the position of the sample relative to the x ray producing foil. The material loss is then measured. For Al_2O_3, BUCKY calculations were performed and compared with the Helen experimental results. The actual uncertainty in the results is not known, but near the vaporization threshold the uncertainty must be at least 0.05 μm. The Helen data points at about 0.6 and 0.8 J/cm^2 are shown to have zero depth removed, but to have some surface damage. This may mean a small depth removed that could not be measured. The Helen results show a threshold for vaporization of between 0.25 and 0.6 J/cm^2. The BUCKY simulations predict a vaporization threshold of 0.25 J/cm^2. At about 1.1 J/cm^2, Helen had a removal of 0.1 μm and BUCKY predicted 0.12 μm. So the agreement between BUCKY and Helen experiments was within experimental uncertainty.

III. ZEUS 2-D CODE

The ZEUS-2D radiation-magnetohydrodynamics code[2,3,4] is being augmented to add the key capabilities of the University of Wisconsin's 1-D BUCKY code, including multiple materials, multigroup radiation diffusion, and table lookup of detailed opacities and equations of state. ZEUS-2D is a two-dimensional, Eulerian-mesh code, written in covariant orthogonal coordinates and solved by finite differences with operator splitting into implicit source and

explicit transport steps. The finite-difference mesh can be modified dynamically, although ZEUS-2D is not an adaptive-mesh code, and the mesh spacing can be varied independently in both dimensions.

The unmodified ZEUS-2D code has been tested on simple radiation diffusion, microexplosion, and Hohlraum test problems, and it appears to be a suitable code upon which to base the desired modifications. Multiple materials have been implemented by including the solution of a separate equation of continuity for each species. The modifications to the difference equations required to add multigroup frequency dependence have been developed and tested in a small auxiliary code, using the same variable names and covariant differencing scheme presently in ZEUS-2D. These modifications are in the process of being introduced into ZEUS-2D. The table lookup subroutines from the BUCKY code for equations of state and opacities have been merged with the ZEUS-2D code, and debugging of this merger is in its final stages.

IV. CONCLUSIONS

Verification of ion stopping, radiation transport, atomic physics, vaporization, and melting are in progress for the BUCKY code. The physics models in BUCKY agree with experiments in several regimes. The ZEUS-2D code is being modified to include multigroup radiation diffusion, multiple material tracking and realistic equations-of-state and opacities. Models developed in BUCKY will be inserted into ZEUS-2D, allowing the accurate simulation of 2-D target and target chamber phenomena.

ACKNOWLEDGEMENT

This work is supported by the U.S. Department of Energy and Lawrence Livermore National Laboratory. We wish to acknowledge the ion vaporization experimental data provided by T. Renk of Sandia National Laboratory.

REFERENCES

1. J. J. MacFarlane, G. A. Moses, and R. R. Peterson, "BUCKY-1 – A 1-D Radiation Hydrodynamics Code for Simulating Inertial Confinement Fusion High Energy Density Plasmas," University of Wisconsin Fusion Technology Institute Report UWFDM-984 (August 1995).
2. J. M. Stone and M. L. Norman, "ZEUS-2D: A Radiation Magnetohydrodynamics Code for Astrophysical Flows in Two Space Dimensions. I. The Hydrodynamic Algorithms and Tests," *Astrophysical J. Suppl.* **80**, 753 (1992).
3. J. M. Stone and M. L. Norman, "ZEUS-2D: A Radiation Magnetohydrodynamics Code for Astrophysical Flows in Two Space Dimensions. II. The Magnetohydrodynamic Algorithms and Tests," *Astrophysical J. Suppl.* **80**, 791 (1992).
4. J. M. Stone, D. Mihalas, and M. L. Norman, "ZEUS-2D: A Radiation Magnetohydrodynamics Code for Astrophysical Flows in Two Space Dimensions. III. The Radiation Hydrodynamic Algorithms and Tests," *Astrophysical J. Suppl.* **80**, 753 (1992).
5. P. Wang, "EOSOPA - A Code for Computing the Equations-of-State and Opacities of High Temperature Plasmas with Detailed Atomic Models," University of Wisconsin Fusion Technology Institute Report UWFDM-933 (December 1993).
6. "SESAME: The Los Alamos National Laboratory Equation of State Database," LANL Report LA-UR-92-3407, edited by S. P. Lyon and J. D. Johnson (1992).
7. J. J. MacFarlane, et al., "Plasma Diagnostics Using Kα Satellite Emission Spectroscopy in Light Ion Beam Fusion Experiments," *Lasers and Particle Beams* **13**, 231 (1995).
8. J. J. MacFarlane and P. Wang, "Numerical Simulation of High Energy Density Plasmas in KALIF Beam Target Interaction Experiments," Fusion Power Associates Report FPA-95-3 (1995).
9. R. R. Peterson, J. J. MacFarlane and Ping Wang, "X-ray and Debris Emission from Direct and Indirect National Ignition Facility," these proceedings.
10. J. L. Porter, et al., "The Albedo of Gold at High Temperatures," ICF Quarterly Report, Lawrence Livermore National Laboratory Report UCRL-LR-105821-94-4 (1994).
11. T. A. Mehlhorn, "A Finite Material Temperature Model for Ion Energy Deposition in Ion-Driven ICF Targets," *J. Appl. Phys.* **52**, 6522 (1981).
12. J. F. Ziegler, "TRIM-90 The Transport of Ions in Matter," IBM - Research, Yorktown, New York (1990). Also, J. F. Ziegler, J. P Biersack, and U. Littmark, "The Stopping and Range of Ions in Solids," Pergamon Press, New York (1985).
13. F. Biggs and R. Lighthill, "Analytical Approximations for X-Ray Cross Sections III," Sandia National Laboratories Report SAND-0070 (August 1988).

U.S. Department of Energy

Contract No. DE-AS08-88DP10754

The Development and Application of
Advanced Analytical Methods
to Commercial ICF Reactor Chambers

Task 3
Final Report

ALARA: Analytic and Laplacian Adaptive Radioactivity Analysis
A Complete Package for Analysis of Induced Activation

Fusion Technology Institute
University of Wisconsin-Madison

Abstract

While many codes have been written to compute the induced activation and changes in composition caused by neutron irradiation, most of those which are still being updated are only slowly adding functionality and not improving the accuracy, speed and usability of their existing methods. ALARA moves forward in all four of these areas, with primary importance being placed on the accuracy and speed of solution.

By carefully analyzing the various ways to model the physical system, methods to solve the mathematical problem and the interaction between these two issues, ALARA chooses an optimum combination to achieve high accuracy, fast computation, and enhanced versatility and ease of use.

The physical system is modelled using advanced linear chains, which include the contributions from straightened loops in the reaction scheme, while the truncation philosophy minimizes the discrepancies between the model and the real problem. The mathematical method is then adaptively chosen based on the characteristics of each linear chain to use analytically exact methods when possible and an accurate expansion technique otherwise.

Future modifications to ALARA include addition of new functionality by implementing methods to use new data libraries, implementing methods to get new information from existing libraries, enhancing usability, and improving speed by fine tuning and parallel processing.

Chapter 1

Introduction

When designing any system with a large neutron flux, an important characteristic is the amount of induced activation expected in the system's components during operation, at the end of life and at various times after the shutdown of the system. Many codes have been written to perform such calculations for a variety of systems, from accelerators to fission and fusion reactors. The special conditions of fusion reactors, such as high neutron flux/fluence and pulsed operation, have led to many variations of these codes.

The calculation of induced radioactivity in the first wall, blanket and shield materials is an important task for the design and safety of fusion reactors. The neutron products of the D-T reaction induce radioactivity by interacting with and transporting through these materials with much higher initial energies and populations than those of fission reactors of similar power. The results of these radioactivity calculations are used extensively in safety and design analyses to determine such parameters as the nature of the radioactive waste, the amount of shielding required for radiologically sensitive components, and the decay heating after shutdown. Like other engineering calculations, the accuracy of the results is important; overly conservative approximations result in costly and complicated designs while liberal approximations result in safety and technical hazards to the operators, scientists, public and equipment.

To solve this problem a code must perform two steps. First it must model the physical system in time, space and isotopic composition, creating a system of linear first order ordinary differential equations [ODE's]. Second, the solution to this system of ODE's must be found using a numerical technique. Both steps are non-trivial since the physical problem, while finite in time and space, is theoretically infinite in final isotopic composition, and the resulting ODE's have characteristics which can make their efficient and accurate solution difficult.

ALARA is a new computational tool for performing such calculations. Given a groupwise neutron flux, ALARA uses data from a variety of libraries to determine the altered material composition which is then used to calculate the activity, $\beta-$, $\gamma-$, and $\alpha-$ heating. In addition, a groupwise γ-ray source flux can be computed by ALARA to be used for the calculation of doses. Finally, if provided with an adjoint importance field based on flux-to-dose conversion factors and the gamma source distributions, ALARA can directly calculate the biological dose.

1.1 Historical Attempts and Failings

The computational solutions to this problem have been well studied. Many different approaches for modelling the physical problem have been combined with at least as many mathematical solution methodologies. Each combination has its advantages and disadvantages,[1] but none have arrived at an optimum mixture of accuracy, efficiency and usability. Even ignoring the issue of usability, there are few codes which are keeping up with the demands of greater accuracy in modelling and solutions without becoming inconveniently slow.

One of the best performers in the past, in terms of speed and accuracy, has been the DKR[2–4] family of codes.[a] Unfortunately, even though it reaches the ultimate in mathematical accuracy and efficient operation, its physical modelling has left it subject to much philosophical criticism. Namely, DKR is unable to model loops in the reaction scheme. If an isotope undergoes a series of transmutations and decays which lead back to itself, DKR ignores any such contribution in all but the simplest of cases. While it has been shown that this is a somewhat valid criticism,[5] those codes which have addressed this problem in the past have many other failings. Another criticism of DKR is its inability to track and log the production of light ions, often important when analyzing the mechanical integrity of a material. On the other hand, DKR has pioneered the ability to exactly model pulsed irradiation histories and use mathematically exact solution methods while solving a multi-dimensional input problem.

Two of the most popular alternatives to DKR are FISPACT[6] and RACC.[7,8] While FISPACT is heavily used in Europe, it has a number of disadvantages. First and foremost, it is unable to accurately and exactly model the pulses which are today part of the designs of so many fusion reactor systems. This has been shown to be an important issue in the calculation of activity for some isotopes, leading to errors of up to several orders of magnitude.[9] Furthermore, it uses an ODE solver which is step-wise in time and, given the stiffness of the system, requires a slow and tedious calculation. Finally, as a 0-dimensional code, it is only able to find a solution for one given spectral distribution with each operation. While RACC has historically had the same problems with pulse modelling and mathematical method, the newest version, RACC-P, has addressed these issues and now models the pulsing exactly and uses a matrix solution method to increase the speed. It does, however, have its own drawbacks. In certain regimes, the solution method for each matrix is subject to significant errors which can then be amplified as this matrix is used to repeatedly calculate the final answer. The data handling methods of RACC are its biggest obstacle to efficient and accurate operation. First, it employs a philosophy to truncate the reaction schemes which leads to inconsistent precision in the solution. It also recreates the reaction schemes for each point in space with a different flux spectrum, a very time consuming process which must be accelerated by solving the problem with a flux which is averaged over a number of spatial points.

While ALARA is an entirely new code product, the methods and philosophies embodied in DKR were chosen as a starting point for its development. The basic philosophies of exact modelling of pulsing, consistent truncation of reaction schemes, and mathematically exact solution methods were retained and the main criticisms addressed. The design philo-

[a] The DKR family of codes has evolved much since the original authoring of DKR to the most recent version known as DKR-Pulsar. Throughout this report, DKR will refer generally to the entire family and specifically to the most recent version.

sophy is outlined later in this chapter. The specific methodologies and techniques used to improve the physical modelling and mathematical solution are described in Chapters 2 and 3, respectively.

1.2 Design Philosophy

ALARA has been designed with three basic principles in mind: accuracy, speed, and simplicity. These three qualities have been maximized in ALARA after extensive research of the models involved in such calculations.[1,5] The errors, time of execution, and learning curve have all been made "as low as reasonably achievable".[b] The methods used to model the physical system and to perform the mathematical solution are carefully combined to preserve or enhance the accuracy while accelerating the solution. Throughout all this, there is an underlying effort to ensure that ALARA will be easy to use by providing a simple, well-documented input file format, checking this input for errors, and providing a broad, flexible range of options.

1.2.1 Accuracy

The accuracy of the final solution is affected both by how realistically the physical system is modelled and by what mathematical methods are employed for the final solution. Unfortunately, these two requirements often conflict; as the physical model becomes more realistic the required mathematical methods become more approximate or error prone. When modelling the physical problem, two of the most important issues are how to deal with loops in the reaction scheme and how to truncate the infinite isotopic composition to a finite problem. While the effect of the latter on the mathematical method is negligible, the former has a great impact. In the past, the unwritten rule has been that realistic treatment of loops requires complicated/inefficient mathematical methods. ALARA has broken that rule by finding a physical approximation to the loops which retains problem accuracy and allows for quite simple and efficient mathematical methods. The keys to ALARA's mathematical accuracy are the ability to adaptively choose the mathematical technique and the accuracy of those techniques. Two of the three mathematical techniques which ALARA employs are mathematically exact!

1.2.2 Speed

The most significant factor affecting the speed is the chosen class of mathematical method. In particular, unless a linear transformation matrix method is used the time required to exactly model a pulsed history will be large. ALARA employs such matrix methods, solving for the linear transformation from the initial isotopic composition to the final composition for each pulse and inter-pulse dwell period, and then multiplying these matrices to obtain a complete linear transformation for the entire history. In addition to this decision, speed was considered throughout the code design process. For example, data library formats and internal data handling have been implemented with modern techniques to enhance versatility without sacrificing speed.

[b] This phrase is the origin of the term ALARA, a well known philosophy in the nuclear industry related to the minimization of radiation exposure when working in radioactive environments.

1.2.3 Simplicity

While accuracy and speed have long been issues in the creation of engineering codes, their simplicity is of increasing importance. In this context, simplicity is an issue for both modification/maintenance and use of the code. Since ALARA has been written in C++, it benefits from some of the philosophies of object-oriented code design. This allows the code itself to be more readable to future programmers and also facilitates enhanced modularity. This modularity means that if new functionality is added to the code, it can be optimized internally with minimal detrimental effect on the existing code.

ALARA has also been designed with the user in mind. Even though improved methods have existed for years, many codes have continued to use input formats which are reminiscent of punch card input entry. Furthermore, most tools in this field have been designed for the solution at a single spatial point, requiring many subsequent and slightly altered runs to get any kind of spatial information. ALARA allows the user to find the solution to an activation problem in a variety of different multi-dimensional geometries, using a flexible system to define the material properties and allowing a complicated pulsed/intermittent irradiation history and a variety of after-shutdown solution times. Furthermore, the input file can be fully commented, preventing the common difficulty of creating a long list of seemingly disconnected numbers for code input.

Finally, the data used by ALARA can come from one of a variety of sources. To accommodate this, a companion code, ALARA Data Conversion [ALARA_DC], has been written and is described in Appendix C.

Chapter 2

Physical Model

After describing the nature of the physical problem, this chapter will describe the philosophies, approximations and methods used by ALARA to model this physical problem.

When an isotope is subjected to neutron irradiation, it is likely that a neutron will interact with a nucleus of that isotope, converting it to a different isotope. Many such reactions are possible with each isotope, so that after only one round of neutron reactions, a material made of only one isotope can be partially converted into over 20 others. These isotopes, in turn, can undergo similar interactions, leading to yet more isotopes, and so on. Many of these isotopes can and will be radioactive, and through their decay, even more possible isotopes can enter the physical system. If this is represented graphically (Figure 2.1), it forms a tree of isotopes which can go on, in principle, infinitely. For the purpose of discussing this physical problem, the products of each generation of reactions (transmutation or decay) will be referred to as a *rank* and each individual reaction from one isotope to another will be referred to as a *branch.*

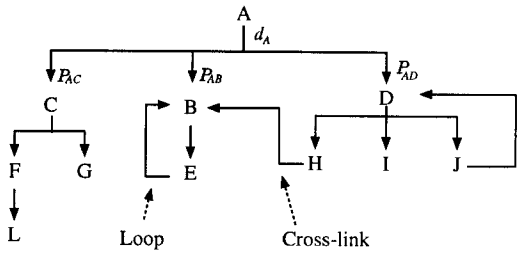

Figure 2.1: Sample reaction tree showing loops and cross-links.

Each isotope has a unique destruction rate, d_i, while each branch of this tree has an associated production rate, P_{ij}, for the isotope to which this branch leads. For decay reactions, this production rate is independent of the neutron flux while for transmutation reactions it is a function of the spectral distribution of the flux. The raw data used to form these production rates is read from large data libraries, either as decay rate/half-life data from decay libraries or as transmutation cross-sections from transmutation libraries. The methods used to measure, evaluate and compile such data will not be discussed here.

It is possible, as mentioned in Chapter 1, for one nucleus to undergo a series of reactions, being converted from one isotope to another and so on and eventually back to the original isotope. Loops such as this are of specific importance when modelling this physical problem. The nature of such loops is somewhat random; they can begin at any rank in the tree and can undergo any number of reactions before closing the loop. If the *order* of a loop is defined as the number of isotopes between two occurences of the same isotope in a loop, then the order can range from 1 to greater than 10. A related but less important phenomenon is that of

"cross-linking" of subtrees. This is caused when two different isotopes, which could each be at any rank, both undergo reactions to the same isotope. In this case, the tree can become quite tangled, departing from the classical tree structure known and studied in computer science.

While the problem has finite dependencies on time and space (see below), it is the modelling of this potentially infinite aspect of the physical problem which causes the most difficulty and is described in Section 2.1.

Current designs for experimental and power fusion reactors of all types often include the necessity for pulses, from the short frequent pulses of an inertial confinement system to the long infrequent pulses of a magnetic confinement system. This pulsing creates an important effect[9–11] since between each pulse, the radioactive isotopes which have been created are able to decay while the stable isotopes remain unchanged. This changes the distribution of isotopes having important implications on the reactions during the subsequent pulses. In practice, these reactors can be pulsed at different frequencies, depending on the experimental, power and/or maintenance requirements. Section 2.2 will describe the approximations and assumptions used in modelling this aspect of the physical model.

Finally, the material composition and neutron flux spectrum will vary from location to location in the device. A structural region of a problem may contain some variety of steel while a coolant region might have water and a breeding region would contain lithium. The initial isotopes, and thus the reaction trees, will therefore be very different for each region. Further, for each point of interest, the spectral distribution and magnitude of the fluxes will be different. Thus, even for identical trees from the same material composition, the production rates for each isotope will vary from point to point. Section 2.3 describes the important aspects of modelling these spatial variations.

2.1 Chain Creation

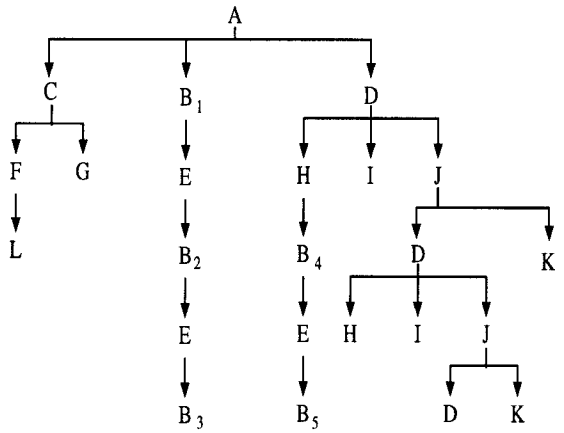

Figure 2.2: Fully straightened and unlinked reaction tree.

In principle, it is possible to convert the physical model in its entirety to a mathematical one and solve the problem directly. It is much more practical, however, to convert the single large problem into a number of smaller subproblems and then solve each one individually, combining the results where appropriate. The first step in this process is to develop a philosophy to convert the cross-linked and loop-filled tree into a true classical tree structure (see Figure 2.2). To perform this requires the introduction of what will be called *partial-contribution* isotopes, or *pc*-isotopes. A *pc*-isotope is an isotope in a tree or chain which is not necessarily unique. The basic physical model described above only allows for one occurence of each isotope in each tree. By creating *pc*-isotopes, a somewhat larger system is created, but its solution is more simply achieved. After the full solution of the problem, the *pc*-isotopes

are collapsed into unique isotopes, with the contribution from each being accounted for appropriately. While the use of *pc*-isotopes to remove cross-links is straightforward, their implementation for removing loops is more complicated and the subject of section 2.1.1.

After all the loops and cross-links have been removed, each tree is traversed in a *depth-first search*[a], creating a number of independent linear chains (see Figure 2.3). In practice, it is necessary at this stage to truncate these chains to some finite size. As mentioned above, these trees, and therefore the resulting chains, are theoretically infinite and some philosophy must be developed to decide exactly how these chains will be truncated. This is the subject of section 2.1.2.

2.1.1 Loop Handling

In principle, the method used to remove the loops from the reaction trees is the same as that used to remove the cross-links. Loops, in fact, are just a special case of cross-linked chains, where the chain is linked to itself. Thus, loops are removed by a technique which will be refered to as *loop straightening*. In this method, all the isotopes which make up a loop in the tree are repeated using *pc*-isotopes. This repetition occurs an infinite number of times in theory, but in practice, the chain is truncated using the same methods which are outlined in Section 2.1.2 below.

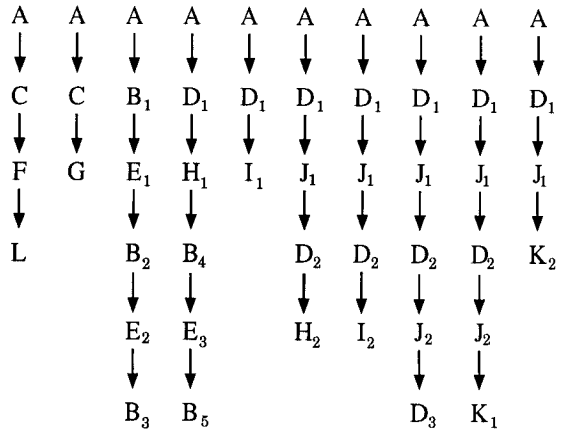

Figure 2.3: Separated linear chains representation of reaction tree.

The primary reason for choosing such a method is to preserve the characteristics of the mathematical model which will be created. If the reaction scheme is treated directly without the removal of cross-links and loops, the mathematical model will inevitably be a somewhat large and full matrix representing a stiff system of ODE's and solving for a large number of isotopes at the same time (Equation 3.1). If, however, it is possible to convert the physical model to one of linear chains, the mathematical model can take the form of a lower bidiagonal matrix (Equation 3.3). This type of mathematical model can be subjected to many special treatments for the accurate and efficient solution of the matrix exponential, some of which are described in Chapter 3.

It is now necessary, however, to show that the use of these methods does not jeopardize the physical accuracy of the model. First, the qualitative effect that the loop-straightening process has on the model must be understood. Each iteration of the loop isotopes adds a new set of *pc*-isotopes to the chain and will be referred to as a *correction*. Just as in many such approximation processes, in the limit as the number of corrections becomes very large, the result approaches the exact solution. It is therefore necessary to choose a point to truncate the approximation while retaining confidence in the solution. Of course, the entire problem, loops or not, is theoretically infinite, so this truncation issue is not unique to loops.

[a] A depth-first search is an algorithm which moves deeper into a tree as far as it can go before backtracking and moving down a different path.

Work has been done to show that the loop-straightening method is also valid quantitatively.[5] A study of the numerical effect of the loop corrections on the result showed that for many realistic first order loops, a single correction could reduce the relative error to the order of 10^{-6} and as few as 3 corrections can reduce this error to less than 10^{-10}. First order loops were used in this analysis because the contribution from each correction in such cases is logically greater than in higher order loops. It is important to recognize the importance of this measure being a *relative* error. It has no effect on the precision of the results (discussed further in Section 2.1.2), but only on the accuracy of the results.

Relative to other loop handling models, loop straightening can improve the speed and accuracy of the mathematical calculation while maintaining the same precision in the physical model as is being used throughout.

2.1.2 Truncation Philosophy

On the surface, the concept of truncating the theoretically infinite chains created by modelling the physical system for these calculations is a simple one: truncate the chain once the isotopes have a negligible effect on the result. In practice, however, this is a delicate process which deserves some discussion.

There are two primary issues to be considered, namely,

- how can the effect of the isotopes at a certain rank in the chain be calculated, and,
- how the significance of that effect can be determined.

The easiest way to calculate the effect of a particular isotope in a chain is to simply solve the problem including that isotope. This would require solving the entire problem twice, however, drastically affecting the speed of the problem. The first enhancement, therefore, is to perform this reference calculation only once for each initial isotope using a flux which is somehow representative of all the spatial points which contain that initial isotope (see Section 2.4). If every point in space has a unique set of initial isotopes, this still leads to solving the problem twice, but as the problems become more complex, with perhaps 50 or more spatial points sharing the same mixture definition, this is a significant savings.

What is the best flux to represent all the spatial points which share an initial isotope? Since higher fluxes will tend to maximize the amount of transmutation from one isotope to another, the obvious choice is some flux which is a maximum bound for the problem. Since the flux is groupwise and it is possible that one spatial point will have the highest fast flux while another point has the highest slow neutron flux, the best choice for a bounding flux should be the groupwise maximum flux of all the points which share an initial isotope. This reference flux can then be used to solve the problem for a particular chain as it is being created.

If this truncation reference calculation assumes that a unit quantity of the initial isotope exists, then the solution gives the relative production of each isotope in the chain. A user specified tolerance can then be used to determine how significant the relative production of the last isotope in that chain is, and decide whether to continue the creation of the chain. This too, however, is more subtle than first appearances suggest.

Consideration must be given as to how the user specified tolerance is to be interpreted. The best interpretation of the many possibilities is that of an *atom loss tolerance*. Due to the fact that we are truncating a theoretically infinite chain, atoms will be lost from the physical model through branches leaving the last isotope in the chain. It is best, therefore, to use this truncation tolerance to minimize this atom loss. Since it is also possible for this last isotope to have a low relative production rate, yet still have a high loss of atoms through its branches, it must be possible to calculate not just the relative production of the last isotope in a chain, but the atom loss through this last isotope. Fortunately, this is quite simple. By temporarily zeroing the destruction rates of this last isotope, the result of the reference calculation will be the total relative production of all isotopes in the subtree rooted by this isotope, and therefore represents the maximum possible atom loss through this isotope. This value can then be compared to the user specified tolerance, which is now interpreted as the maximum atom loss in any chain.

There are obviously two mechanisms of atom loss: transmutation and decay. The former is only possible when there is a neutron flux present but the latter occurs throughout the operation lifetime as well as after the shutdown of the device. This difference is important since the after-shutdown lifetimes are often much longer than the operation lifetimes and it is during these times that the activity is often most important. To guard against these differences, it is necessary to compare the relative production both at shutdown and at each after-shutdown time. If the relative atom loss is less than the tolerance at shutdown, but greater than the tolerance at any of the after shutdown times, it may represent an important atom loss path during shutdown. It is here that we can distinguish between atom loss mechanisms. Since the only atom loss mechanism after shutdown is decay, only subsequent decay branches are important, even if the relative atom loss is greater than the tolerance.

The results of this philosophy are quite simple. First, any relative atom loss which exceeds the tolerance at shutdown will result in a continuation of the chain. Second, if the relative atom loss is less than the tolerance both at shutdown and at all after-shutdown times, then the chain should be totally truncated at this point. Finally, if the relative atom loss is less than the tolerance at shutdown and greater at some after-shutdown time, then all transmutation branches in that subtree should be truncated but decay branches followed.

This truncation approach affords some rudimentary error estimates for the results. Using an analogy to experiment, the user specified tolerance provides a measure for the *precision* of the calculation. The smallest possible correction and hence the largest possible error for the results for any one isotope is this truncation tolerance. This will also be the dominant source of physical modelling error in the result. Since these same truncation rules are used indiscriminately for truncating straightened loops, the error from truncation will always be greater than the error caused by not using more corrections to the loop. Thus, following the analogy to experiment, the *accuracy* of loop solutions is affected by the number of corrections while the precision is affected by truncation tolerance. Since the number of corrections is determined indirectly by the truncation tolerance, this methodology provides the most consistency across the entire problem.

2.1.3 Alternatives and Extensions to the Truncation Philosophy

The full implementation of this philosophy does have detrimental effects on the speed of the solution. The most significant drag is caused by the full pulsing solution of the chain for each truncation calculation. An alternative is to combine the reference flux concept with that of a reference time, a representative steady-state simulation time to use only for truncation calculations returning to the exact pulsing solution when performing the final solution. When using this alternate method, it is important to understand the full implications. In particlar, even if the chosen reference time approximates the operation history well, the reference calculation includes no after-shutdown history, a period in which many isotopic compositions may change. The user should always consider how sensitive the solution is to this reference time.

Another source of drag is the solution of completely negligible data at the truncation point. Considering the precision and extent of the available data, it is possible to reach a point in the chain where the relative atom loss is many orders of magnitude less than the truncation tolerance. While it is obvious that the chain should be truncated, the full solution of this *pc*-isotope will probably lead to a negligible contribution. A second user defined tolerance, known as an ignorance tolerance, can be used to determine when a truncation point should be ignored completely and the chain creation procedure should continue without performing the complete solution of this *pc*-isotope. To ignore all truncation points, an ignorance tolerance of 1 should be used and to ignore none, an ignorance tolerance of 0.

This truncation method provides the optimum combination of speed and accuracy. In general, using a relative atom loss is the most accurate way to physically model the system and allow the user to get a useful measure for how precise the results are.[1] Faster approximations could be made to conservatively estimate the relative lost atom production. However, while conservatisms may seem appropriate for the physical model, they can lead to the physical model being too large, causing the time required for mathematical solution to be greater. It should also be noted that this measure of the truncation error in the physical model is an upper bound since a groupwise maximum flux is being used for the calculations. In many spatial regions, the actual production in the final solution may be many of orders of magnitude less.

2.2 Pulsing Representation

Modern fusion reactor designs for both power and experimental reactors include either the ability or necessity for pulsed or intermittent operation. This has important effects on the calculation of induced activity since the radioactive isotopes which may be produced during the pulses can decay between them. When an accurate pulsed solution is calculated and compared to steady-state approximations,[9] the errors can be significant.

For most systems the pulsing scheme will follow a somewhat regular work schedule. As an example, consider an experimental reactor which is designed to operate for 10 minutes every half hour during the work day. If each operation period is neutronically identical, this could easily be modelled for a 20 year lifetime as in Table 2.1. This kind of pulsing history can be modelled exactly by ALARA, solving the problem efficiently through the use of matrix methods.

Description	Time	# of Pulses
Pulse length	10 min	
Operation dwell	20 min	16 (half-hour segments)
Nightly dwell	16 h 20 min	5 (work days)
Weekend dwell	64 h 20 min	49 (weeks without maintenance)
Annual Maintenance	3 weeks 64 h 20 min	20 (years)

Table 2.1: Example pulsing schedule for experimental device.

Thus, the only assumption made by ALARA for the modelling of a pulsed history is that the pulses all be of the same height (spectral characteristics) and length. Future modifications may allow the pulse characteristics to change from one part of the scheme to another.

2.3 Spatial Variations

As mentioned above, most systems will have gross variations in material composition from one spatial point to another. The existence of any material will also mean that the flux can experience similar variations. It is most convenient for the user if this can be modelled entirely within a single run of the code, rather than requiring that the code be run many times, once for each point in space. This requires an algorithm which will not cause the solution to become slow and inefficient.

ALARA accomplishes these goals. The space can be divided in up to three dimensions and a number of different geometries into *zones* whose boundaries are the transition from one material composition to another. Each zone contains a defined isotopic composition and so a *mixture* can be thought of as the possibly disjoint set of all zones which have the same initial isotopic composition. Each zone can be further subdivided into *intervals*, each allowed to have a different flux spectrum. It is important that the data handling of these spatial variations be implemented efficiently, as described briefly in the next section.

2.4 Implementation of Physical Modelling Techniques

To implement these various methods and techniques efficiently, it is first necessary to optimally cross-reference the physical model. In particular, many different mixture definitions could, in practice, consist of overlapping sets of initial isotopes. If the solution is found by looping through these mixtures, the chain information for the same root isotopes would either have to be recalculated or stored, having a severe impact on either the speed or memory resource, respectively. The solution is to create a global list of unique isotopes which are cross-referenced to the relevant mixture definitions for the number density information, which are, in turn, cross-referenced to the appropriate intervals for the local flux information. With this list in place, the solution can be found by looping through each of the globally unique root isotopes. The reference truncation flux must be found across all the intervals containing the same root isotope, by accessing the cross-referenced lists of intervals from the cross-

referenced list of mixtures. Finally, as alluded to above, as each chain is solved and its relevant solution information stored, the chain information itself can be discarded reducing any storage requirements.

Also, because the solution for each interval contains information about a large potential number of isotopes in the final composition, an efficient data structure was needed to store this data. The solution was a linked list in which each list item contained an identifier for the isotope, the final number densities at shutdown and the various after-shutdown times, and decay information relevant for the calculation of activities and decay heats.

Chapter 3

Mathematical Technique and Theory

The mathematical problem which results from the physical problem described in Chapter 2 is, at first glance, a very simple one. If the original decay scheme (without removing cross-links and straightening loops – Figure 2.1) is converted directly to its mathematical equivalent, the result is a compact but potentially stiff system of linear first order ordinary differential equations [ODE's],

$$\begin{aligned}\dot{\vec{N}}(t) &= \boldsymbol{A}\vec{N}(t) \\ &= \begin{bmatrix} -d_1 & P_{2\to1} & P_{3\to1} & \cdots & \cdots & P_{l\to1} \\ P_{1\to2} & -d_2 & P_{3\to2} & \cdots & \cdots & P_{l\to2} \\ P_{1\to3} & P_{2\to3} & -d_3 & \cdots & \cdots & P_{l\to3} \\ \vdots & \vdots & \vdots & \ddots & & \vdots \\ \vdots & \vdots & \vdots & & -d_{l-1} & P_{l\to l-1} \\ P_{1\to l} & P_{2\to l} & P_{3\to l} & \cdots & P_{l-1\to l} & -d_l \end{bmatrix} \cdot \begin{bmatrix} N_1 \\ N_2 \\ N_3 \\ \vdots \\ \vdots \\ N_l \end{bmatrix},\end{aligned} \tag{3.1}$$

where:

$$\begin{aligned}\vec{N} &\equiv \text{number densities, } N_i\text{, of all isotopes} \\ d_i &\equiv \text{destruction rate of isotope } i \\ P_{i\to j} &\equiv \text{production rate of isotope } j \text{ from isotope } i \quad .\end{aligned}$$

After loop straightening and cross-link removal has been performed, the result is a some-

what larger, simpler set of ODE's:

$$\dot{\vec{N}}(t) = \boldsymbol{B}\vec{N}(t)$$
$$= \begin{bmatrix} -d_1 & 0 & 0 & \cdots & \cdots & 0 \\ P_{1\to 2} & -d_2 & 0 & \cdots & \cdots & 0 \\ P_{1\to 3} & P_{2\to 3} & d_3 & \cdots & \cdots & 0 \\ \vdots & \vdots & \vdots & \ddots & & \vdots \\ \vdots & \vdots & \vdots & & -d_{m-1} & 0 \\ P_{1\to m} & P_{2\to m} & P_{3\to m} & \cdots & P_{m-1\to m} & -d_m \end{bmatrix} \cdot \begin{bmatrix} N_1 \\ N_2 \\ N_3 \\ \vdots \\ \vdots \\ N_m \end{bmatrix}. \tag{3.2}$$

This lower triangular matrix is quite sparse with a maximum of two entries in each row since each isotope has only one production path and one total destruction rate.

Finally, if this physical model is further broken into the previously described linear chains, many small sets of ODE's are created with special simplifying characteristics,

$$\dot{\vec{N}}(t) = \boldsymbol{C}\vec{N}(t)$$
$$= \begin{bmatrix} -d_1 & 0 & 0 & \cdots & \cdots & 0 \\ P_{1\to 2} & -d_2 & 0 & \cdots & \cdots & 0 \\ 0 & P_{2\to 3} & -d_3 & \cdots & \cdots & 0 \\ 0 & 0 & P_{3\to 4} & -d_4 & & \vdots \\ \vdots & \vdots & \vdots & & \ddots & 0 \\ 0 & 0 & 0 & \cdots & P_{k-1\to k} & -d_k \end{bmatrix} \cdot \begin{bmatrix} N_1 \\ N_2 \\ N_3 \\ \vdots \\ \vdots \\ N_k \end{bmatrix}. \tag{3.3}$$

The bidiagonal nature of these matrices is an important factor in subsequent derivations and calculations.

In all cases, the generic solution takes the form

$$\vec{N}(t) = \boldsymbol{T}\vec{N}_o(t), \tag{3.4}$$

where $\boldsymbol{T}$ is the exponential of the matrices $\boldsymbol{A}$, $\boldsymbol{B}$, or $\boldsymbol{C}$, depending on which method is used (e.g. $\boldsymbol{T} = e^{\boldsymbol{A}t}$).

It is interesting to compare the sizes of these three matrices as it gives some initial insight into the efficiency of the solution. To compare the size of the original scheme, n, with that of the straightened tree, m, is not easy. Since the physical conversion is to convert cross-links and loops into *pc*-isotopes, it is clear that $m > n$; however, the severity of this inequality is difficult to determine. An approximate comparison between k and m, however, can be made. Since $\boldsymbol{B}$ represents a true tree structure, it can be analyzed by assuming that it is a full n-ary tree, that is, assuming that each *pc*-isotope in the tree has the same number of branches. Since k is the depth of such a tree, there will be n^{k-1} chains representing the $m = \frac{n^k-1}{n-1} \approx O(n^{k-1})$ nodes of the tree. The mathematical operations performed on these matrices are generally at least of order of the square of the matrix dimension, and often the cube. Thus, for matrix $\boldsymbol{B}$, the mathematical costs will be at least $O(n^{2k-2})$ and possibly $O(n^{3k-3})$ or higher. On the other hand, for the n^{k-1} matrices $\boldsymbol{C}$, the mathematical costs will

be $O(k^2n^{k-1})$ or $O(k^3n^{k-1})$. This very rough analysis shows that for mathematical operations of order x, as long as $n^{1-\frac{1}{x}} > k^{\frac{1}{k-1}}$, the linear chain method will be more efficient. While it may be difficult to visualize this relationship, it can be used to define some limits. For second order operations, for $n \geq 4$, the linear chain method is always more efficient. For third order operations, only $n \geq 3$ is required. On the other hand, for $n = 2$, the chain depth, k, must be greater than 2, and even $k = 3$ requires 5^{th} order operations for the linear chains to be more efficient. Finally, for a real problem in which $n \geq 4$, the linear chain method is more efficient for all orders of solution.

It is important to note that not only is this analysis not rigorous, but the order of the mathematical solution is itself dependent on the method which is used. Thus, the analysis gives a first glance into the comparison of efficiency, but is hardly complete.

By transfering this system to the Laplace domain and considering each equation individually, it is possible to write the solution in a more compact form (N.B. P_i implies $P_{i-1\to i}$):

$$\tilde{N}_i = \frac{N_{i_0}}{s+d_i} + P_i\frac{\tilde{N}_{i-1}}{s+d_i} \tag{3.5}$$

$$\begin{aligned} &= \frac{N_{i_0}}{s+d_i} + \frac{N_{i-1_0}}{s+d_{i-1}}\frac{P_i}{s+d_i} + \frac{N_{i-2_0}}{s+d_{i-2}}\frac{P_{i-1}P_i}{(s+d_{i-1})(s+d_i)} + \cdots \\ &\quad + \frac{N_{2_o}}{s+d_2}\prod_{j=3}^{i}\frac{P_j}{s+d_j} + \frac{N_{1_o}}{s+d_1}\prod_{j=2}^{i}\frac{P_j}{s+d_j}, \end{aligned} \tag{3.6}$$

which can be written as

$$\begin{aligned} \tilde{N}_i &= \sum_{j=1}^{i}\tilde{N}_{ij} \\ &= \sum_{j=1}^{i}N_{j_o}\prod_{k=j+1}^{i}P_k\prod_{l=j}^{i}\frac{1}{s+d_l} \\ &= \sum_{j=1}^{i}N_{j_o}\tilde{F}_{ij}(s)\prod_{k=j+1}^{i}P_k. \end{aligned} \tag{3.7}$$

In this representation, the matrix $\boldsymbol{T}$ is filled by setting

$$\begin{aligned} T_{ij} &= N_{ij}/N_{j_o} \\ &= \mathcal{L}^{-1}\left[\tilde{F}_{ij}(s)\right]\prod_{k=j+1}^{i}P_k, \end{aligned} \tag{3.8}$$

and it becomes an exercise of solving for the inverse transform of the term

$$\tilde{F}_{ij}(s) = \prod_{l=j}^{i}\frac{1}{s+d_l}. \tag{3.9}$$

Normally, two such matrices, $\boldsymbol{T}$ and $\boldsymbol{D}$, are required to represent the pulse and dwell times, respectively. In the first case, all the destruction and production rates include the terms for neutron transmutation which are dependent on the flux spectrum and therefore it is only during this period in which loops can occur in the isotope tree. In the dwell period, the destruction and production rates are only those of decay, and therefore, many of the values will be zero.

3.1 Adaptive Mathematical Methods

Upon examining available methods to solve such lower bidiagonal systems, it can be seen that there are certain easily determined characteristics of the matrix which can be used to adaptively choose a method for each linear chain which will optimize the speed and accuracy of the solution.

The eigenvalues of these matrices are simply the diagonal elements, which in turn are the destruction rates of each isotope in the linear chain being modelled. True degeneracies in these values will occur only when the chain being modelled by this matrix has straightened loops and a simple test can determine whether this is the case. If no loop exists, this bidiagonal system is mathematically identical to the system solved by Bateman[12] many years ago, and many accurate and efficient methods exist to find the solution. This method is always used to calculate the transfer matrix for the dwell period since loops cannot exist. On the other hand, if loops do exist, the solution is somewhat more complicated and is facilitated by this transformation to the Laplace space. The next adaptive decision determines which method will be used to perform the Laplace inversion and is based on an analysis of the spectral radius of the matrix, $\boldsymbol{C}$: for sufficiently small radii, a series method can be used, while in other cases, a direct and analytic inversion is preferred.

Because the mathematical method is chosen independently and adaptively for each chain, the efficiency and accuracy of the entire solution is optimized. In particular, if a small loop occurs in one small portion of a scheme, it is not necessary to perform the slower Laplace based calculations on the entire problem when the Bateman solution is available for most of the problem. On the other hand, the solution is not limited by the non-loop Bateman solution when loops do exist.

3.2 The Analytical Bateman Solution

If all the destruction rates, d_i, are distinct, Equation 3.9 can be easily inverted,

$$f_{ij}(t) = \sum_{l=j}^{i} e^{-d_l t} \prod_{\substack{m=j \\ m \neq l}}^{i} \frac{1}{d_m - d_l}. \tag{3.10}$$

This leads to a compact representation of the solution to the Bateman equations:

$$N_i(t) = N_{i_o} e^{-d_i t} + \sum_{j=1}^{i-1} N_{j_o} \left[\sum_{k=j}^{i-1} \frac{P_{k+1}(e^{-d_k t} - e^{-d_i t})}{d_i - d_k} \prod_{\substack{l=j \\ l \neq k}}^{i-1} \frac{P_{l+1}}{d_l - d_k} \right]. \tag{3.11}$$

Finally, we can write the transfer matrix elements as:

$$T_{ii} = e^{-d_i t}$$
$$T_{\substack{ij \\ i \neq j}} = \sum_{k=j}^{i-1} \frac{P_{k+1}(e^{-d_k t} - e^{-d_i t})}{d_i - d_k} \prod_{\substack{l=j \\ l \neq k}}^{i-1} \frac{P_{l+1}}{d_l - d_k}. \tag{3.12}$$

3.3 Laplace Inversion Method

When the destruction rates (eigenvalues) are not distinct, other methods of solving Equation 3.9 are required. In general, however, because of the bidiagonal nature of the matrix representation (that is, because of the linear chain physical representation), this is a simple problem which, for a small system, can easily be solved on paper by hand. In particular, this Laplace space representation can be directly inverted to the time representation.

For repeated poles, one uses the residue theorem to determine the coefficients for each term in a partial fractions expansion. Each of those terms would result in an exponential, perhaps multiplied by a polynomial in time, t, when converted back to the time domain. Those residues are calculated using one of two simple rules.

If the pole is not repeated, then the residue, R_k, for the pole, $-d_k$, is calculated as

$$R_k = \lim_{s \to d_k} (s + d_k) \tilde{F}_{ij}(s) \tag{3.13}$$

which becomes $R_k e^{-d_k t}$ in the time domain. If all poles have a singular multiplicity, the solution reduces exactly to the Bateman solution, and can be represented in many ways. This is obviously the solution with no loops.

If the pole is repeated m times, under a partial fraction expansion, this becomes m terms in that expansion:

$$\frac{R_{km}}{(s + d_k)^m} + \frac{R_{km-1}}{(s + d_k)^{m-1}} + \cdots + \frac{R_{k1}}{(s + d_k)} \tag{3.14}$$

which becomes

$$e^{-d_k t} \left(R_{km} \frac{t^{m-1}}{(m-1)!} + R_{k,m-1} \frac{t^{m-2}}{(m-2)!} + \cdots + R_{k2} \frac{t}{1!} + R_{k1} \right) \tag{3.15}$$

in the time domain.. In this case, the residues are found using:

$$R_{kn} = \frac{1}{(m-n)!} \lim_{s \to d_k} \frac{d^{m-n}}{ds^{m-n}} \left[(s + d_k)^m \tilde{F}_{ij}(s) \right]. \tag{3.16}$$

This latter rule requires the ability to evaluate derivatives of a generic function:

$$\tilde{G}^k_{ij}(s) = (s + d_k)^m \tilde{F}_{i,j}(s) \tag{3.17}$$

at values of $s = -d_k$ for all i. By examining the successive derivatives of $\tilde{G}(s)$ it can be

shown (see Appendix A) that these derivatives can be recursively defined as:

$$\left[\tilde{G}^k_{ij}(s)\right]^{(n)} = \sum_{j=1}^{n}(-1)^j \frac{(n-1)!}{(n-j)!}\left[\tilde{G}^k_{ij}(s)\right]^{(n-j)} \sum_{i=1}^{I} \frac{1}{(s+d_i)^j} \tag{3.18}$$

and this, in turn, can be converted to a computational numerical algorithm, allowing the entire problem to be solved.

We will call this method the Laplace Inversion Method.

3.4 Laplace Expansion Method

Alternately, an expansion in $1/s$ may be desirable in some cases. There are cases in which the above method might amplify roundoff errors due to division by small numbers which result from the subtraction of two similar numbers (such as when two of the poles are very near each other), but such divisions can be eliminated by writing the solution as a difference of exponentials, expanding that difference, factoring out the offending term from the numerator and cancelling. While this seems like a monumental task to perform on an arbitrary problem, thanks to the bidiagonal nature of the system, it is again quite simple to implement. If we start again with our function:

$$\tilde{F}_{ij}(s) = \prod_{l=j}^{i} \frac{1}{s+d_l} \tag{3.19}$$

and making no assumptions about the multiplicity of the poles, we expand this as a series in $1/s$, the result is:

$$\begin{aligned}
\tilde{F}_{ij}(s) &= \frac{1}{s^{i-j+1}} \prod_{l=j}^{i} \frac{1}{1+\frac{d_l}{s}} \\
&= \frac{1}{s^{i-j+1}} \prod_{l=j}^{i} \left(1 - \frac{d_l}{s} + \frac{d_l^2}{s^2} - \frac{d_l^3}{s^3} + \cdots\right) \\
&= \frac{1}{s^{i-j+1}} \left[1 - \frac{\sum_{l=j}^{i} d_l}{s} + \frac{\sum_{l=j}^{i} d_l \sum_{k=l}^{i} d_k}{s^2} - \frac{\sum_{l=j}^{i} d_l \sum_{k=l}^{i} d_k \sum_{m=k}^{i} d_m}{s^3} + \cdots\right].
\end{aligned} \tag{3.20}$$

If $n = i - j$, in the time domain, this becomes:

$$\begin{aligned}
f_{ij}(t) = t^n \Bigg[&\frac{1}{n!} - \frac{t}{(n+1)!}\sum_{l=j}^{i} d_l + \frac{t^2}{(n+2)!}\sum_{l=j}^{i} d_l \sum_{k=l}^{i} d_k \\
&- \frac{t^3}{(n+3)!}\sum_{l=j}^{i} d_l \sum_{k=l}^{i} d_k \sum_{m=k}^{i} d_m + \cdots\Bigg]
\end{aligned} \tag{3.21}$$

and thus:

$$T_{ii} = e^{-d_i t}$$
$$T_{\substack{ij \\ i \neq j}} = f_{ij}(t) \prod_{k=j}^{i-1} P_k \,. \tag{3.22}$$

It is clear that this solution will only be computationally viable when the product, $\max\{d_i\} \cdot t$ is small. For arbitrary problems, this is only guaranteed when there are small times, but can easily be tested for a particular problem. Other representations can be formed, each providing different insight into the method (see Appendix B).

We will call this method the Laplace Expansion Method.

3.5 Mathematical Implementation with Pulsing History

As with the physical modelling, the implementation of the mathematical solution requires some special implementation to enhance its efficiency.

The first such enhancement is to store the solution matrices from one chain to another. The value of this implementation can be seen when considering the solution of many subsequent chains of large rank, n. If each chain differs in only the last branch, all the $n \times n$ transfer matrices would have to be completely recalculated ($n^2/2$ calculations) for each of these subsequent chains. On the other hand, if the transfer matrix solution for each interval is stored after its use in the solution of one chain, only the last row (n calculations) is necessary. This savings carries to all situations throughout the scheme. Since the chains are formed by a depth-first search, it is likely that for each chain, a significant portion of the data has already been determined for a previous calculation.

This is also true for the decay matrices between pulses and after-shutdown, but in this case, the matrices are not only saved between chains, but between intervals for the same chain. Since the decay matrices are independent of flux, they need only be calculated once for each chain and then used in all the intervals for that chain. This has large potential savings since there may be many intervals which share the decay matrices, each recalculation of which would cost n calculations even with the already implemented savings. Furthermore, since the decay matrices are likely to be much sparser than the pulse transfer matrices, a special implementation of the Bateman solution routine to intelligently fill these matrices has been implemented.

Once these methods have been implemented to efficiently calculate the individual transfer matrices for each pulse, each inter-pulse decay period and each after-shutdown decay period, it is straightforward to calculate the total transfer matrix for the entire problem.

First, a single pulse transfer matrix, $\boldsymbol{T}_0$, and a single dwell matrix for the dwell time of the first level of pulsing, $\boldsymbol{D}_1$, are calculated. The product of these, $\boldsymbol{D}_1\boldsymbol{T}_0$, is then raised to a power representing the number of pulses in that level, n_1. This becomes the transfer matrix for the next level, $\boldsymbol{T}_1 = \boldsymbol{T}_0(\boldsymbol{D}_1\boldsymbol{T}_0)^{n_1}$. Now a single dwell matrix for the dwell time of the second level is calculated, $\boldsymbol{D}_2$. This is repeated using the general formula[10]

$$\boldsymbol{T}_i = \boldsymbol{T}_{i-1}(\boldsymbol{D}_i\boldsymbol{T}_{i-1})^{n_i}. \tag{3.23}$$

It is important to use an efficient algorithm[13] for this matrix exponentiation process since it will be performed so often during the operation of the code.

For N levels of pulsing, the matrix, $\boldsymbol{T}_N$, will be the transfer matrix for the entire problem history up to shutdown. Multiplying this matrix by the initial number density, $\vec{N}_o$, results in a final, at-shutdown number density. This final number density vector can then be multiplied by a single dwell matrix for each after-shutdown time to determine the appropriate isotopic compositions.

Acknowledgements

Much of the development used to create ALARA, and in particular, the handling of loops, was inspired by vigorous discussion with the late Prof. Emeritus Charles Maynard. He always insisted that loops were usually not important, and when they were, the solution could be easily found. I am happy to have proven him correct.

Bibliography

[1] P.P.H. Wilson and D.L. Henderson, "Qualitative Analysis of Physical and Mathematical Approximations Necessary for Induced Radioactivity Calculations of Fusion Devices", UWFDM-997, University of Wisconsin Fusion Technology Institute, Madison, Wisconsin (1995).

[2] T.Y. Sung and W.F. Vogelsang, "DKR: A Radioactivity Calculation Code for Fusion Reactors," UWFDM-170, Fusion Technology Institute, University of Wisconsin-Madison, Madison, Wisconsin, September 1976.

[3] D.L. Henderson and O. Yasar, "DKRICF: A Radioactivity and Dose Rate Calculation Code Package: Vols. I & II," UWFDM-714, Fusion Technology Institute, University of Wisconsin-Madison, Madison, Wisconsin, November 1986. This code package is available from the Radiation Shielding Information Center (RSIC) at Oak Ridge National Laboratory as Computer Code Collection entry CCC-323-DKR.

[4] DKR-PULSAR is a new version of the DKR-ICF code which implements methods from Reference 9 for the exact treatment of pulsed history irradiation. It is being developed by D.L. Henderson and H. Khater at the University of Wisconsin–Madson.

[5] P.P.H. Wilson and D.L. Henderson, "Expanding Towards Excellence: Ironing Out DKR's Wrinkles", UWFDM-995, University of Wisconsin Fusion Technology Institute, Madison, Wisconsin (1995).

[6] R.A. Forrest and J-Ch. Sublet, "FISPACT3 - User Manual," AEA/FUS 227, April 1993.

[7] J. Jung, "RACC: Theory and Use of the Radioactivity Code RACC," ANL Report: ANL/FPP/TM-122, May 1979.

[8] H. Attaya, "Input Instructions for RACC-P," ANL Report: ANL/FPP/TM-270, September 1994.

[9] J.E. Sisolak, S.E. Spangler and D.L. Henderson, "Pulsed/Intermittent Activation in Fusion Energy Systems," Fus. Tech. vol. 21, p. 2145 (May 1992).

[10] S.E. Spangler, J.E. Sisolak and D.L. Henderson, "Calculational Models for the Treatment of Pulsed/Intermittent Activation Within Fusion Energy Devices," Fus. Eng. and Design, Vol. 22, p.349 (July 1993).

[11] S.E. Spangler, Master's Thesis, "A Numerical Method for Calculating Nuclide Densities in Pulse Activation Studies," University of Wisconsin-Madison, 1991.

[12] H. Bateman, *Proc. Cambridge Phil. Soc.* **15**: 423 (1910).

[13] E.S. Lee, "Computer Engineering: Computer Algorithms, Data Structures, and Languages," Prepared Notes, University of Toronto, 1989.

Appendices

A Derivation of Recursive Derivative Definition

$$G(s) = \prod_{i=1}^{N} \frac{1}{s+d_i} \tag{A.1}$$

$$\begin{aligned} G'(s) &= \sum_{j=1}^{N} \frac{-1}{s+d_j} \prod_{i=1}^{N} \frac{1}{s+d_i} \\ &= -G(s) \sum_{j=1}^{N} \frac{1}{s+d_j} \end{aligned} \tag{A.2}$$

$$G''(s) = -G'(s) \sum_{j=1}^{N} \frac{1}{s+d_j} + G(s) \sum_{j=1}^{N} (s+d_j)^{-2} \tag{A.3}$$

$$\begin{aligned} G'''(s) &= -G''(s) \sum_{j=1}^{N} \frac{1}{s+d_j} + G'(s) \sum_{j=1}^{N} (s+d_j)^{-2} \\ &\quad + G'(s) \sum_{j=1}^{N} (s+d_j)^{-2} - 2G(s) \sum_{j=1}^{N} (s+d_j)^{-3} \\ &= -G''(s) \sum_{j=1}^{N} \frac{1}{s+d_j} + 2G'(s) \sum_{j=1}^{N} (s+d_j)^{-2} \\ &\quad - 2G(s) \sum_{j=1}^{N} (s+d_j)^{-3} \end{aligned} \tag{A.4}$$

$$\begin{aligned} G''''(s) &= -G'''(s) \sum_{j=1}^{N} \frac{1}{s+d_j} + G''(s) \sum_{j=1}^{N} (s+d_j)^{-2} \\ &\quad + 2G''(s) \sum_{j=1}^{N} (s+d_j)^{-2} - 4G'(s) \sum_{j=1}^{N} (s+d_j)^{-3} \\ &\quad - 2G'(s) \sum_{j=1}^{N} (s+d_j)^{-3} + 6G(s) \sum_{j=1}^{N} (s+d_j)^{-4} \\ &= -G'''(s) \sum_{j=1}^{N} \frac{1}{s+d_j} + 3G''(s) \sum_{j=1}^{N} (s+d_j)^{-2} \\ &\quad - 6G'(s) \sum_{j=1}^{N} (s+d_j)^{-3} + 6G(s) \sum_{j=1}^{N} (s+d_j)^{-4} \end{aligned} \tag{A.5}$$

Thus, for n=4,

$$\begin{aligned} G^{(n)}(s) &= -\frac{(n-1)!}{(n-1)!}G^{(n-1)}(s)\sum_{j=1}^{N}\frac{1}{s+d_j} \\ &+ \frac{(n-1)!}{(n-2)!}G^{(n-2)}(s)\sum_{j=1}^{N}(s+d_j)^{-2} \\ &- \frac{(n-1)!}{(n-3)!}G^{(n-3)}(s)\sum_{j=1}^{N}(s+d_j)^{-3} \\ &+ \frac{(n-1)!}{(n-4)!}G^{(n-4)}(s)\sum_{j=1}^{N}(s+d_j)^{-4} \\ &= \sum_{i=1} n(-1)^i\frac{(n-1)!}{(n-i)!}G^{(n-i)}(s)\sum_{j=1}^{N}(s+d_j)^{-i} \end{aligned} \tag{A.6}$$

A.1 Induction Proof

$$G^{(n)}(s) = \sum_{i=1}^{n}(-1)^i\frac{(n-1)!}{(n-i)!}G^{(n-i)}(s)\sum_{j=1}^{N}(s+d_j)^{-i} \tag{A.7}$$

given

$$G^{(0)}(s) = G(s) = \prod_{j=1}^{N}(s+d_j)^{-1} \tag{A.8}$$

First, we solve for n=1:

$$\begin{aligned} G'(s) &= (-1)\frac{0!}{0!}G(s)\sum_{j=1}^{N}(s+d_j)^{-1} \\ &= -G(s)\sum_{j=1}^{N}(s+d_j)^{-1} \end{aligned} \tag{A.9}$$

which matches Equation A.2.

Now, we solve for n=2:

$$\begin{aligned} G''(s) &= (-1)\frac{1!}{1!}G'(s)\sum_{j=1}^{N}(s+d_j)^{-1} + \frac{1!}{0!}G(s)\sum_{j=1}^{N}(s+d_j)^{-2} \\ &= -G'(s)\sum_{j=1}^{N}(s+d_j)^{-1} + G(s)\sum_{j=1}^{N}(s+d_j)^{-2} \end{aligned} \tag{A.10}$$

which matches Equation A.3.

Now, given $G^{(k)}(s)$, we take the derivative, $G^{(k+1)}(s)$, and see if it matches the correct form:

$$G^{(k+1)}(s) = \sum_{i=1}^{k}(-1)^i \frac{(k-1)!}{(k-i)!}\left[G^{(k-i+1)}\sum_{j=1}^{N}(s+d_j)^{-i} - iG^{(k-i)}\sum_{j=1}^{N}(s+d_j)^{-(i+1)}\right] \tag{A.11}$$

letting, $l = k+1$:

$$\begin{aligned} G^{(l)}(s) = & \sum_{i=1}^{l-1}(-1)^i \frac{(l-2)!}{(l-i-1)!}G^{(l-i)}\sum_{j=1}^{N}(s+d_j)^{-i} \\ & - \sum_{i=1}^{l-1}(-1)^i \frac{(l-2)!}{(l-i-1)!}iG^{(l-i-1)}\sum_{j=1}^{N}(s+d_j)^{-(i+1)} \end{aligned} \tag{A.12}$$

Now, letting $m = i+1$ in the second sum:

$$\begin{aligned} G^{(l)}(s) = & \sum_{i=1}^{l-1}(-1)^i \frac{(l-2)!}{(l-i-1)!}G^{(l-i)}\sum_{j=1}^{N}(s+d_j)^{-i} \\ & + \sum_{m=2}^{l}(-1)^m \frac{(l-2)!}{(l-m)!}(m-1)G^{(l-m)}\sum_{j=1}^{N}(s+d_j)^{-m} \end{aligned} \tag{A.13}$$

and recombining the sums:

$$\begin{aligned} G^{(l)}(s) = & -\frac{(l-2)!}{(l-2)!}G^{(l-1)}(s)\sum_{j=1}^{N}(s+d_j) \\ & + \sum_{i=2}^{l-1}(-1)^i\left[\frac{(l-2)!}{(l-i-1)!} + (i-1)\frac{(l-2)!}{(l-i)!}\right]G^{(l-i)}\sum_{j=1}^{N}(s+d_j)^{-i} \\ & + (-1)^l(l-2)!(l-1)G(s)\sum_{j=1}^{N}(s+d_j)^{-l} \end{aligned} \tag{A.14}$$

$$\begin{aligned} = & -G^{(l-1)}(s)\sum_{j=1}^{N}(s+d_j)^{-1} \\ & + \sum_{i=2}^{l-1}(-1)^i\left[(l-i)\frac{(l-2)!}{(l-i-1)!(l-i)} + (i-1)\frac{(l-2)!}{(l-i)!}\right]G^{(l-i)}\sum_{j=1}^{N}(s+d_j)^{-i} \\ & + (-1)^l(l-1)!G(s)\sum_{j=1}^{N}(s+d_j)^{-l} \end{aligned} \tag{A.15}$$

$$= -G^{(l-1)}(s)\sum_{j=1}^{N}(s+d_j)^{-1}$$
$$+\sum_{i=2}^{l-1}(-1)^i\frac{(l-1)!}{(l-i)!}G^{(l-i)}\sum_{j=1}^{N}(s+d_j)^{-i} \tag{A.16}$$
$$+(-1)^l(l-1)!G(s)\sum_{j=1}^{N}(s+d_j)^{-l}$$
$$=\sum_{i=1}^{l}(-1)^i\frac{(l-1)!}{(l-i)!}G^{(l-i)}\sum_{j=1}^{N}(s+d_j)^{-i} \tag{A.17}$$

QED.

B Other Forms of $1/s$ Expansion

The $1/s$ expansion from Section 3.4 can take on many slightly different forms providing different methods for determining the coefficients. First, it is instructive to relate the expansion as shown in Equation 3.21 to a simple difference of exponentials. Starting with the Bateman solution (Equation 3.10) for a single matrix element,

$$T_{31} = \frac{P_2(e^{-d_1t}-e^{-d_3t})}{d_3-d_1}\frac{P_3}{d_2-d_1} + \frac{P_3(e^{-d_2t}-e^{-d_3t})}{d_3-d_2}\frac{P_2}{d_1-d_2} \tag{3.12}$$

and using the standard expansion for the exponential, we get

$$
\begin{aligned}
&= P_2 P_3 \left[\frac{1 - d_1 t + \frac{(d_1 t)^2}{2} - \frac{(d_1 t)^3}{6} - 1 + d_3 t - \frac{(d_3 t)^2}{2} + \frac{(d_3 t)^3}{6} + \dots}{(d_3 - d_1)(d_2 - d_1)} \right. \\
&\qquad \left. + \frac{1 - d_2 t + \frac{(d_2 t)^2}{2} - \frac{(d_2 t)^3}{6} - 1 + d_3 t - \frac{(d_3 t)^2}{2} + \frac{(d_3 t)^3}{6} + \dots}{(d_3 - d_2)(d_1 - d_2)} \right] \\
&= P_2 P_3 \left[\frac{(d_3 - d_1)[t - (d_3 + d_1)\frac{t^2}{2} + (d_3^2 + d_3 d_1 + d_1^2)\frac{t^3}{6} + \dots]}{(d_3 - d_1)(d_2 - d_1)} \right. \\
&\qquad \left. + \frac{(d_3 - d_2)[t - (d_3 + d_2)\frac{t^2}{2} + (d_3^2 + d_3 d_2 + d_2^2)\frac{t^3}{6} + \dots]}{(d_3 - d_2)(d_1 - d_2)} \right] \\
&= P_2 P_3 \left[\frac{(d_2 - d_1)\frac{t^2}{2} + [d_3(d_1 - d_2) + (d_1^2 - d_2^2)]\frac{t^3}{6} + \dots}{d_2 - d_1} \right] \\
&= P_2 P_3 \left[\frac{t^2}{2} - (d_3 + d_2 + d_1)\frac{t^3}{6} + \dots \right] \\
&= P_2 P_3 \, t^2 \left[\frac{1}{2} - \frac{t}{6}(d_3 + d_2 + d_1) + \dots \right]
\end{aligned}
\tag{B.1}
$$

which has the form of Equation 3.21.

Whether in the Laplace Transform domain or the time domain, there is a necessity to calculate coefficients of the form:

$$
\{c_i\} = \left\{ \sum_{j=1}^{N} d_j \ , \ \sum_{j=1}^{N} d_j \sum_{k=j}^{N} d_k \ , \ \sum_{j=1}^{N} d_j \sum_{k=j}^{N} d_k \sum_{l=k}^{N} d_l \ , \ \dots \right\} \tag{B.2}
$$

A different form for these coefficients becomes apparent when $N = 2$ or $N = 3$. The coefficients, $\{c_i\}$, are:

$$
\{c_i\} = \left\{ d_1 + d_2 \ , \ d_1(d_1 + d_2) + d_2^2 \ , \ d_1 \left[d_1(d_1 + d_2) + d_2^2 \right] + d_2^3 \ , \dots \right\} \tag{B.3}
$$

or

$$\{c_i\} = \Big\{ d_1 + d_2 + d_3,\ d_1(d_1 + d_2 + d_3) + d_2(d_2 + d_3) + d_3^2,$$

$$d_1\left[d_1(d_1 + d_2 + d_3) + d_2(d_2 + d_3) + d_3^2\right] + d_2\left[d_2(d_2 + d_3) + d_3^2\right] + d_3^3\ , \ldots \Big\} \quad \text{(B.4)}$$

This shows the following pattern, assuming $\{\lambda_{0,j}\} = 1;\ j = [1, N]$:

$$\lambda_{ij} = \sum_{k=j}^{N} d_k \lambda_{i-1,k} \quad \text{(B.5)}$$

$$c_i = \lambda_{i1} \quad \text{(B.6)}$$

This last form leads to an efficient way to calculate these coefficients using matrix multiplcations. If we form a matrix, M, with elements $m_{ij} = d_j; j \geq i$:

$$\boldsymbol{M} = \begin{bmatrix} d_1 & d_2 & d_3 & \ldots & d_N \\ 0 & d_2 & d_3 & \ldots & d_N \\ 0 & 0 & d_3 & \ldots & d_N \\ \vdots & & & \ddots & \vdots \\ 0 & 0 & 0 & \ldots & d_N \end{bmatrix}, \quad \text{(B.7)}$$

it is clear that $\lambda_1 = [\boldsymbol{M} \cdot \vec{1}]$ and that $\lambda_i = [\boldsymbol{M}^i \cdot \vec{1}]$. Therefore,

$$c_i = \lambda_{i1} = \left[M^i \cdot \vec{1}\right]_1 . \quad \text{(B.8)}$$

Since the direct calculation of

$$\sum_{j_1=1}^{N} d_{j_1} \sum_{j_2=j_1}^{N} d_{j_2} \sum_{j_3=j_2}^{N} d_{j_3} \cdots \sum_{j_{n-1}=j_{n-2}}^{N} d_{j_{n-1}} \sum_{j_n=j_{n-1}}^{N} d_{j_n} = \prod_{l=n}^{1} \sum_{j_l=j_{l-1}}^{N} d_{j_l} \quad \text{(B.9)}$$

tends to require $O(N^n)$ calculations, the matrix method above will be highly advantageous

since it requires only $O(nN^3)$ calculations.

Once these coefficients have been calculated, they are then used to calculate the time response using Equation 3.21:

$$f(t) = t^n \left[\frac{1}{n!} - \frac{t}{(n+1)!} \sum_{l=j}^{i} d_l + \frac{t^2}{(n+2)!} \sum_{l=j}^{i} d_l \sum_{k=l}^{i} d_k - \frac{t^3}{(n+3)!} \sum_{l=j}^{i} d_l \sum_{k=l}^{i} d_k \sum_{m=k}^{i} d_m + \cdots \right]. \tag{3.21}$$

C ALARA_DC: Data Conversion for Code Interfacing

In designing ALARA for maximum usability, consideration was taken for the way that it would be implemented by the end user. Most important was to consider the origins of the various inputs which would be needed to complete each calculation. Every ALARA problem requires four distinct types of input:

1. cross-section, decay and gamma libraries
2. geometry/mixture definitions
3. groupwise flux input
4. pulsing and history information

By facilitating the conversion of these various inputs from other standard formats to that required by ALARA, the ease of use for the end user is enhanced. Such conversions are available for input types 1-3, while input type 4, pulsing and history information is particular to the pusled history activation calculation. ALARA Data Conversion [ALARA_DC] is being written with these conversion needs in mind.

It was originally written to convert the cross-section, decay and gamma data from various international standard text formats to the proprietary data format required by ALARA (see Appendix D for binary data format). However, because the geometry definitions are required

in various formats for neutron transport calculations which generate the groupwise fluxes in various formats, ALARA_DC is being extended to convert these data as well.

While most transport calculations do require geometry definitions at least as specific as those needed by ALARA, the mixture definitions often lack certain trace elemental quantities which are unimportant for transport calculations but may be important for activation calculations. For example, a transport calculation through a steel block may define the mixture as iron for the purpose of the transport calculation while the alloying concentrations of nickel, chromium, and other elements are very important in determining the activation characteristics of the material. Therefore, ALARA_DC will be designed to extract the geometry definitions from the transport calculation and allow the user to modify/upgrade the mixture definition. In different cases, this geometry information may be extracted from either transport calculation input (deterministic calculations) or output (Monte Carlo calculations with combinatorial geometries).

The flux data can also take a number of different formats. Some of the available codes share standard binary and/or text based data formats for these results while others have their own formats. ALARA_DC will be extended to first convert the standard shared formats and then the more popular unique formats. In some cases, this conversion will be simultaneous to the geometry conversion, and in others, the fluxes will be interactively extracted from the available output.

D Binary Reaction Library Format

Because the reaction schemes/chains are created by a depth first search using the data from the transmutation and decay libraries, these libraries need to be accessed extensively and randomly. In the past, such random access was not possible because of the limits on mass storage devices. Currently, in a text format, such random access would still be very tedious. To ensure that this random access does not create a drag on ALARA, it is necessary to either store the entire library in memory or use a binary file format. Because the libraries are often

quite large (many MB) a simple binary format was designed. This section will describe the formats for the binary files and their indexes, which are generated in a text format and then appended in binary format to the end of the binary library.

The format of the binary file will be described by listing, in order, the data written to the file using the format: *(data type)*Description[**size**].

D.1 Transmutation Library

- *(long)*File Position of Index[**1**]
- *(int)*Number of Parent Isotopes[**1**]
- *(int)*Number of Neutron Energy Groups[**1**]
- *(int)*Flag indicating existence of Group Boundary info[**1**]
- *(float)*Group Boundary Data[**Number of Groups + 1** if above flag]
- *(int)*Flag indicating existence of Integral Flux Data[**1**]
- *(float)*Integral Flux Data[**Number of Groups** if above flag].
- Parent Isotope Info
  - *(int)*Parent KZA[**1**]
  - *(int)*Number of Reactions[**1**]
  - Reaction info once for each reaction
    - *(int)*Daughter KZA[**1**]
    - *(char)*Emitted Particles[**6**]
    - *(float)*Cross-section Data[**Number of Groups**]

This is followed by the index:

- *(char)*Library Type[**1**]
- *(int)*Number of Parent Isotopes[**1**]
- *(int)*Number of Neutron Energy Groups[**1**]
- *(int)*Special Code for Group Boundary Data[**1**]
- *(long)*File Index of Group Boundary Data[**1**]
- *(int)*Special Code for Integral Flux Data[**1**]
- *(long)*File Index of Integral Flux Data[**1**]

- Parent Index Info
  - *(int)*Parent KZA[**1**]
  - *(int)*Number of Reactions[**1**]
  - *(long)*File Index of This Parent[**1**]
  - Reaction info once for each reaction
    - *(int)*Daughter KZA[**1**]
    - *(char)*Emitted Particles[**6**]
    - *(long)*File Index of This Reaction[**1**]

D.2 Decay Library

- *(long)*File Position of Index[**1**]
- *(int)*Number of Parent Isotopes[**1**]
- Parent Isotope Info
  - *(int)*Parent KZA[**1**]
  - *(int)*Number of Decay Paths[**1**]
  - *(float)*Half Life[**1**]
  - *(float)*Average Beta Energy[**1**]
  - *(float)*Average Gamma Energy[**1**]
  - *(float)*Average Alpha Energy[**1**]
  - Reaction info once for each decay path
    - *(int)*Daughter KZA[**1**]
    - *(char)*Daughter Flag[**1**]
    - *(float)*Branching Ratio[**1**]

This is followed by the index:

- *(char)*Library Type[**1**]
- *(int)*Number of Parent Isotopes[**1**]
- Parent Index Info
  - *(int)*Parent KZA[**1**]
  - *(int)*Number of Decay Paths[**1**]
  - *(long)*File Index of This Parent[**1**]
  - Reaction info once for each decay path
    - *(int)*Daughter KZA[**1**]
    - *(char)*Daughter Flag[**1**]
    - *(long)*File Index of This Decay Path[**1**]

D.3 Mixed Reaction Library

- *(long)*File Position of Index[**1**]
- *(int)*Number of Parent Isotopes[**1**]
- *(int)*Number of Neutron Energy Groups[**1**]
- *(int)*Flag indicating existence of Group Boundary info[**1**]
- *(float)*Group Boundary Data[**Number of Groups** + **1** if above flag]
- *(int)*Flag indicating existence of Integral Flux Data[**1**]
- *(float)*Integral Flux Data[**Number of Groups** if above flag].
- Parent Isotope Info
  - *(int)*Parent KZA[**1**]
  - *(int)*Number of Transmutation Reactions[**1**]
  - *(int)*Number of Decay Paths[**1**]
  - Reaction info once for each transmutation reaction
    - *(int)*Daughter KZA[**1**]
    - *(char)*Emitted Particles[**6**]
    - *(float)*Cross-section Data[**Number of Groups**]
  - Reaction info once for each decay path
    - *(int)*Daughter KZA[**1**]
    - *(char)*Daughter Flag[**1**]
    - *(float)*Branching Ratio[**1**]

This is followed by the index:

- *(char)*Library Type[**1**]
- *(int)*Number of Parent Isotopes[**1**]
- *(int)*Number of Neutron Energy Groups[**1**]
- *(int)*Special Code for Group Boundary Data[**1**]
- *(long)*File Index of Group Boundary Data[**1**]
- *(int)*Special Code for Integral Flux Data[**1**]
- *(long)*File Index of Integral Flux Data[**1**]
- Parent Index Info

- *(int)*Parent KZA[**1**]
- *(int)*Number of Transmutation Reactions[**1**]
- *(int)*Number of Decay Paths[**1**]
- *(long)*File Index of This Parent[**1**]
- Reaction info once for each transmutation reaction
  - *(int)*Daughter KZA[**1**]
  - *(char)*Emitted Particles[**6**]
  - *(long)*File Index of This Reaction[**1**]
- Reaction info once for each decay path
  - *(int)*Daughter KZA[**1**]
  - *(char)*Daughter Flag[**1**]
  - *(long)*File Index of This Decay Path[**1**]

D.4 Gamma Source Library

- *(long)*File Position of Index[**1**]
- *(int)*Number of Parent Isotopes[**1**]
- Parent Isotope Info
  - *(int)*Parent KZA[**1**]
  - *(int)*Number of Spectra[**1**]
  - *(int)*Number of Discrete Gammas in each Spectra[**Number of Spectra**]
  - *(int)*Number of Interpolation Regions in each Spectra[**Number of Spectra**]
  - *(int)*Number of Interpolation Points in each Spectra[**Number of Spectra**]
  - Reaction info once for each spectrum
    - *(float)*Discrete Gamma Energies[**Number of Discrete Gammas(i)**]
    - *(float)*Discrete Gamma Intensities[**Number of Discrete Gammas(i)**]
    - *(float)*Interpolation Region Boundaries[**Number of Interpolation Regions(i)**]
    - *(float)*Interpolation Region Types[**Number of Interpolation Regions(i)**]
    - *(float)*Interpolation Point X-values[**Number of Interpolation Points(i)**]
    - *(float)*Interpolation Point Y-values[**Number of Interpolation Points(i)**]

This is followed by the index:

- *(char)*Library Type[**1**]
- *(int)*Number of Parent Isotopes[**1**]
- Parent Index Info

- *(int)*Parent KZA[**1**]
- *(int)*Number of Spectra[**1**]
- *(long)*File Index of This Parent[**1**]
- Reaction info once for each Spectra
  - *(int)*Number of Discrete Gammas[**1**]
  - *(int)*Number of Interpolation Regions[**1**]
  - *(int)*Number of Interpolation Points[**1**]

D.5 Adjoint Library

- *(long)*File Position of Index[**1**]
- *(int)*Number of Daughter Isotopes[**1**]
- *(int)*Number of Neutron Energy Groups[**1**]
- *(int)*Flag indicating existence of Group Boundary info[**1**]
- *(float)*Group Boundary Data[**Number of Groups + 1** if above flag]
- *(int)*Flag indicating existence of Integral Flux Data[**1**]
- *(float)*Integral Flux Data[**Number of Groups** if above flag].
- Daughter Isotope Info
  - *(int)*Daughter KZA[**1**]
  - *(int)*Number of Transmutation Reactions to this Daughter[**1**]
  - *(int)*Number of Decay Paths to this Daughter[**1**]
  - Reaction info once for each transmutation reaction
    - *(int)*Parent KZA[**1**]
    - *(char)*Emitted Particles[**6**]
    - *(float)*Cross-section Data[**Number of Groups**]
  - Reaction info once for each decay path
    - *(int)*Parent KZA[**1**]
    - *(char)*Daughter Flag[**1**]
    - *(float)*Branching Ratio[**1**]

This is followed by the index:

- *(char)*Library Type[**1**]
- *(int)*Number of Daughter Isotopes[**1**]
- *(int)*Number of Neutron Energy Groups[**1**]

- *(int)*Special Code for Group Boundary Data[**1**]
- *(long)*File Index of Group Boundary Data[**1**]
- *(int)*Special Code for Integral Flux Data[**1**]
- *(long)*File Index of Integral Flux Data[**1**]
- Daughter Index Info
  - *(int)*Daughter KZA[**1**]
  - *(int)*Number of Transmutation Reactions to this Daughter[**1**]
  - *(int)*Number of Decay Paths to this Daughter[**1**]
  - *(long)*File Index of This Daughter[**1**]
  - Reaction info once for each transmutation reaction
    - *(int)*Parent KZA[**1**]
    - *(char)*Emitted Particles[**6**]
    - *(long)*File Index of This Reaction[**1**]
  - Reaction info once for each decay path
    - *(int)*Parent KZA[**1**]
    - *(char)*Daughter Flag[**1**]
    - *(long)*File Index of This Decay Path[**1**]

The repitition of much of this data in the index as well as the files allows the simple reading and extracting of the index without jumping back and forth in the binary file.

U.S. Department of Energy

Contract No. DE-AS08-88DP10754

The Development and Application of
Advanced Analytical Methods
to Commercial ICF Reactor Chambers

Task 4
Final Report

Structural Dynamics Modeling of ICF Reactor Chambers

Fusion Technology Institute
University of Wisconsin-Madison

4.1 Introduction

The design of an inertial confinement fusion (ICF) reaction chamber involves identifying the structural response of the containment vessel to intense thermal and mechanical loads as energy is released from the implosion. The Fusion Technology Institute (FTI) has been involved with a number of ICF reactor designs over the last fifteen years. The response of the first wall to an impulsive pressure or thermal shock is a critical issue and has been included in nearly all of the reactor designs. The primary mechanism for simulating the mechanical response of the chamber has been numerical computer codes developed for each of the individual designs. Whenever possible the finite element codes have been verified with analytical and experimental data. The intent of this research is to extend existing programs and generate new codes in parametric form so that software packages can be made available to the ICF community. Consequently, the user may easily change geometry, materials, boundary conditions or loading conditions to arrive at the final design.

The code development effort has been divided into the following four areas:

A) Cylindrical shells
B) Spherical shells
C) Hemispherical shells
D) Perforated Plates
E) Reactor components (beam/cooling tubes)

Under the guidance of Professor R. L. Engelstad, three graduate students and one undergraduate student have investigated different areas of ICF chamber design during the course of this contract. Cylindrical shells are being studied using finite element and experimental methods by Cousseau for his Ph.D. thesis [1] and results will be presented at the 16th International Modal Analysis Conference (IMAC) [2]. In collaboration with Professor P. Peterson from the University of California - Berkeley, results for spherical shells were reported at the 12th Topical Meeting on the Technology of Fusion Power [3]. Hemispherical shells were investigated by Sprague and results are presenting in his undergraduate thesis [4]. Perforated plates were studied using finite element and experimental techniques by Kaap and results are presented in his M.S. thesis [5] and at the 16th IMAC [6]. Results for reactor components, specifically beam cooling tubes have been presented at 16th IEEE/NPSS Symposium on Fusion Engineering [7]. This report presents a summary of the completed work in each of these areas.

4.2 Cylindrical Shells

4.2.1 Unperforated Cylindrical Shells

Many investigators have developed the differential equations of motion which describe the behavior of thin shells. An extensive publication by Leissa [8] is a compilation of a wealth of information about shell vibrations, primarily cylindrical shells. Forsberg [9, 10] and Ludwig and Krieg [11] considered the effect of various boundary conditions on the natural frequencies of cylindrical shells, including axisymmetric cases, using quasi-exact methods. More recently, Powers [12] studied the use of equivalent elastic properties to model the dynamic response of perforated cylinders. Adler [13] used a variety of boundary conditions on a cylindrical shell to show their effects on frequencies and mode shapes. He showed that boundary conditions can affect cylindrical shell frequencies and mode shapes in unexpected ways; natural frequencies change only slightly when various end conditions are applied, although mode shapes can vary greatly. Since the loading of the reaction chamber is primarily axisymmetric, the response to this type of excitation will be considered in the code development work.

Figure 4.1 shows the schematic of a cylindrical shell with the axial, circumferential and radial directions denoted by x, θ, and z, respectively. The corresponding displacements are given by u, v, and w. In addition, the shell dimensions are given by the following: h is the thickness, R is the radius, and L is the length. Material properties use E for elastic modulus, ρ for density, and υ for Poisson's ratio.

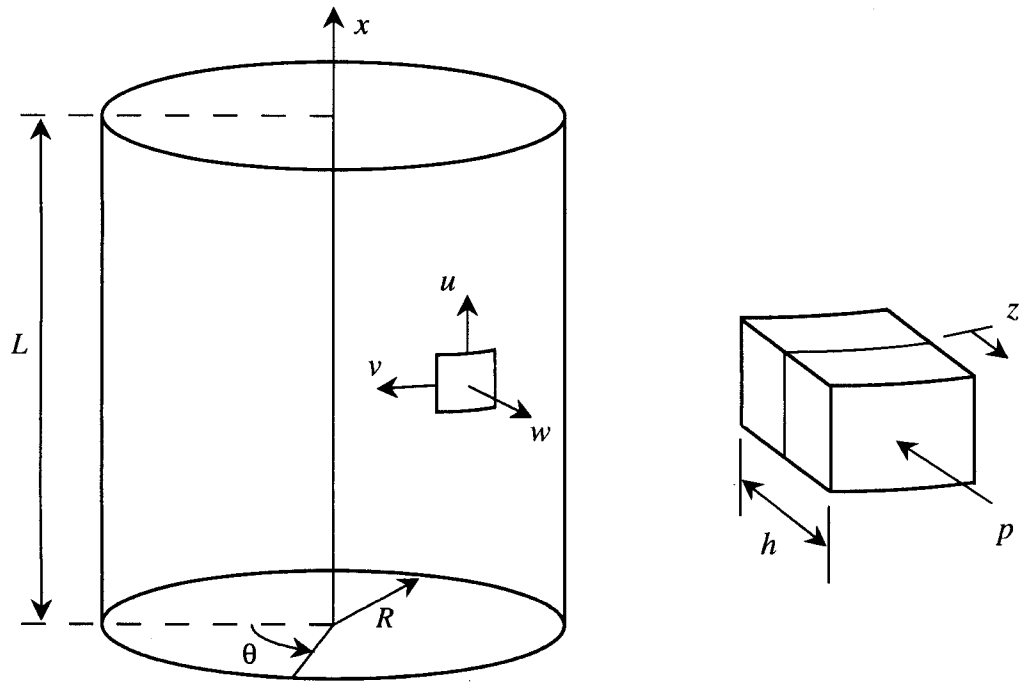

Fig. 4.1. Cylindrical coordinate system and displacement components.

There are many different formulations of the general differential equations of motion for thin shell vibrations (Love, Flugge, Timoshenko, Sanders, etc.). The analyses follow the common assumptions of linear thin shell theory proposed by Love [14], i.e., the cylinder is assumed to be thin ($R/h>10$), of constant wall thickness and made of a linear, isotropic, homogeneous material. The equations as developed by Sanders are:

$$\begin{bmatrix} K_{11} & K_{12} & K_{13} \\ K_{21} & K_{22} & K_{23} \\ K_{31} & K_{32} & K_{33} \end{bmatrix} \begin{Bmatrix} u(x,\theta,t) \\ v(x,\theta,t) \\ w(x,\theta,t) \end{Bmatrix} = \frac{\rho(1-\upsilon^2)R^2}{E}\frac{\partial^2}{\partial t^2}\begin{Bmatrix} u(x,\theta,t) \\ v(x,\theta,t) \\ -w(x,\theta,t) \end{Bmatrix} + \frac{(1-\upsilon^2)R^2}{Eh}\begin{Bmatrix} 0 \\ 0 \\ p(x,\theta,t) \end{Bmatrix}$$

where

$$K_{11} = R^2\frac{\partial^2}{\partial x^2} + (1-\upsilon)\left[\frac{1}{2} + k\frac{1}{8}\right]\frac{\partial^2}{\partial\theta^2}$$

$$K_{12} = K_{21} = R\left[\frac{(1+\upsilon)}{2} - k\frac{3(1-\upsilon)}{8}\right]\frac{\partial^2}{\partial x\partial\theta}$$

$$K_{13} = K_{31} = \upsilon R\frac{\partial}{\partial x} + kR\frac{(1-\upsilon)}{2}\frac{\partial^3}{\partial x\partial\theta^2}$$

$$K_{22} = R^2(1-\upsilon)\left[\frac{1}{2} + k\frac{9}{8}\right]\frac{\partial^2}{\partial x^2} + (1+k)\frac{\partial^2}{\partial\theta^2}$$

$$K_{23} = K_{32} = \frac{\partial}{\partial\theta} - k\frac{\partial^3}{\partial\theta^3} - kR^2\frac{(3-\upsilon)}{2}\frac{\partial^3}{\partial x^2\partial\theta}$$

$$K_{33} = 1 + k\left[R^4\frac{\partial^4}{\partial x^4} + 2R^2\frac{\partial^4}{\partial x^2\partial\theta^2} + \frac{\partial^4}{\partial\theta^4}\right]$$

Markus [15] describes Sanders equations as "the best first order equations describing the deformations of cylindrical shells". In the case of axisymmetric vibrations, the differential equations can be separated, or decoupled, from an 8th order equation to a 6th order and a 2nd order equation. A finite element model of a thin cylindrical shell with no holes was created and compared with previous studies and known analytical solutions; agreement was excellent.

4.2.2 Perforated Cylindrical Shells - Problem Description

The two most common perforation patterns are triangular and rectangular as shown in Figs. 4.2 and 4.3, respectively. The shaded area represents a unit cell; in the case of the triangular pattern the cell is hexagonal and for a rectangular perforation pattern the cell is rectangular. Each cell has one perforation, a circular hole with radius a. To complete the perforation pattern, the unit cell is replicated over the pattern region. The pattern's void fraction is defined as the percent of total mass (or area) removed when creating the perforation pattern.

In this study, the entire surface area of the cylindrical shell is covered uniformly by the perforation pattern. The circumferential distance between hole centers, i.e., the pitch P_θ, must be an integer fraction of the circumference of the cylinder to insure continuity of the pattern. Also when the perforation pattern extends to the ends of the cylinder the axial distance between hole centers, i.e., the pitch P_x, must be an integer fraction of the length. No known analytical solution exists for thin cylindrical shells with perforation patterns.

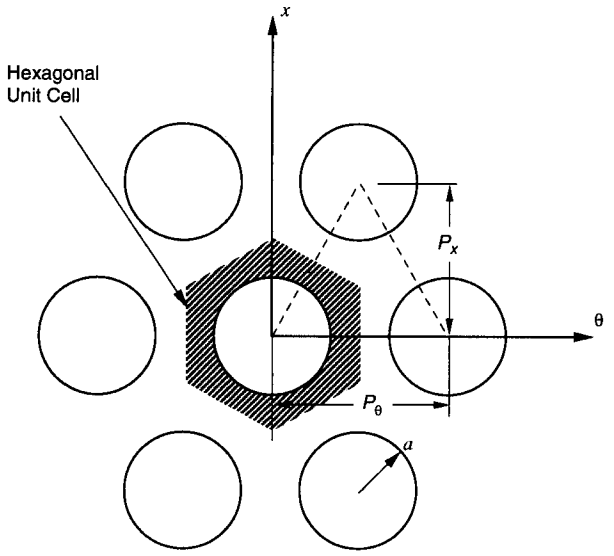

Fig. 4.2. Triangular perforation pattern.

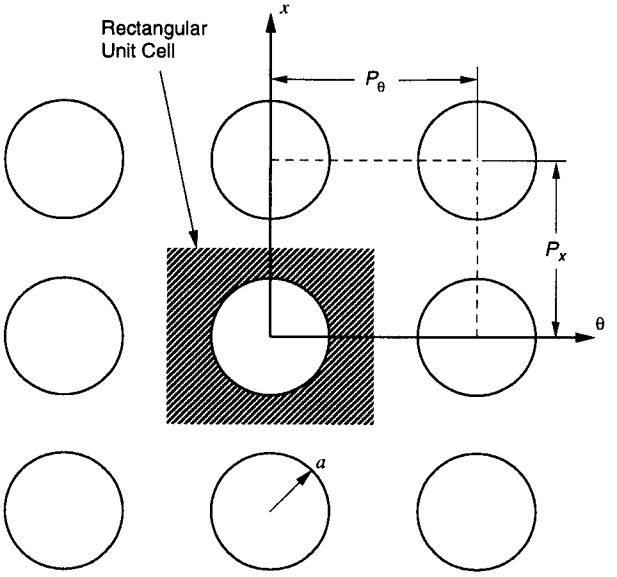

Fig. 4.3. Rectangular perforation pattern.

4.2.3 Perforated Finite Element Model

The finite element method was used to study the effects of perforations on the natural frequencies of cylinder shells. The commercially available finite element (FE) software ANSYS® was used to perform a modal analyses. All FE models were generated with eight-noded elastic shell elements. Perforation patterns on two different cylindrical geometries were studied:

$$\text{Case 1: } \frac{R}{h} = 200, \quad \frac{L}{R} = \frac{11\pi\sqrt{3}}{3} \cong 19.95$$

$$\text{Case 2: } \frac{R}{h} = 200, \quad \frac{L}{R} = \frac{4\pi\sqrt{3}}{11} \cong 1.98$$

The length-to-radius ratios of the cylinders are irrational to accommodate the exact dimensions of the perforation pattern. Both cylinders have the same thickness (5 mm) to aid in comparing the results of the two cases. The length-to-radius ratios were chosen to compare different types of cylindrical shell behavior: the Case 1 cylinder was long and beam-like, the Case 2 cylinder was short and square. For each case triangular and rectangular perforation patterns were used. Figure 4.4 shows a Case 1 cylinder with a rectangular perforation pattern and a 40% void fraction. Figure 4.5 shows a Case 2 cylinder with a triangular perforation pattern and a 20% void fraction. A rectangular pattern has to be used instead of a square pattern to fit both types of patterns on the same length cylinder. The number of holes in the patterns was varied between 25 and 825 while keeping the void fraction constant. Void fractions of 20% and 40% were considered.

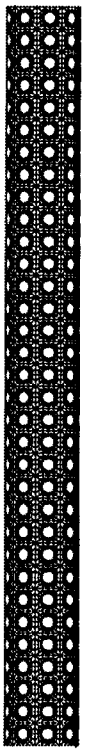

Fig. 4.4. Finite element model of a Case 1 cylinder with a rectangular perforation pattern, 40% void fraction, 14,256 elements.

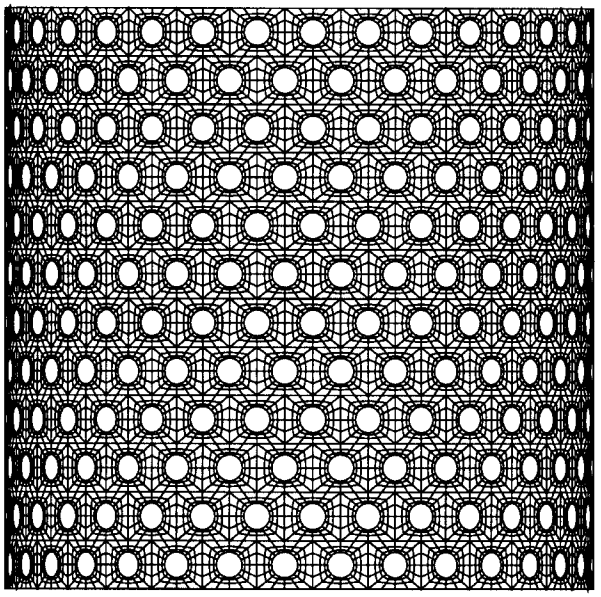

Fig. 4.5. Finite element model of a Case 2 cylinder with a triangular perforation pattern, 20% void fraction, 19,008 elements.

4.2.4 Perforated Finite Element Results

Figure 4.6 illustrates a typical mode shape of a cylinder with a rectangular perforation pattern. Figure 4.7 shows the finite element results for the change in natural frequencies of the lowest three modes of a simply supported Case 1 cylinder. The solid symbols on the vertical axis represent the unperforated natural frequencies; the dashed and solid curves illustrate the natural frequencies for the rectangular perforation pattern with 40% and 20% void fraction, respectively. Figure 4.8 shows similar results for a simply supported Case 2 cylinder.

4.2.5 Experimental Setup and Procedure

Impact testing of perforated cylinders was used to verify the finite element results and characterize the natural frequencies of cylinders with completely different hole patterns but the same void fraction. Figure 4.9 shows the three cylinders tested. From left to right, the first is an unperforated aluminum cylinder used to benchmark the experimental setup. The next two are commercially manufactured perforated cylinders provided by Perforated Tubes, Inc., Ada, Michigan. The cylinders are stainless steel with 33% and 23% void fractions, respectively.

Impulse testing was performed by attaching accelerometers to the cylinders using a wax adhesive. The commercial software package, Snapmaster, was used to acquire the voltage signals created by the accelerometers; FFT algorithms provided by the software package Matlab were used to transform the voltage signal into the frequency spectrum. The positions of the accelerometers were chosen using a reference grid on the cylinder. The intersections of the grid lines were designed to fall upon node and antinode positions of the cylinder. The free response due to an impulse was measured by the accelerometers with the cylinders supported to simulate free-free boundary conditions. Initial impulse testing was performed to identify the optimum mass and stiffness of the impact hammer. Because the accuracy of the FFT used to determine the natural frequencies is inversely proportional to the sample time, it was important to create an impulse providing the maximum response time of the cylinder.

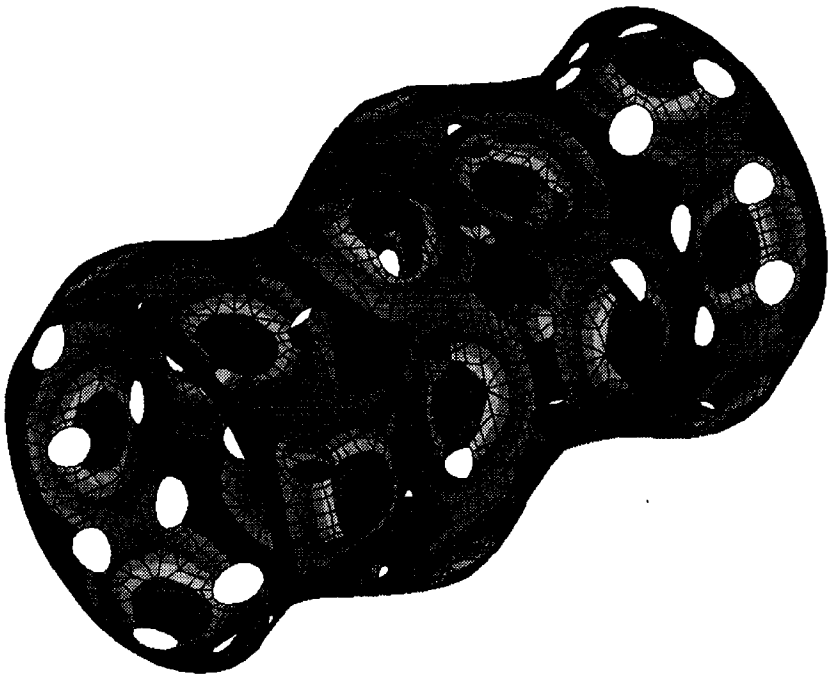

Fig. 4.6. Mode shape of a simply supported cylinder with a square perforation pattern.

4.2.6 Experimental Results

Tables 4.1 - 4.3 compare the experimental and finite element results of the lowest modes of each cylinder. The unperforated cylinder used for benchmarking shows excellent correlation between the experimental and finite element values. The FE model of the perforated cylinder does not exactly duplicate the experimental cylinder in hole location or size but the void fraction was identical. Good correlation between the experimental and finite element data was found. A source of possible experimental error was the helical weld present on the manufactured cylinders which was not present in the FE model.

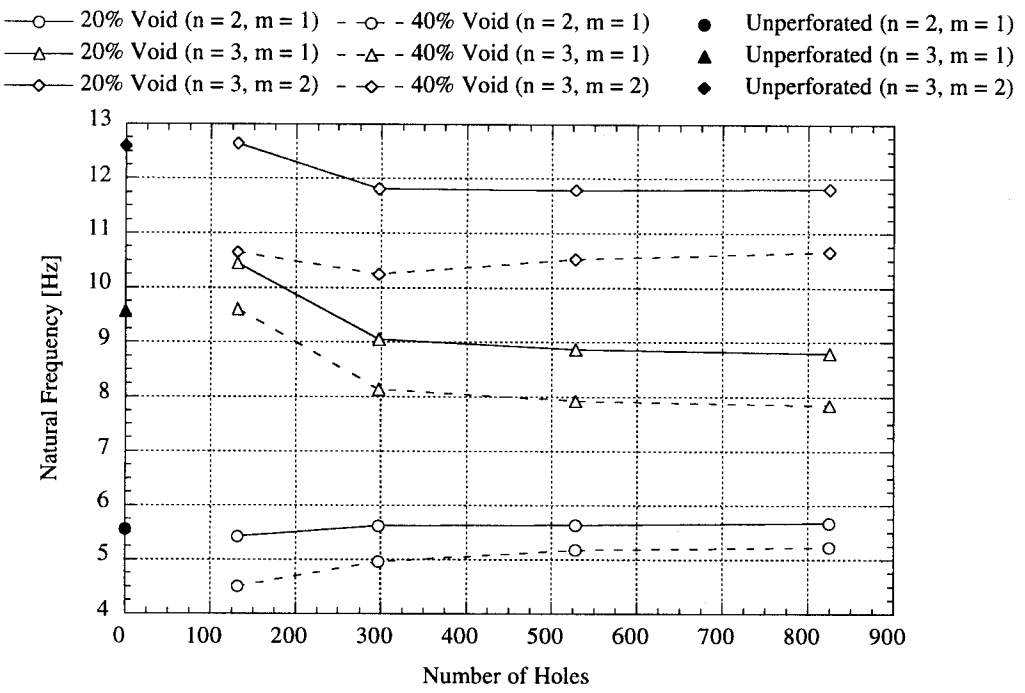

Fig. 4.7. Case 1 cylinder - the change in natural frequency with increasing number of holes ($E = 70\times10^9$ N/m^2, $\rho = 2700$ kg/m^3, $\upsilon = 0.3$). All data is for a square perforation pattern.

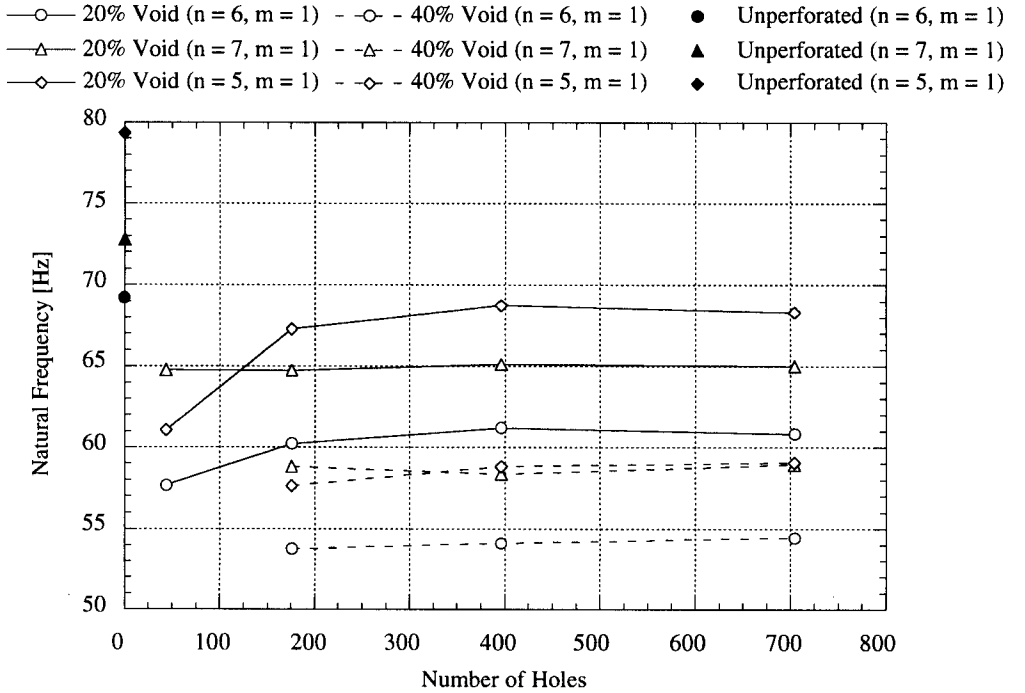

Fig. 4.8. Case 2 cylinder - the change in natural frequency with increasing number of holes ($E = 70\times10^9$ N/m^2, $\rho = 2700$ kg/m^3, $\upsilon = 0.3$). All data is for a square perforation pattern.

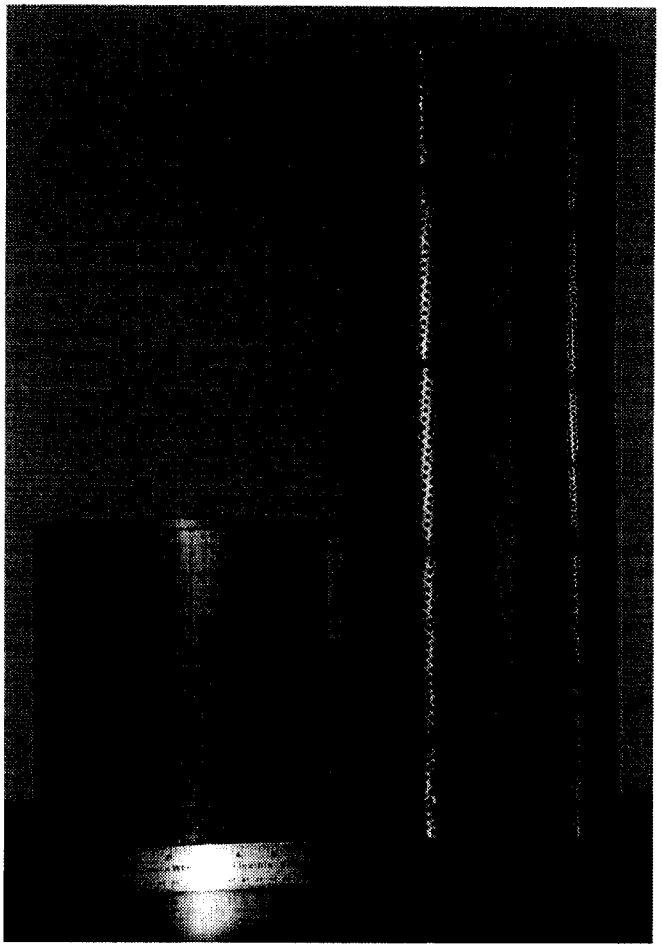

Fig. 4.9. The three cylinders used in the experimental procedure.

Table 4.1. Natural Frequencies of the Unperforated Aluminum Cylinder with Free-Free Boundary Conditions (E = 70 GPa, υ = 0.33, ρ = 2700 kg/m^3, L = 26.0 cm, R = 10.46 cm, h = 0.84 cm).

n m	Finite Element [Hz]	Experimental [Hz]	Percent Difference
2 1	504	503	< 1%
2 2	615	605	2%
3 1	1417	1412	< 1%
3 2	1584	1593	-1%

Table 4.2. Natural Frequencies of the Perforated Stainless Steel Cylinder (33% Void Fraction) with Free-Free Boundary Conditions (E = 190 GPa, υ = 0.3, ρ = 7920 kg/m^3, L = 60.5 cm, R = 3.11 cm, h = 0.107 cm).

n m	Finite Element [Hz]	Experimental [Hz]	Percent Difference
2 1	329	313	5%
2 2	333	320	4%
2 3	560	553	1%

Table 4.3. Natural Frequencies of the Perforated Stainless Steel Cylinder (23% Void Fraction) with Free-Free Boundary Conditions (E = 190 GPa, υ = 0.3, ρ = 7920 kg/m^3, L = 60.5 cm, R = 5.17 cm, h = 0.157 cm).

n m	Finite Element [Hz]	Experimental [Hz]	Percent Difference
2 1	587	575	2.1%
2 2	590	582 - 583	1.3%
2 3	660	627 - 635	4.3%

4.2.7 Conclusion

The effects of uniform perforation patterns on the natural frequencies of cylindrical shells has been assessed by FE and experimental analyses. The following general observations can be made.

- As the number of holes increases the natural frequencies approach a steady value.
- In general, the reduction in stiffness is a stronger influence on frequency change than the reduction in mass, i.e., the addition of holes reduces the unperforated natural frequencies.
- Increasing the void fraction from 20% to 40% reduces the natural frequencies.
- For a large number of holes, the ordering of the natural frequencies remains unchanged from the unperforated ordering.
- For a large number of holes, the mode shapes are similar to the unperforated mode shapes.

4.2.8 Ongoing Investigations

Thus far the finite element models have all been developed for a modal analysis solution within the commercial code ANSYS. A transient solution type is being benchmarked in order to simulate the dynamic response to blast waves and identify the regions under the highest stress.

4.3 Spherical Shells

4.3.1 Introduction

Spherical shells have also been proposed to be used as containment vessels for inertial confinement fusion, for example in National Ignition Facility (NIF). Determining the structural response (i.e., the location of maximum displacement and stresses) of spherical shells with perforations subjected to repetitive thermal and mechanical loads released from the implosion is necessary for the successful design of an ICF reactor. Analytical solutions for the axisymmetric natural frequencies for a homogenous, continuous sphere can be found in the literature [16, 17]. These analytical solutions can be used to benchmark more complicated finite element models, such as spherical shells with perforations for laser beams and target injection.

4.3.2 Finite Element Modeling and Verification

An axisymmetric finite element model of a spherical shell has been created using the commercially available program ANSYS. This model includes membrane and bending stress, and boundary conditions can be specified to correspond to realistic support conditions. The analytical equation for the torsionless natural frequency based on bending theory can be found in [16] and the torsional natural frequency equation based only on membrane theory can be found in [17]. For both of these solutions, it is necessary to idealize the problem such that no support forces (i.e., boundary conditions) are applied to the spherical shell. Table 4.4 compares the analytical and finite element torsionless natural frequencies and Table 4.5 compares the torsional natural frequencies. The finite element model is in excellent agreement with the analytical solutions. Mode 1 of Table 4.4 is the "breathing" mode of the sphere. This is the mode that will be predominately excited from a uniform blast wave emanating from the center of the sphere.

Table 4.4. Natural frequencies of the first three modes of torsionless vibration dominated by in-plane motion for the following parameters: a = 1 m, h = 0.02 m, E = 216 GPa, υ = 0.3, ρ = 7800 kg/m^3.

Mode Number	Analytical Solution [Hz] (Bending Theory)	FEM Solution [Hz] (Axisymmetric Model, 201 Nodes)
1	1415.7	1415.7
2	1733.9	1733.8
3	2389.9	2389.8

Table 4.5. Natural frequencies of the first three torsional modes for the following parameters: a = 1 m, h = 0.02 m, E = 216 GPa, υ = 0.3, ρ = 7800 kg/m^3.

Mode Number	Analytical Solution [Hz] (Membrane Theory)	FEM Solution [Hz] (Axisymmetric Model, 201 Nodes)
1	1038.7	1038.9
2	1642.4	1642.7
3	2203.5	2204.1

In addition, an analytical solution based on membrane theory and a numerical implementation of the solution has been completed to simulate the dynamic response of an axisymmetric spherical shell to uniform sequential impulses. It is assumed that the shell is thin and will be uniformly excited by the blast loading. A single mode solution using the "breathing" mode has been used for this solution. The intent here is to use this numerical solution to benchmark the individual finite element models as they are developed for the transient and steady-state simulations. A typical example is presented in the following section.

4.3.3 NIF Minichamber

The NIF minichamber is a concept proposed by Professor Per Peterson at the University of California at Berkeley for basic diagnostic testing. The minichamber is a smaller chamber that is to be inserted inside the main NIF target chamber through the hollow cylinder used for the pedestal support. With this design constraint, the proposed minichamber would be approximately one tenth the size of the main chamber. The target would be contained inside the minichamber and both would be cryogenically cooled.

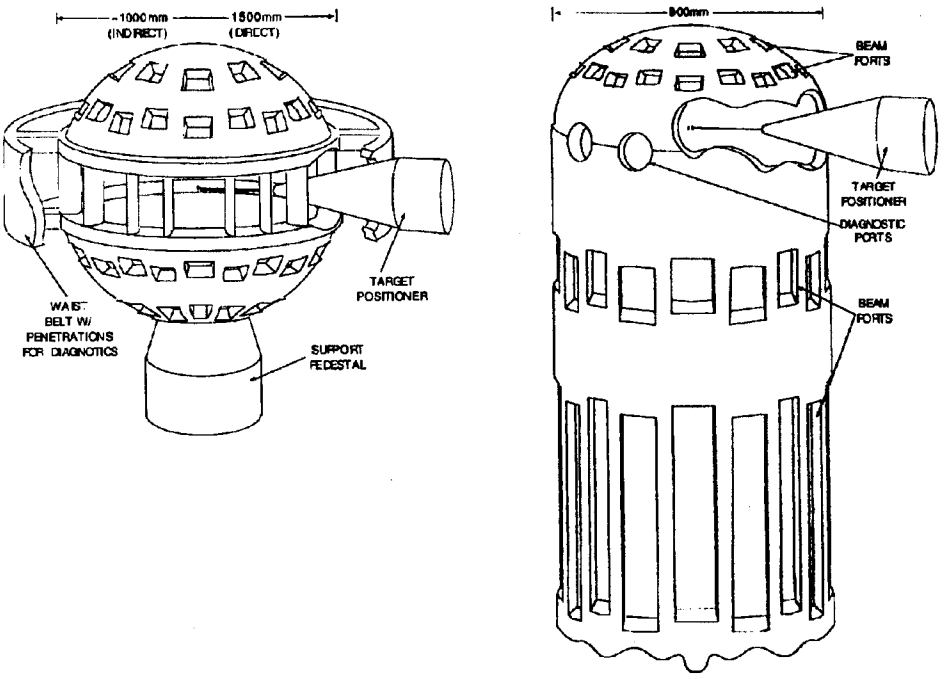

Fig. 4.10. Spherical and cylindrical NIF mini-chambers [3].

Possible design options for the configuration of the minichamber included a spherical chamber or a cylindrical chamber with hemispherical end caps; see Fig. 4.10. It would be constructed out of aluminum with perforations to allow the laser beams to reach the target. To investigate the feasibility of the minichamber withstanding a typical blast loading, a scoping

study was performed. For the case presented here, the chamber was assumed to be spherical in shape with no perforations (a worst case scenario). In addition, no supporting structure or constraints were placed on the sphere. The outer radius was assumed to be 55 cm and the thickness was set at 5 cm (but could be varied as needed). A finite element model was generated to simulate the response of the shell structure to an internal, time-dependent pressure load. Analytical solutions were then used to benchmark and verify the dynamic results.

Table 4.6 lists the material properties of 6061 aluminum at room temperature. However, at a temperature of -240 °C, the yield strength increases from 270 MPa to 340 MPa and the ultimate strength (or tensile strength) increases from 310 MPa to 480 MPa. Therefore, for this scoping study, the more conservative properties were used in the analyses, i.e., those at room temperature. In addition, a structural damping level of 1.0 % was set for all calculations.

Table 4.6. Material properties of 6061 aluminum at room temperature.

Yield Strength	270 MPa
Ultimate Strength	310 MPa
Modulus of Elasticity	70 GPa
Density	2700 kg/m^3
Poisson's Ratio	0.33
Structural Damping	1%

4.3.4 NIF Minichamber - Hydrodynamics

Figure 4.11 shows the time-dependent pressure load as computed by the scientists at the University of California at Berkeley using the code TSUNAMI. It is assumed that the pressure is applied uniformly on the inside of the sphere, normal to the surface. The maximum pressure of 2.66 MPa occurs at 4.3 μs, then at 100 μs the pressure decays away until it reaches zero at 1 ms. For convenience, a linear function was assumed for the decay beyond 100 μs.

4.3.5 NIF Minichamber - Mechanical Response

The response of the minichamber to the internal pressure load was calculated numerically. An axisymmetric finite element model of a sphere was constructed employing elastic shell elements that included both bending and membrane stiffness. The time-dependent pressure loading was applied uniformly and normal to the inside surface of the sphere. A transient solution was used to calculate displacements and stresses as a function of time due to the time-dependent pressure loading.

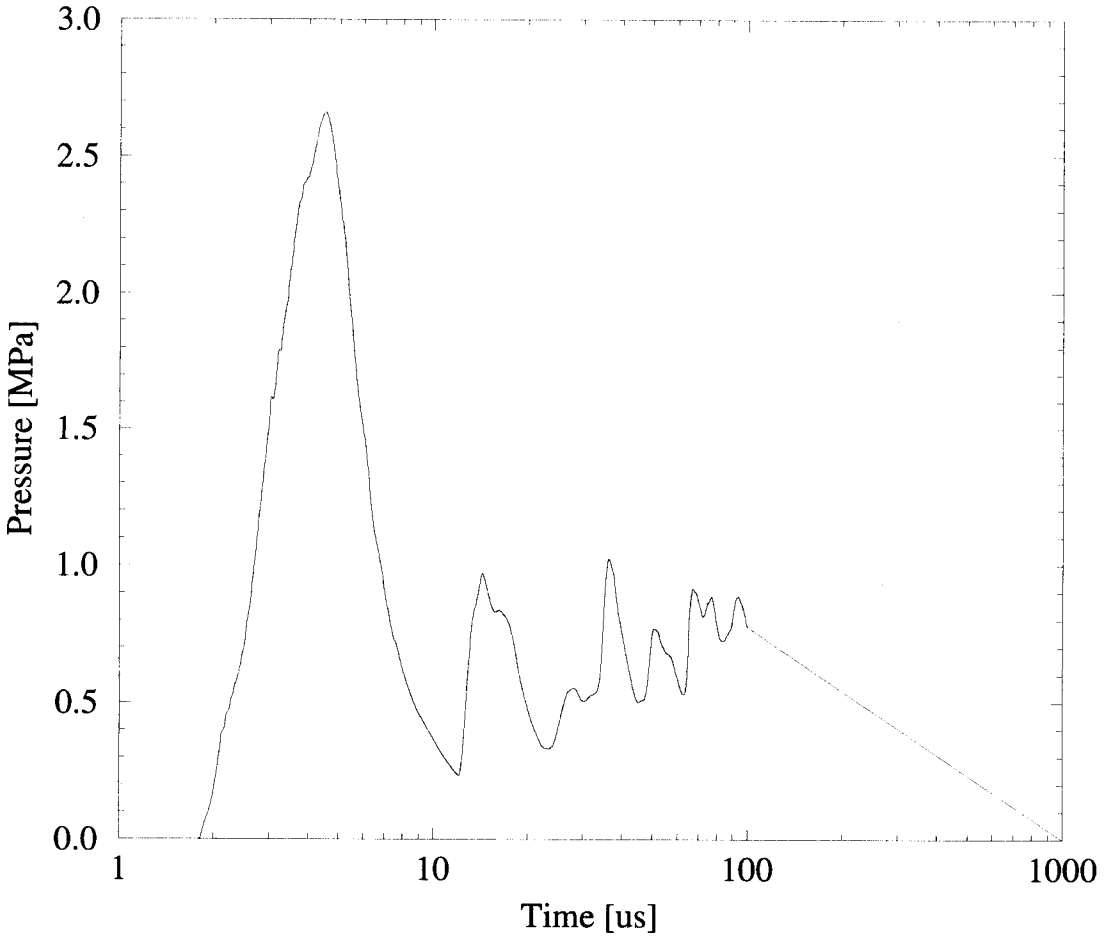

Fig. 4.11. Internal pressure load on the NIF minichamber (Prof. P. Peterson).

An analytical solution for the response of the minichamber to an impulse loading was also examined. Soedel [16] presents the axisymmetric equation of motion of a thin, spherical shell with free boundary conditions. The theoretical solution also neglects bending stiffness (i.e., provides only a membrane approximation). Using the convolution integral, the impulse solution with the pressure load was numerically integrated to find the response of the shell. Figure 4.12 shows the analytical results for the radial displacement of the shell during and after the impulsive pressure loading. For a thickness of 5 cm, a maximum radial displacement of 0.0385 mm occurs at 0.19 ms. The figure shows the shell "ringing" or vibrating for 20 to 30 ms after the end of the pressure loading. The duration of the "ringing" is directly affected by the amount of structural damping in the system.

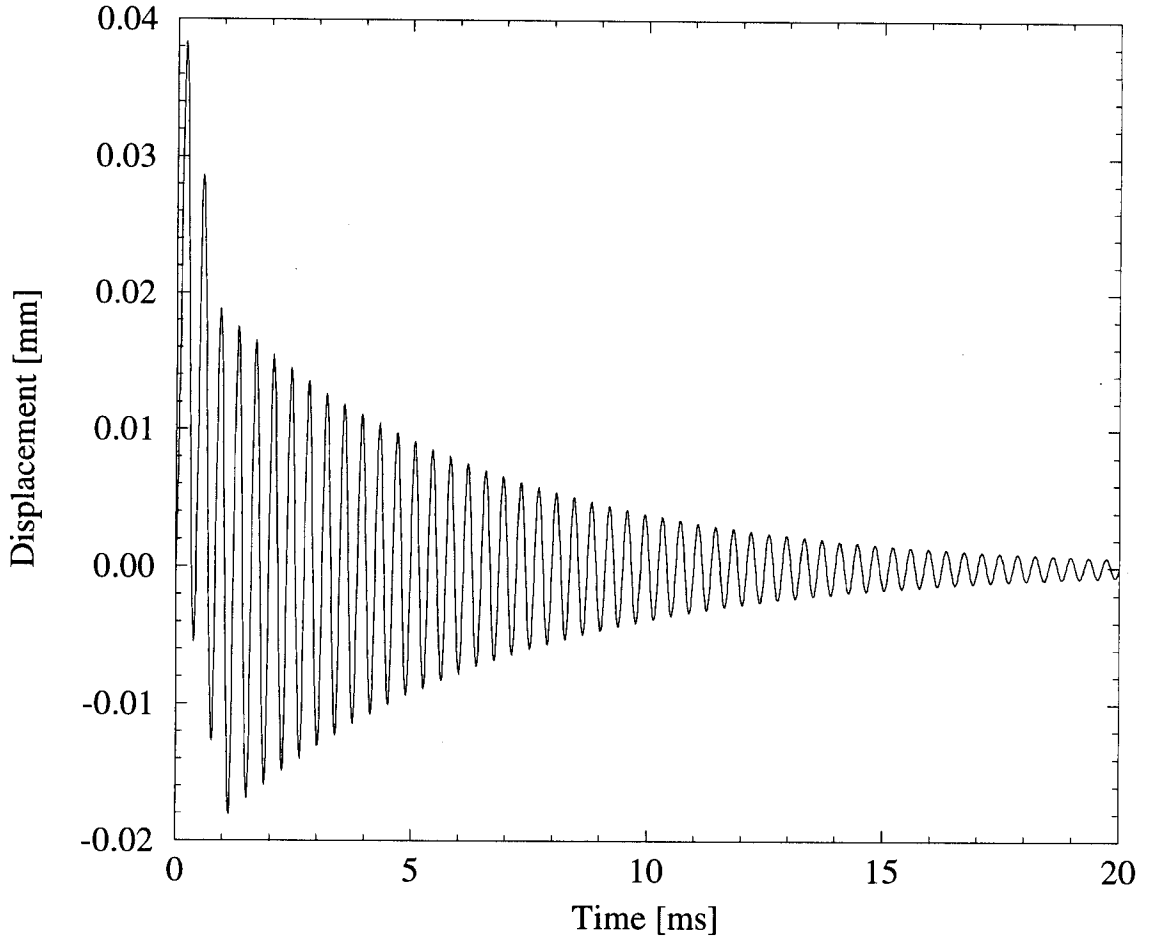

Fig. 4.12. Radial displacement of the minichamber as a function of time.

Figure 4.13 compares the analytical and finite element solutions for the in-plane or membrane stress in the shell during the first 0.20 ms of the pressure loading. A maximum stress of 7.7 MPa occurs at 0.19 ms (the same time as the maximum radial displacement). The remainder of stress history will follow the same characteristic curve as the displacements. In addition, the finite element model is capable of calculating the stress at both the inner and outer surfaces of the shell, which can be seen in Fig. 4.13. Note that as the impulse load is first applied, the shell can not respond in the same time frame. In fact, on the inner surface of the shell a compressive stress develops because the shell itself is effectively behaving as a constraint.

The maximum stress in the spherical shell (7.7 MPa) is well below the yield strength of 6061 aluminum (270 MPa at room temperature). In the above analysis, none of the typical stress risers, such as perforations in the shell and boundary conditions, were modeled. In an actual structure the maximum stress could be as much as an order of magnitude larger. Also, the

possibility of brittle fracture or fatigue fracture at the low operating temperature has not yet been addressed.

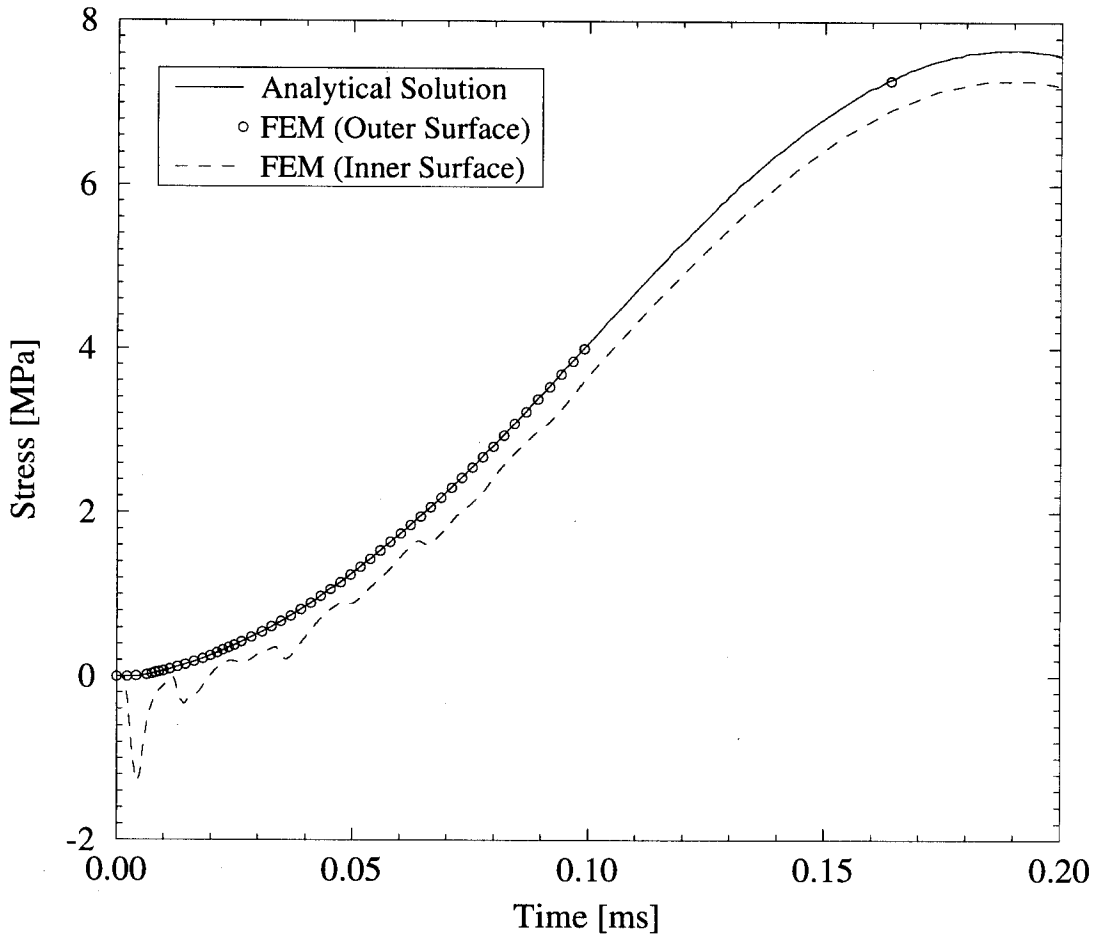

Fig. 4.13. In-plane stress of the minichamber as a function of time.

4.4 Hemispherical Shells

4.4.1 Introduction

The primary goal of this research is to aid in the design of hemispherical endcaps for use in inertial confinement fusion reactor target chambers. Any shell structure used in a target chamber may require various holes, or perforation patterns, for diagnostic equipment, target insertion, and beam lines. To properly design a target chamber, the natural frequencies of the structure must be known to prevent catastrophic failures due to resonant conditions and as a basis for any fatigue analysis.

4.4.2 Problem Formulation

A spherical coordinate system, (r, θ, ϕ), was used throughout this analysis. It is shown in Fig. 4.14 with the (x, y, z) Cartesian coordinate system for reference. In addition, an element of the shell is shown with all associated displacements. The displacement normal to the shell is represented by w. Tangential circumferential displacement and tangential meridional displacements are represented by v and u, respectively.

All shells studied in this research are considered "thin," i.e., $h/R << 1$. In the study of thin shells, the outer surfaces of the structure are compressed to the middle surface, and a thickness is assigned to the structure. Two general perforated hemispherical shell structures were studied in this analysis. The first case studied was a hemispherical shell with a hole at the apex. This configuration is of primary importance in the design of fusion target chambers, e.g., the apex hole is required for target injection and also maintenance. A detailed drawing of this configuration is shown in Fig. 4.15 with all associated dimensions and variables. Obviously, for hemispherical shells, the half-angle, ϕ_0, was maintained at 90°. For each thickness to shell radius ratio, h/R, the apex hole radius to shell radius ratio, a/R, was evaluated for a wide range of values.

The second hemispherical shell studied had circumferential holes in addition to the apex hole. A view of this configuration is shown in Fig. 4.16. Like the previous shell, the hemispherical shell with an apex hole and circumferential holes was tested for three h/R values. The circumferential hole radius to shell radius ratio, b/R, was varied for each h/R ratio. The radius of the apex hole, a, was held constant. As a general case, the distance of the circumferential hole axis from the apex, ϕ_b, was taken as 45° for all analyses.

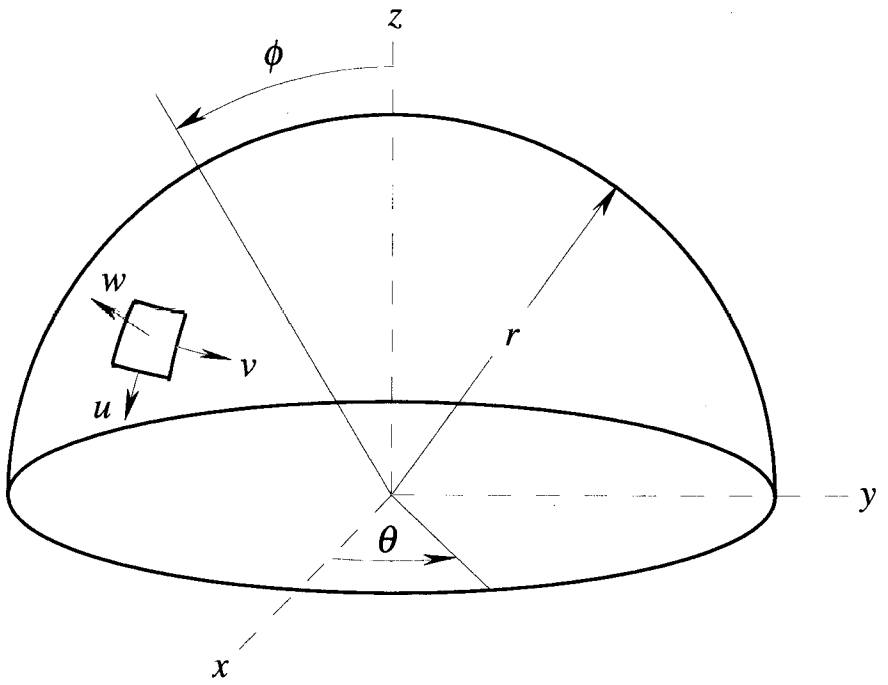

Fig. 4.14. Spherical coordinate system with shell displacement components.

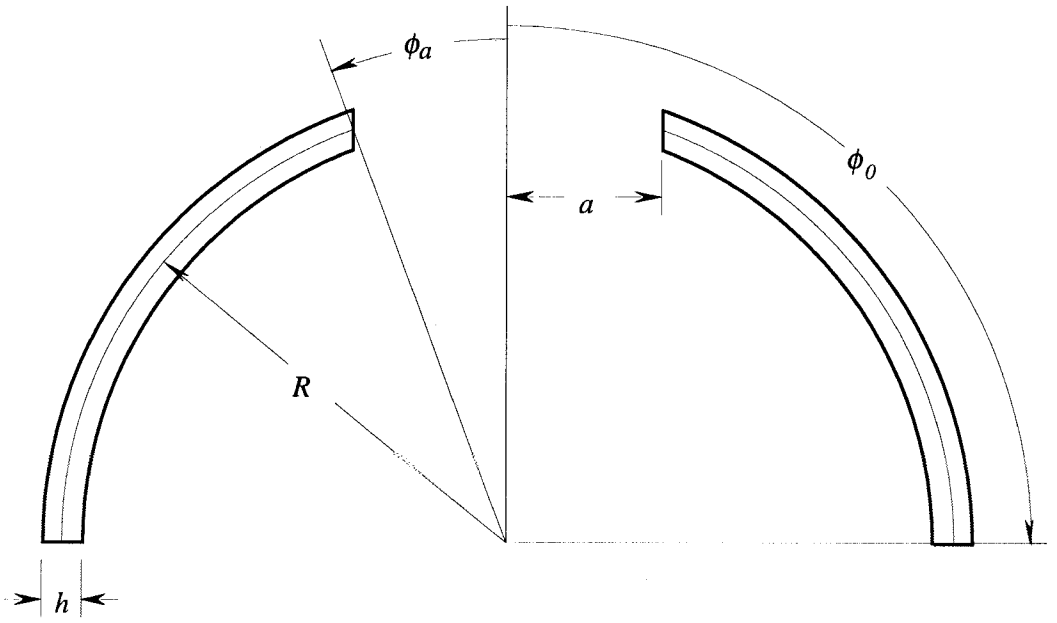

Fig. 4.15. Geometry definitions of a hemispherical shell with an apex hole.

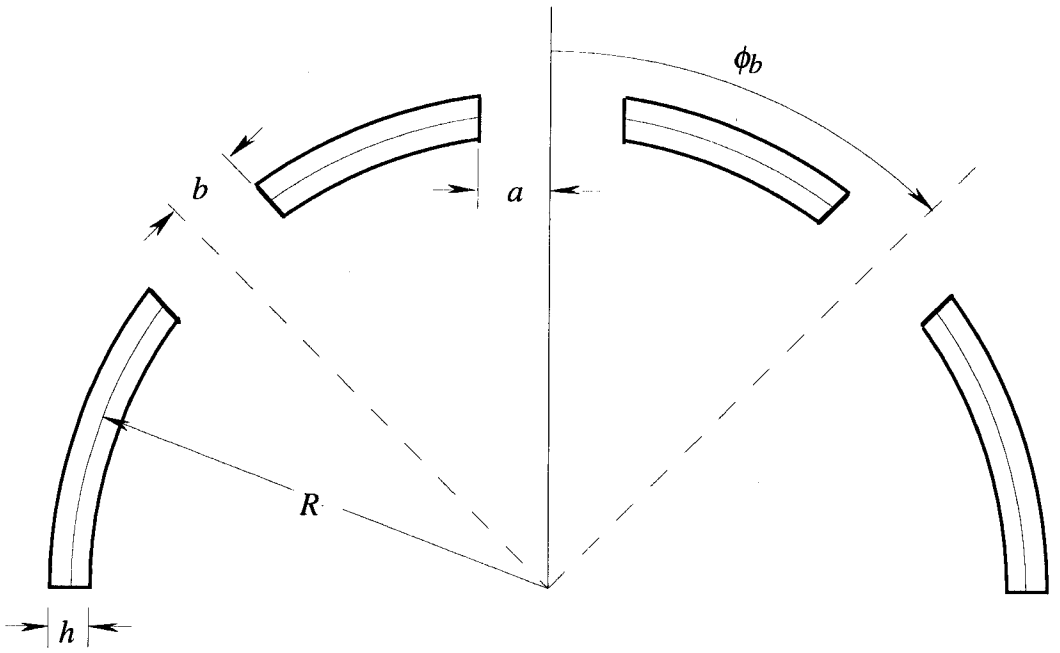

Fig. 4.16. Geometry of a hemispherical shell with an apex hole and circumferential holes.

All numerical frequency results in this study will be presented in terms of the non-dimensional frequency parameter, Ω, given by

$$\Omega = f 2\pi R \sqrt{\frac{\rho\left(1-\upsilon^2\right)}{E}}$$

where f is the frequency, ρ is the mass density, υ is Poisson's ratio, and E is the modulus of elasticity.

4.4.3 Unperforated Hemispherical Shells

A quarter symmetry finite element model of a hemispherical shell was created using 8-noded, quadrilateral shell elements (see Fig. 4.17). The surface geometry was created using Pro/ENGINEER and subsequently meshed with PATRAN; the model was then solved using ANSYS. By using quarter symmetry, greater mesh refinement could be achieved, however, this type of model could only be used to find the axisymmetric modes of the hemispherical shell. A full model is required to study all mode shapes.

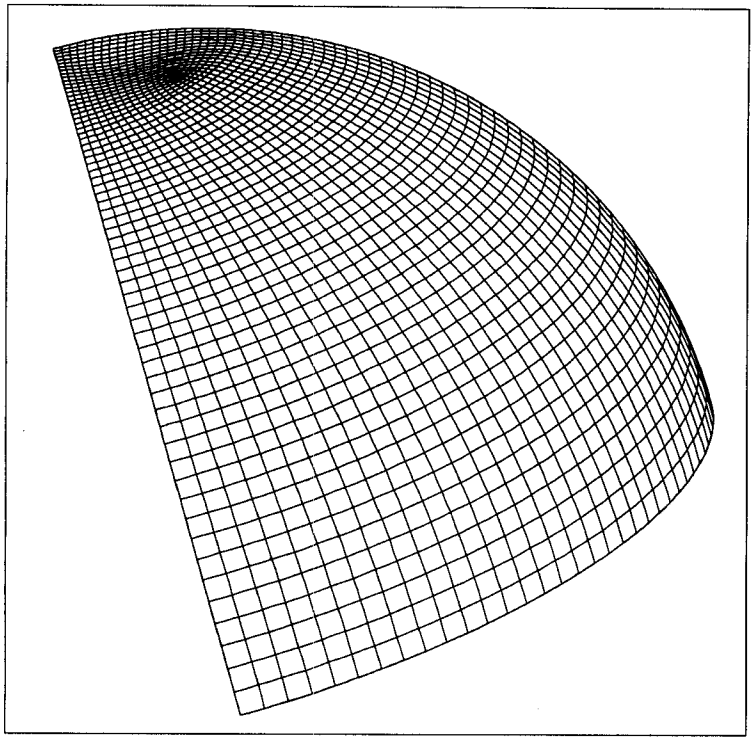

Fig. 4.17. Quarter symmetry finite element model of a hemispherical cap.

Solutions for the dynamic response of a clamped hemispherical shell without perforations have been previously documented. Eikrem and Doige [18] found the first 23 axisymmetric modes using both analytical and experimental methods. The asymmetric mode shapes were studied by Singh and Mirza [19] using finite elements. These previous results were used to verify and benchmark the finite element modeling techniques that were used to investigate perforated hemispherical shells.

Eikrem and Doige studied a 6.0 in. radius steel hemispherical shell with clamped edges, utilizing both experimental and analytical methods. The experimental shell had a mean thickness of 0.031 in. This shell has been reproduced with a finite element model as shown in Fig. 4.17. The model was created using 5824 nodes and 1887 elastic shell elements. The frequencies of the first three axisymmetric modes are shown in Table 4.7.

Table 4.7. Natural frequencies of the first three axisymmetric modes with the following parameters: $R = 6.0$ in., $h = 0.031$ in., $E = 30\text{x}10^6$ psi, $\rho = 0.733\text{x}10^{-3}$ lb-s^2/in^4, $\upsilon = 0.3$.

Axisymmetric Mode Number	Eikrem & Doige (Analytical) (Hz)	FEM Solution (Hz)	% Difference
1	4040.85	4044.4	.09
2	5001.42	5004.46	.06
3	5216.07	5218.50	.05

Singh and Mirza used finite element methods to determine the asymmetric natural frequencies of clamped hemispherical shells. To reproduce their results, a full model of the shell was created to view all possible mode shapes. A mesh similar in structure to that in Fig. 4.17 was used, but with a less refined mesh (7521 nodes, 2480 elastic shell elements). The results are given in Table 4.8.

Table 4.8. Natural frequencies of the first eight asymmetric modes with the following parameters: R = 6.0 in., h = 0.030 in., E = 30x10^6 psi, ρ = 0. 733x10^{-3} lb-s^2/in^4, υ = 0.3.

Asymmetric Mode – M, I M = Meridonal I = circumferential	Singh & Mirza (Analytical) (Hz)	FEM Solution (Hz)	% Difference
1, 1	3034.36	3022.17	0.40
2, 1	4768.69	4761.13	0.16
1, 2	4829.44	4826.63	0.06
1, 3	5065.15	5062.26	0.06
3, 1	5141.09	5136.34	0.09
2, 2	5160.78	5158.53	0.04
1, 4	5168.10	5165.18	0.06
1, 5	5232.23	5229.36	0.05

As shown by Tables 4.7 and 4.8, the finite element model gives excellent results when compared to known dynamic responses. This finite element method can subsequently be used to identify the dynamic response of hemispherical shells with various perforation patterns.

Finite element models have been created for two perforation patterns. The first is a quarter symmetry model of a hemisphere with a hole at the apex (see Fig. 4.18). The second is a quarter symmetry model with a perforation pattern around the circumference in addition to the hole at the apex (see Fig. 4.21). It should be noted that the quarter symmetry models can be easily transformed into a full model. In addition, the models were created using only quadrilateral elements, which will yield the best results.

4.4.4 Axisymmetric Vibrations of a Hemispherical Shell with an Apex Hole

Any fusion target chamber with a hemispherical endcap will most likely have an apex hole for target insertion and maintenance. This section presents numerical results for the axisymmetric frequency of the first mode of clamped hemispherical shells with apex hole radius to shell radius ratios, a/R, varying from 0 to 0.8. Shells with thickness-to-radius ratios, h/R, of 0.005, 0.010, and 0.050 were evaluated.

Because this research had a direct application, analyses were performed to represent conditions anticipated in a fusion target chamber. When a uniform, radial, impulse load is applied to an axisymmetric shell, only the axisymmetric modes will be excited. Also, when a hemispherical shell is used as a structural component of a target chamber, the edge will most

likely be rigidly clamped. Therefore, only the axisymmetric natural frequencies of a hemispherical shell with a clamped edge were studied. Modeling using symmetry conditions can minimize computational time and allow proper mesh refinement. Quarter symmetry models were used to study the axisymmetric case of a hemispherical shell with an apex hole. An example of the mesh used is shown in Fig. 4.18. Symmetry conditions were applied to the edges at $\theta = 0°$ and $\theta = 90°$. The bottom edge at $\phi = 90°$ was rigidly clamped. A quarter symmetry model was used rather than a model created from axisymmetric elements since quarter symmetry was required to model the non-axisymmetric circumferential perforation pattern.

Figure 4.19 shows Ω vs. a/R for the first axisymmetric mode for each h/R ratio evaluated. As shown, Ω increases as a/R increases. Interestingly, the apex hole has negligible effects on the natural frequency for small radius values. The normalized mode shapes of the fundamental axisymmetric modes for a hemispherical shell with $h/R = 0.050$ with an apex hole are shown in Fig. 4.20.

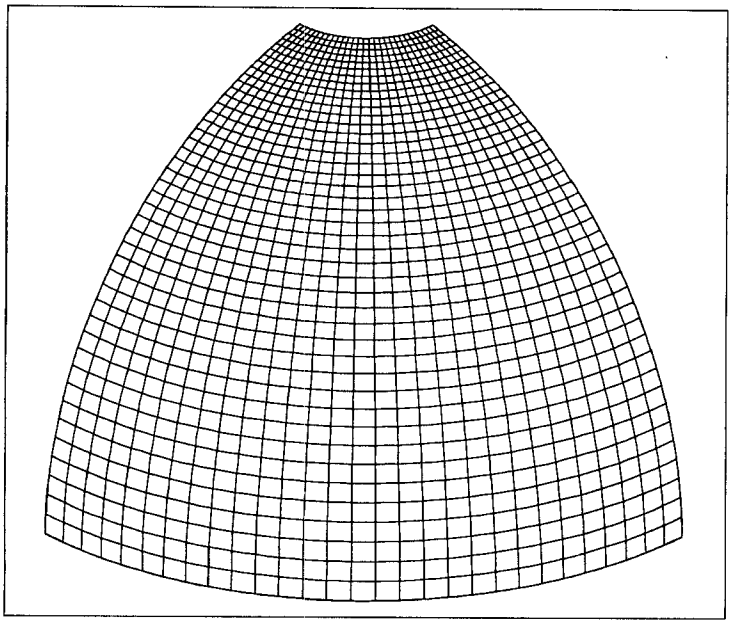

Fig. 4.18. Quarter symmetry finite element model of a hemispherical shell with an apex hole, 1247 elements.

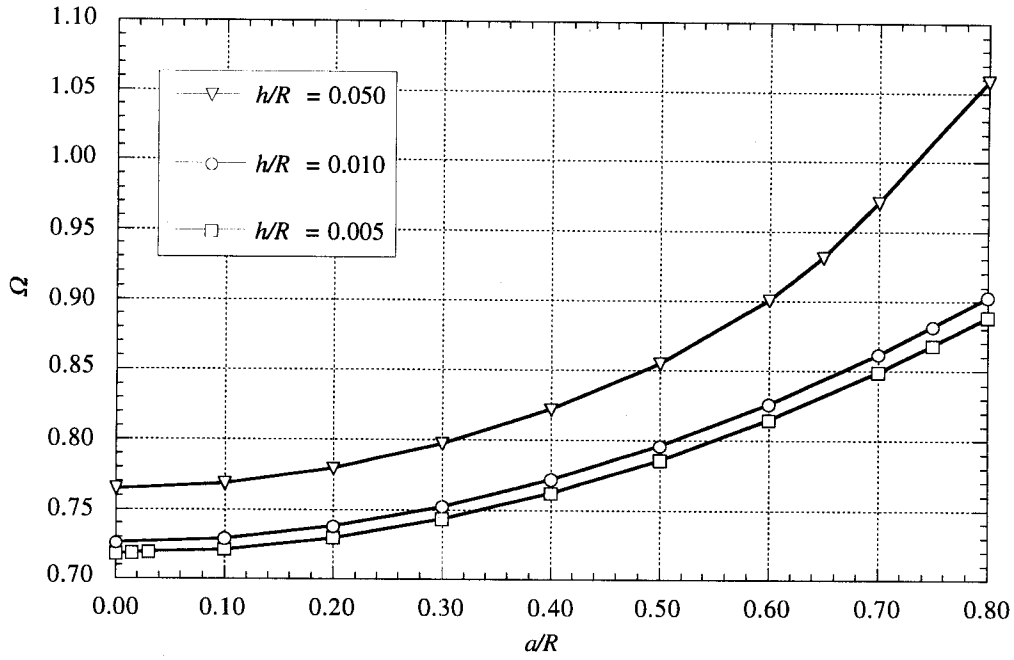

Fig. 4.19. Nondimensional frequencies of the first axisymmetric mode for three h/R ratios.

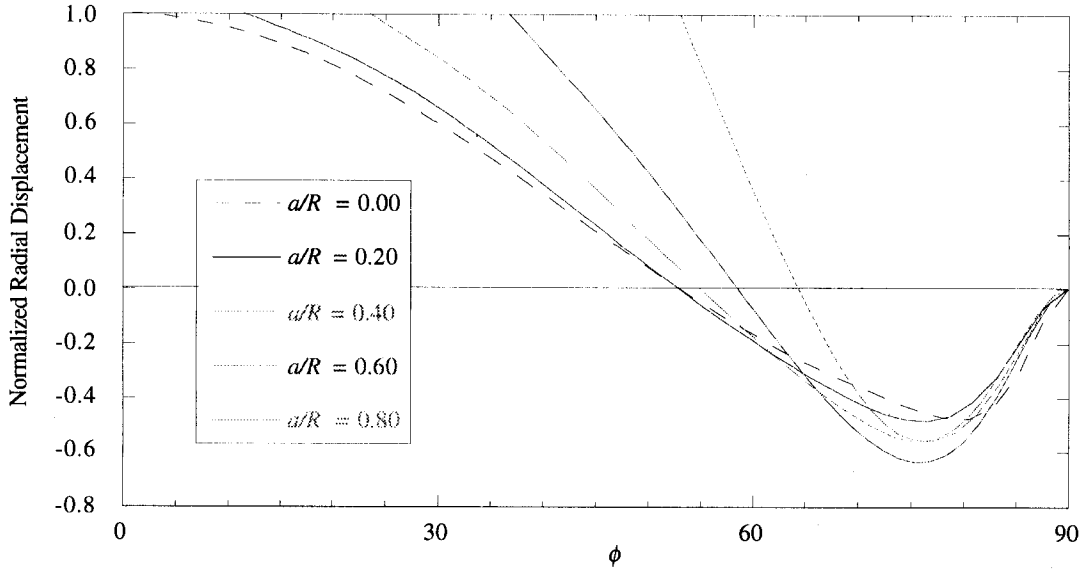

Fig. 4.20. Normalized mode shapes of the fundamental axisymmetric mode for a clamped hemispherical shell with an apex hole ($h/R = 0.050$).

4.4.5 Impulse Loading of a Hemispherical Shell with Apex and Circumferential Holes

Hemispherical shells used for fusion target chambers may have circumferential holes in addition to the apex hole. Circumferential holes are used for diagnostic equipment and laser ports. The apex hole is still needed for target insertion and maintenance. Because of the circumferential holes, the shell is no longer axisymmetric and will therefore not have axisymmetric mode shapes. This section investigates the response of a clamped edge hemispherical shell with 16 equally spaced circumferential holes in addition to an apex hole for the impulse load.

Figure 4.21 shows the quarter symmetry finite element model used for this investigation. It as 2536 nodes and 783 elements. The shell had the following parameters: R = 5.0 in., h = 0.050 in., a = 0.50 in., b = 0.25 in., $E = 30.0\times10^6$ psi, $\rho = 0.733\times10^{-3}$ lb-s^2/in^4, $\upsilon = 0.3$, $\phi_b = 45°$. The boundaries around the holes are free (not reinforced or supported).

A radial impulse pressure of 450 psi was applied for 2.0×10^{-6} seconds to the FE model shown in Fig. 4.21. The response of the shell was taken to 0.008 seconds with damping neglected. Figure 4.22 shows the displacements of a node at $\phi \approx 50°$ as a function of time. A Fourier transform of the data is shown in Fig. 4.23. A modal analysis was performed to identify the frequencies of the quasi-axisymmetric modes. The resulting nondimensional frequencies are shown in Table 4.9. The frequencies in Table 4.9 can be compared with the spikes in Fig. 4.23.

Table 4.9. Non-dimensional quasi-axisymmetric natural frequencies for clamped edge hemispherical shell with the following parameters: a/R = 0.10, b/R = 0.05, h/R = 0.01.

Quasi - Axisymmetric Mode	Ω
1	0.7073
2	0.8306
3	0.9341
4	0.9583
5	1.0149
6	1.0800
7	1.1896
8	1.3179
9	1.4804
10	1.5658
11	1.7236
12	1.9478
13	2.2616

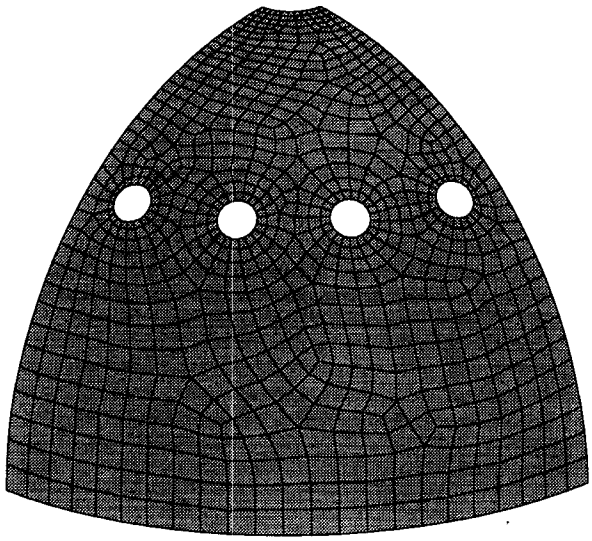

Fig. 4.21. Quarter symmetry finite element model of a hemispherical shell with 16 circumferential holes and an apex hole. The geometry has the following parameters: $a/R = 0.10$, $b/R = 0.05$, $\phi_b = 45°$, 783 elements.

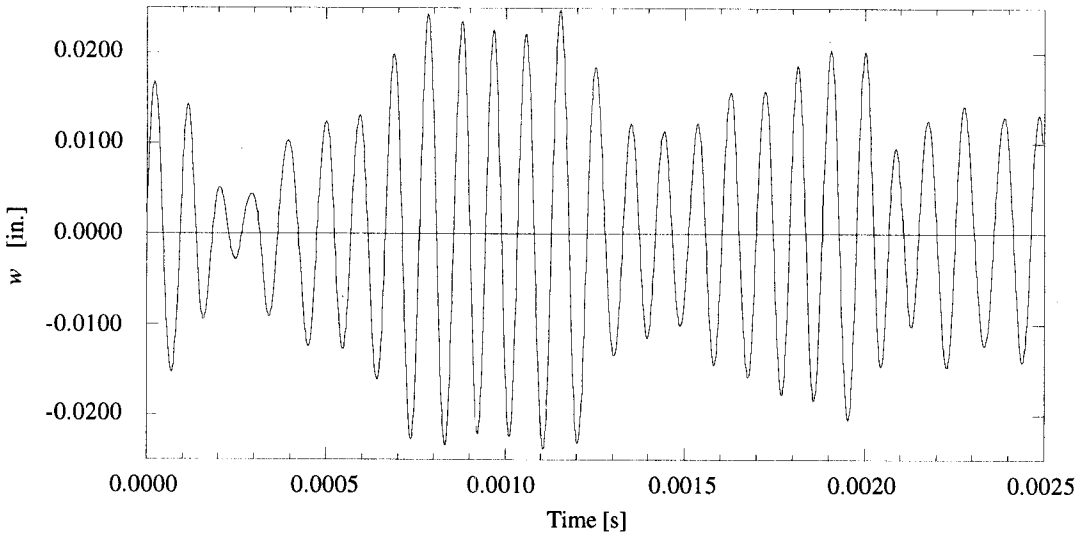

Fig. 4.22. Radial displacement of a FE node at $\phi \approx 50°$ as a function of time after an impulse load of 450 psi for 2.0×10^{-6}s.

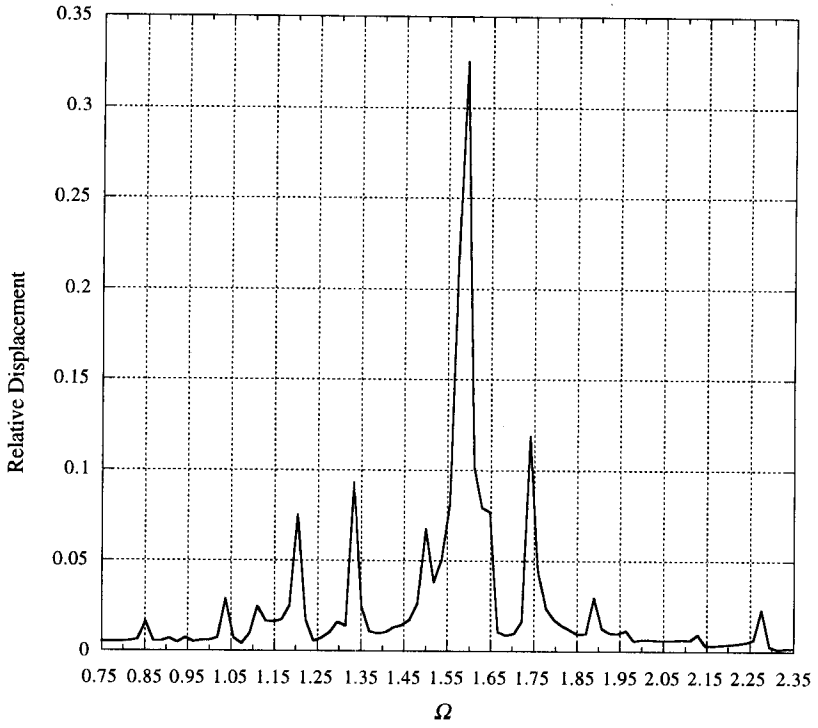

Fig. 4.23. Fourier transform of the data shown in Fig. 4.22.

4.5 Perforated Plates

4.5.1 Introduction

Mechanical, aerospace, and civil engineers all design structures and structural components with plates and shells. Fortunately, the design and analysis of solid plates and shells is well established. Structural designs often deliberately incorporate cutouts or perforations to reduce materials, lighten loads, allow for ventilation, or provide functional openings. Accounting for these perforations in the analysis can be an integral part of determining the correct deflections, stresses, modal frequencies, and mode shapes of a particular structure. In static cases where a plate is perforated with a number of circular holes, assembled in a pattern, the structural changes have traditionally been accounted for by using effective material constants. Usually, the perforated plate is equivalent to a uniform solid plate of the same thickness but having new modulus and Poisson ratio values established by an equal global stiffness criterion.

Industry has numerous engineering applications involving perforated plates. For example the heat exchanger industry, focusing on tube sheet behavior, has supported perforated plate research for over fifty years. As a result, there is an abundance of numerical and experimental work on the static behavior of perforated plates. This data has been tabulated and plotted in design curves and can be found in codes such as the French pressure vessel code CODAP [20] and ASME Boiler and Pressure Vessel Code [21]. Osweiller [22] and Slot [23] have written excellent summaries on the history of perforated plate research. However, there are no known design curves for dynamic behavior of perforated plates.

This study is intended to take the next logical step in understanding the behavior of perforated structures, i.e., characterizing the dynamic response of perforated plates. The study focuses on thin square plates with completely clamped boundary conditions. More specifically the plates are perforated with a large number of uniform circular holes arranged into a square or triangular pattern.

A natural frequency and associated mode shape characterize the dynamic behavior of a perforated plate. Finite element methods and experimental methods were utilized to predict and define this behavior. The resulting data was correlated and converted into effective elastic constants that could be presented as design curves. Classical solid plate theory was used for this conversion from frequency to effective dynamic stiffness.

4.5.2. Perforation Terminology

Two perforation patterns, square and triangular, are most common in industry (see Figs. 4.24 and 4.25). Both patterns use a common parameter, μ, referred to as the ligament efficiency, i.e.,

$$\mu = \frac{h}{P} = \left[1 - \frac{2R}{P}\right]$$

Ligament efficiency is the ratio of ligament width, h, to the perforation center-to-center distance, defined in Figs. 4.24 and 4.25 as the pitch, P. The most fundamental cells for the square and triangular patterns are square and hexagonal, respectively. These basic shapes, containing a single hole, are used in conjunction with solid modeling and FE meshing methods to generate a uniform perforation pattern.

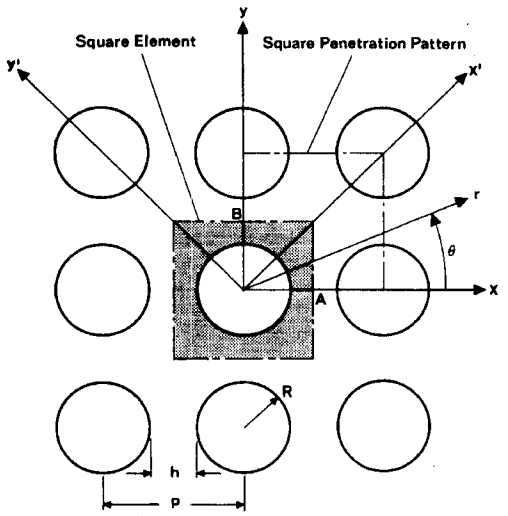

Fig. 4.24. Geometry for square perforation pattern [23].

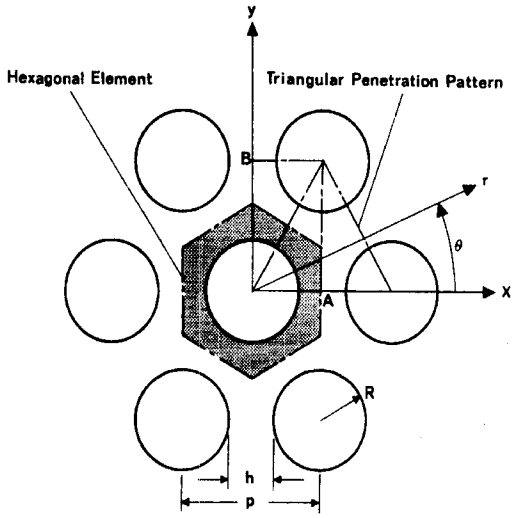

Fig. 4.25. Geometry for triangular perforation pattern [23].

4.5.3 Classical Plate Theory

The characteristic equation for thin clamped square plates can be described by the following [24]:

$$\omega_n = \frac{\lambda_n}{b^2}\sqrt{\frac{D}{\bar{m}}} \quad (n = 1,2,3,\ldots)$$

where λ_n is a frequency constant, listed in Table 4.10, $\bar{m}$ is the mass per unit area, b is the length of the square plate and D is the flexural rigidity of the plate. The mass per unit area is defined as follows:

$$\bar{m} = \frac{\gamma t}{g} = \rho t$$

where γ is the specific weight of the material, g is the gravitational acceleration, ρ is the mass density, and t is the plate thickness.

Table 4.10. Frequency constants for clamped square plates [24].

mode number, n	λ_n
1	35.97
2	73.36
3	108.13
4	131.51
5	164.82
6	210.38
7	219.69

4.5.4 FE Modeling and Benchmarking

Benchmarking FE models with published design curves, comprised of static effective constants, is simplified by limiting the number of plate variables. For example, Kaap's work [5] focused on thin, homogeneous square plates loaded in pure bending. Consequently, only the design curves on perforated plates subjected to pure bending were used for benchmarking the FE models.

Solid plate models were constructed within the FE software package ANSYS. The material properties and geometry used to generate each model are defined in Table 4.11. A number of different models with perforations were generated from the basic model. Some of the parameters that were individually varied were Poisson's ratio, hole size, material density, and the perforation pattern. Varying the perforation hole size indirectly varied ligament efficiency. It should be noted that the pitch, P, is held constant at a value of 2.0.

Table 4.11. Properties for a solid plate model.

Material	6061-T6 Aluminum
Poisson's ratio, ν	0.32
Young's modulus, E	10.0×10^6 lb/in^2
Density, ρ	2.536×10^{-4} lb-s^2/in^4
Thickness, t	0.125 in
Plate width and length, l	10 in

Meshing the perforated plate models was also done within ANSYS using SHELL63, a four-node elastic shell element. This element was chosen because it has been successfully benchmarked against solid plate theory and has excellent convergence for perforated plate models. Model generation started by constructing a controlled mesh around a single hole using the most basic repeatable shape. This meshed area was then replicated to generate a full model.

4.5.5 FE Analysis and Results

Dynamic effective elastic constants are the independent variables in the frequency response equation. The primary dependent variable is the natural frequency of the perforated plate, which is taken from the FE analysis. Effective stiffness values, for example, are determined from backing out stiffness values from a governing equation where the all the parameters other than stiffness are known. Known parameters include the overall dimensions of the plate, 10 in. $\times$ 10 in. $\times$ 0.125 in.

Finite element plate models were generated with either square or triangular perforation patterns and variable ligament efficiencies. Using clamped boundary conditions, each model was analyzed and the modal frequencies computed. The resulting stiffness values from the first seven modes of vibration were plotted for a Poisson's ratio of 0.32 (see Figs. 4.26 and 4.27). For comparison purposes, the static effective material constants are also shown on the plots. In addition to generating modal frequencies, mode shapes were generated for the first five modes of vibration (see Figs. 4.28 and 4.29). The shapes are only intended to supplement the stiffness and therefore do not cover all seven modes.

The FE models were also used to conduct parametric studies on the effective stiffness values. The studies focused on the effects of Poisson's ratio, plate thickness, material density, and number of perforations. To simplify the study only mode 1 was considered. Results showed that effective stiffness is not a function of plate thickness as long as dimensions are within the thin plate regime (see Table 4.12). A second study showed that effective stiffness is sensitive to Poisson's ratio (see Figs. 4.30 and 4.31). Further study showed that the number of holes used to develop the data shown in Figs. 4.26 and 4.27 was a good approximation to an infinitely perforated plate (see Fig. 4.32).

Finally, parametric studies showed that effective stiffness is not a function of material density.

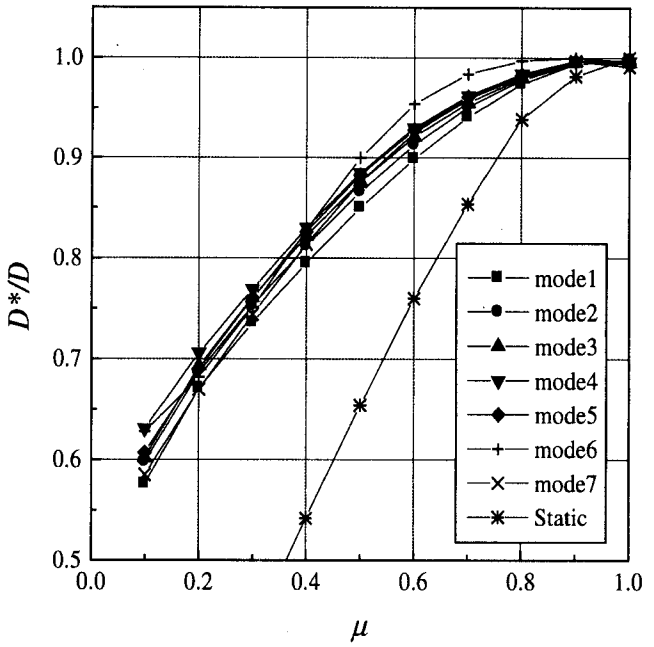

Fig. 4.26. Effective stiffness for square clamped plate with a square perforation pattern ($\nu = 0.32$).

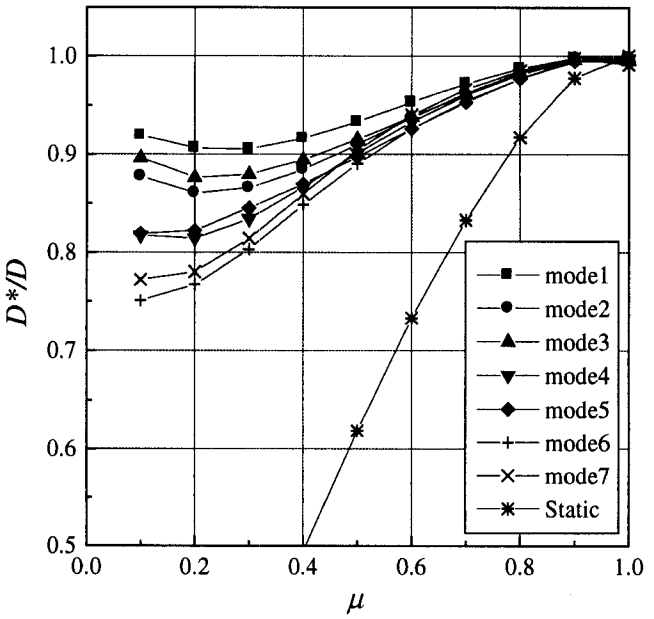

Fig. 4.27. Effective stiffness for square clamped plate with a triangular perforation pattern ($\nu = 0.32$).

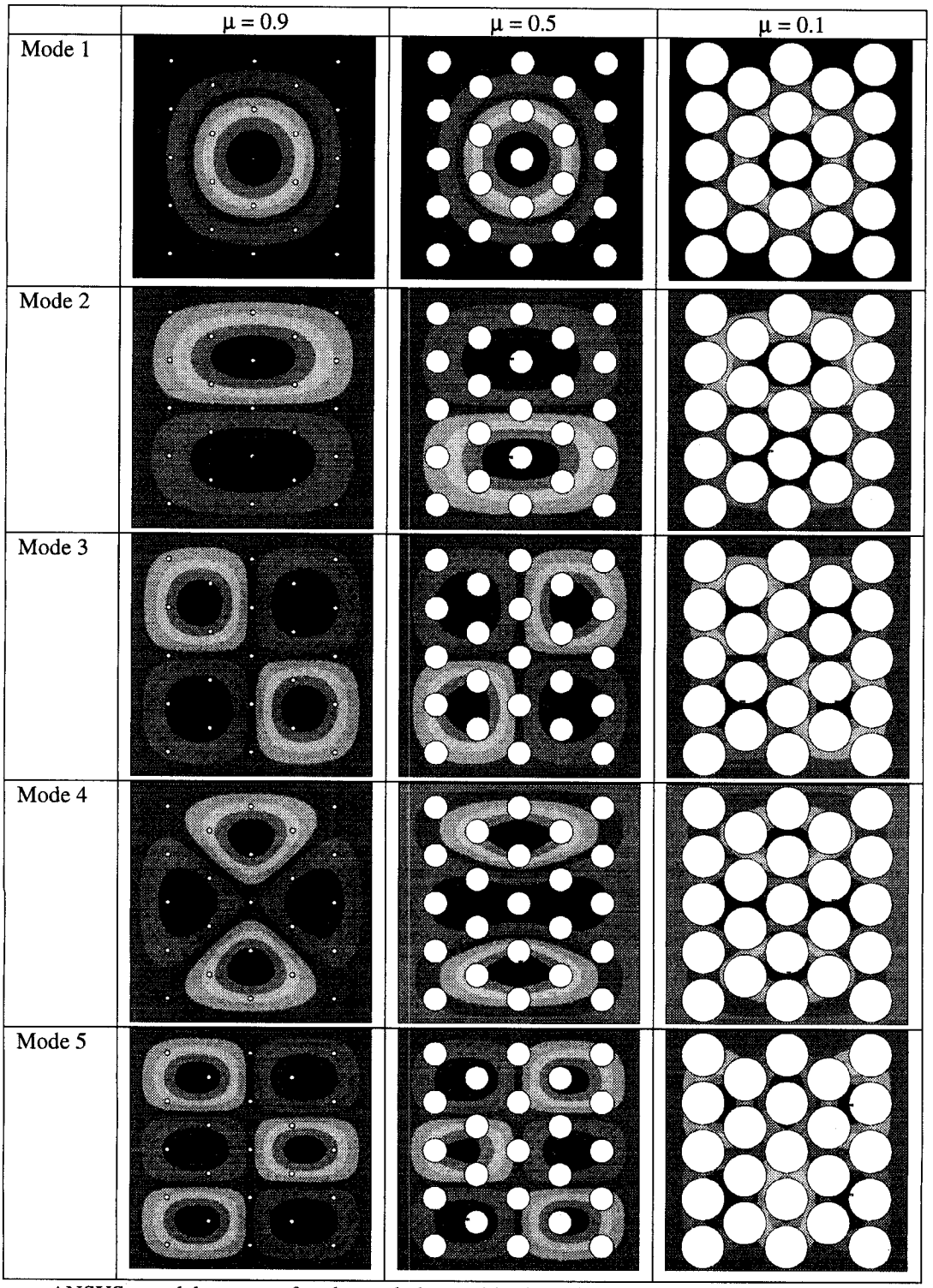

Fig. 4.28. ANSYS modal contours for clamped plates with triangular perforation patterns (P = 2.0, ν = 0.32).

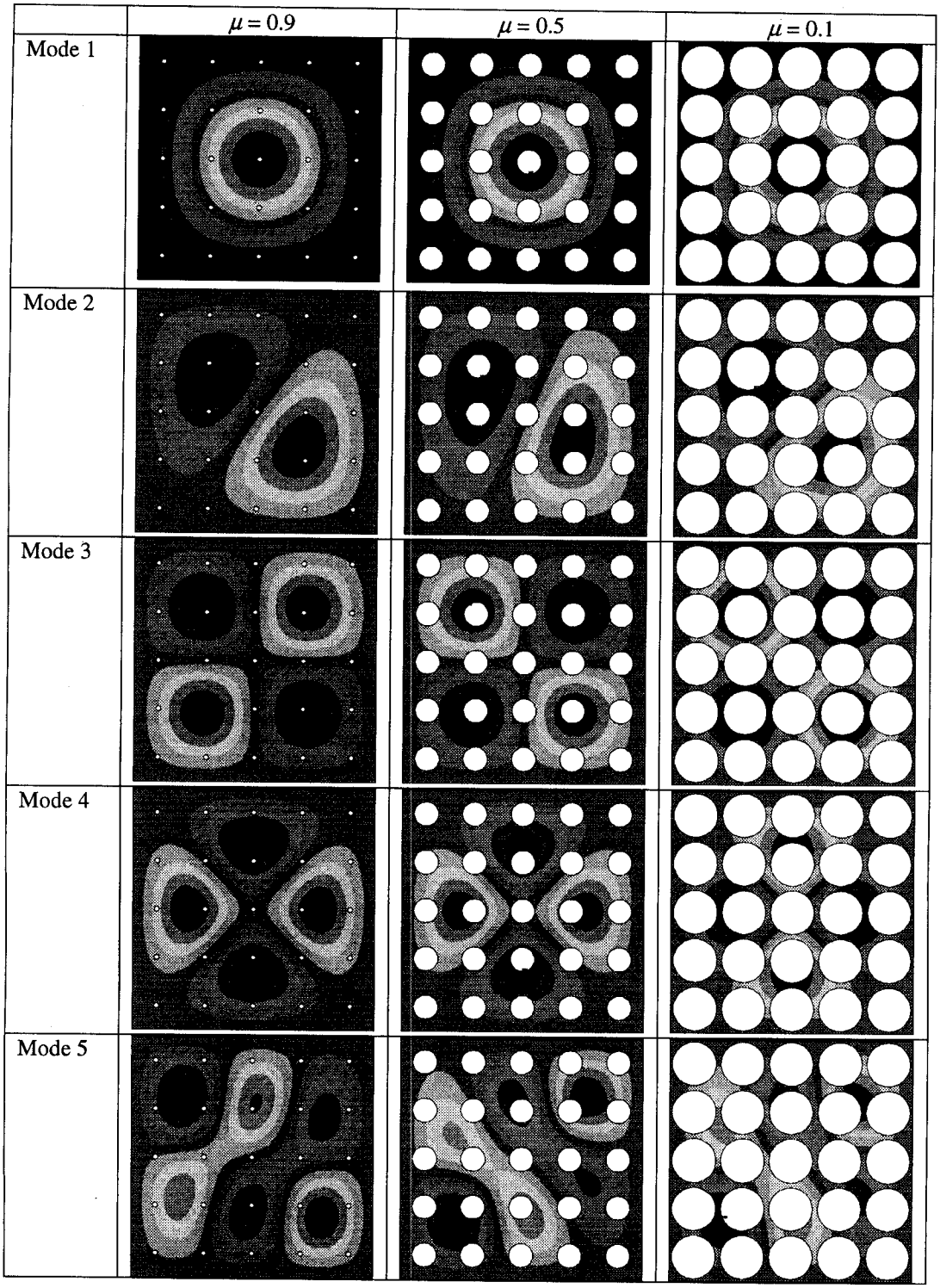

Fig. 4.29. ANSYS modal contours for clamped plates with square perforation patterns ($P = 2.0$, $\upsilon = 0.32$).

Table 4.12. Sensitivity of effective stiffnesses for a square clamped plate with a square perforation pattern, based upon fundamental mode ($\nu = 0.32$, $\mu = 0.7$).

t (in)	t/P	t/l	f (Hz)	D^*/D
0.0625	0.0312	0.00625	114.88	0.926
0.125	0.625	0.0125	229.77	0.926
0.25	0.125	0.025	459.53	0.926
0.5	0.25	0.05	919.06	0.926

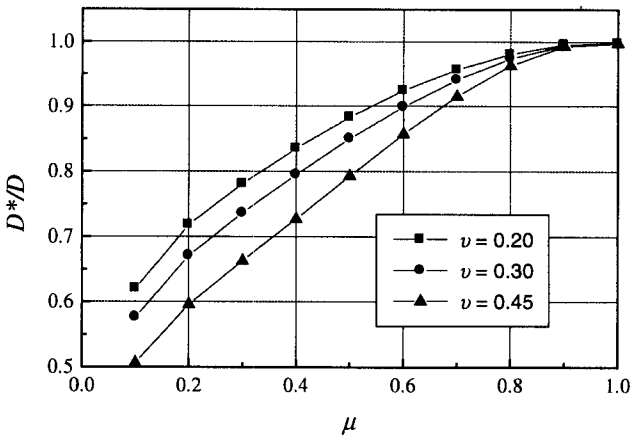

Fig. 4.30. Effective stiffnesses based upon the fundamental frequencies for square clamped plates with square perforation patterns.

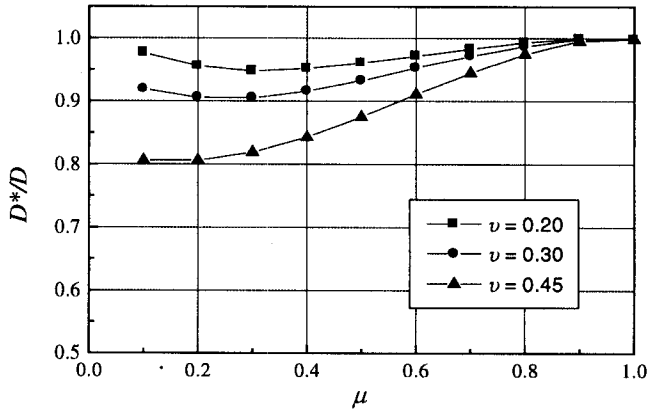

Fig. 4.31. Effective stiffnesses based upon the fundamental frequencies for square clamped plates with triangular perforation patterns.

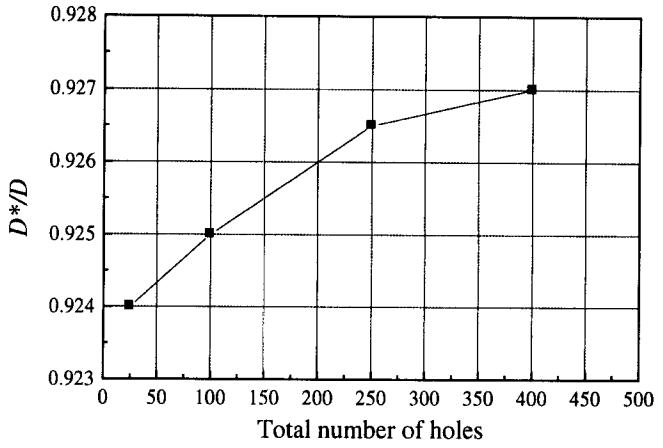

Fig. 4.32. Sensitivity of effective stiffness for fundamental mode to number of holes for square clamped plate with a square perforation pattern ($\nu = 0.32$, $\mu = 0.70$).

4.5.6 Experimental Work

Section 4.5.5 describes the use of FE models to determine the dynamic effective stiffness of completely clamped thin plates perforated with square or triangular penetration patterns. The effective stiffness values were generated using, in addition to other constant parameters, the frequency data taken from the FE modal analysis. The results differ from previously developed effective material constants, presumably, because FE results are based on a dynamic analysis rather than a static analysis. To verify these results, an experimental investigation was carried out.

Plates with material properties and dimensions listed in Table 4.11 were clamped into a rigid support frame and tested for resonant conditions. An optical vibrometer system was used to identify and compute the resonant frequencies of these plates. Each plate tested had either a square or triangular perforation pattern, and a ligament efficiency of 0.1, 0.2, 0.4, 0.6, or 0.8.

Optical measurements utilized the doppler effects of a laser beam that reflected off the surface of the plate. The vibration of the plate due to an initial impulse caused shifts in the reflected light. It was these shifts that were used to compute resonant frequencies. Impact tests were also run with an accelerometer to confirm the optical equipment. As expected the accelerometer data leads to higher frequencies due to the added mass of the accelerometer. Because of this the optical results are believed to be more accurate and are therefore presented in Figs. 4.33 and 4.34. Static effective theory has also been added to the figures for comparison purposes.

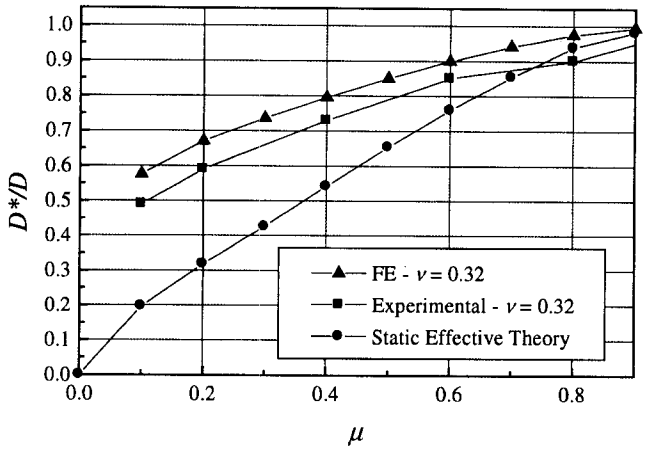

Fig. 4.33. Experimental and FE dynamic effective stiffness results for the fundamental mode of square clamped plates with square perforation patterns.

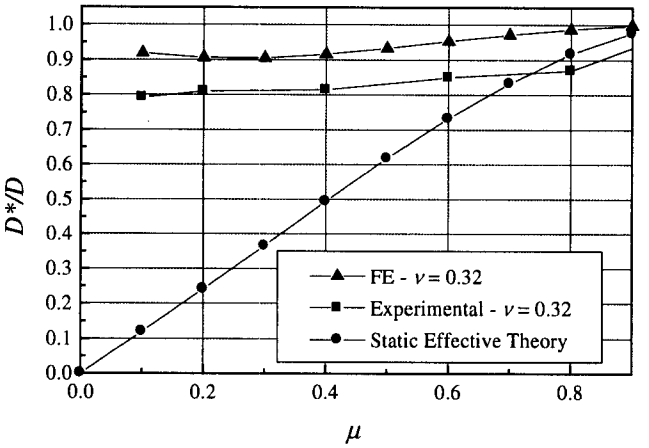

Fig. 4.34. Experimental and FE dynamic effective stiffness results for the fundamental mode of square clamped plates with square perforation patterns.

4.5.7 Conclusions

The vibration characteristics of perforated plates are important when designing structures where resonance or fatigue are possible modes of failure. Literature review of methods for predicting perforated plate vibrations showed that no design curves for this analysis have been developed. Essentially, there are no analytical, numerical, or experimental data available that would enable a designer to predict the dynamic response of perforated plates.

For this study, finite element models were developed to determine the natural frequencies and mode shapes of perforated plates. In order to approximate an infinitely

perforated square plate a large number of perforations were used. Two basic models were then developed, one with a square penetration pattern and the other with a triangular pattern. Adjusting parameters on these models, such as ligament efficiency, was computationally straightforward and thus this method of analysis was very effective for parametric studies.

Parametric studies were carried out to investigate the effects of various material properties. Results show that by decreasing Poisson's ratio, the effective stiffness values increase, however the general trend of stiffness as a function of ligament efficiency remains constant. Material density, on the other hand, has no effect on the dynamic effective stiffness.

Perforated plate mode shapes are essentially independent of perforation size and type. The analytical shapes determined from classical plate theory apply to all the perforated plates examined. The only effect the perforations have on the dynamic characteristics is via structural frequency change. Knowing this, it should be possible to predict the frequency of each mode for all perforated plates. This is an important first step toward understanding more complex problems where either the perforation pattern does not cover the entire structure, the holes are not circular, or the structure has curvature, such as a shell.

4.6 Reactor Components - Beam/Cooling Tubes

A major problem in ICF reactor design is the protection of the first wall from x-rays, neutrons, target debris and mechanical shock resulting from target ignition. The concept of protecting the cylindrical cavity by an annular bank of vertical tubes conveying liquid lithium/lead has been proposed in a number of reactor designs, i.e., HIBALL and LIBRA. A set of five different computer codes have been developed to model the vertical tube's response to planar impulsive excitations. A brief description of each code is given below:

- **B-Tube** (Braided Tube):

  A braided silicon carbide tube conveying liquid coolant is modeled as a tube with no bending stiffness but having an constant internal fluid flow. The hollow "string-like" model is preloaded with an axial tension to provide the structural load carrying capability. The nonplanar, nonlinear equations of motion were previously derived by Engelstad [25]. Numerical integration routines have now been written to solve the differential equations of motion and simulate the tube response to sequential impulses. The code's adjustable parameters include the repetition rate of the reactor (i.e., the period of the sequential impulses), the excitation magnitude, the velocity of the internal fluid, the damping in the system and the geometry of the tube. The code reports data for the midspan displacement of the tube as a function of time. With this data both the steady state and transient response of the tube can be studied. Also, the amplitude-frequency relationships identifying resonance conditions can be determined. With this code, it has been shown that the primary response of the tube will be a radial displacement (or planar displacement), however, the tubes could begin to "whirl" under certain operating conditions.

- **E-Tube** (Extensional Tube):

  This code models an "elastic" tube clamped at both ends conveying a liquid coolant while subjected to planar sequential impulses. In this case, the tube has an actual bending stiffness so no preload axial tension is needed. It is also assumed that the clamped end conditions are rigidly fixed and the length of the tube will extend during oscillatory motion. The nonplanar, nonlinear equations of motion were previously derived by Lee [26]. A computer code has now been generated to simulate the dynamic response of the tube. The adjustable parameters and data output are similar to the B-Tube code. This code also demonstrates that the tube could enter "whirling" motion under certain operating conditions.

- **I-Tube** (Inextensional Tube):

  The I-Tube code package is similar to the nonlinear E-Tube code with clamped boundary conditions that move freely in the axial direction. Consequently, longitudinal deformation does not occur. Again, the nonplanar, nonlinear equations of motion were previously derived by Lee [26]. The adjustable parameters and data output are similar to the B-Tube code.

• **S-Tube** (Stress Tube):

This code models the planar displacement and bending stress in a elastic tube with arbitrary boundary conditions conveying liquid coolant subjected to planar sequential impulses. A major feature of this code is that the stress and displacement histories for any location along the length of the tube can be calculated, in contrast to the above three codes where only displacement at the center of the tube is returned. Another feature of the program is the ability to easily model any combination of classic boundary conditions; for example pinned-pinned, clamped-clamped, pinned-clamped; by using their associated orthogonal shape functions.

The general equation of motion describing the planar mechanical response of a tube under sequential impulse loading can be found in [27]. A modal solution of the equation of motion for arbitrary boundary conditions is also given. This solution was programmed in the S-Tube code. In the above derivation the following assumptions were made. The pressure load is assumed to be uniformly distributed over the length of the tube, is impulsive in nature and is applied at the rep rate of the reactor. Since the flow velocity of the liquid coolant is small, the effects of moving liquid within the tube can be neglected and the fluid considered stationary. Stationary fluid in a tube adds mass to the system without change the flexural rigidity of the tube. Rayleigh damping was used to model internal structural damping and external viscous damping. The code's adjustable parameters include the repetition rate of the reactor, the excitation magnitude, the tube geometry, and the material properties of the tube and liquid coolant.

Figure 4.35 shows for particular input parameters the absolute maximum steady state midspan displacement of a clamped-clamped tube as a function of sequential impulse frequency. This figure illustrates the frequencies or repetition rates associated with resonant conditions, i.e., the peaks in the response curves. The large peak in the center of the figure is the fundamental frequency of the system and the peaks to the left are overtones of the fundamental frequency. These peaks would effectively shift as the length of the tube changes. Therefore, this program can be used to establish the free span tube length in order to place the reactor's operating rep rate away from the resonant peaks.

• **FEM-Tube** (Finite Element Model):

A finite element model of a tube conveying coolant fluid under sequential impulse loading was also constructed using the commercially available program ANSYS. The finite element model confirms the displacement and stress results from the above analytical solutions. Figure 4.36 compares the transient displacement of a pinned-pinned tube subjected to sequential impulses at a frequency of 3.8 Hz.

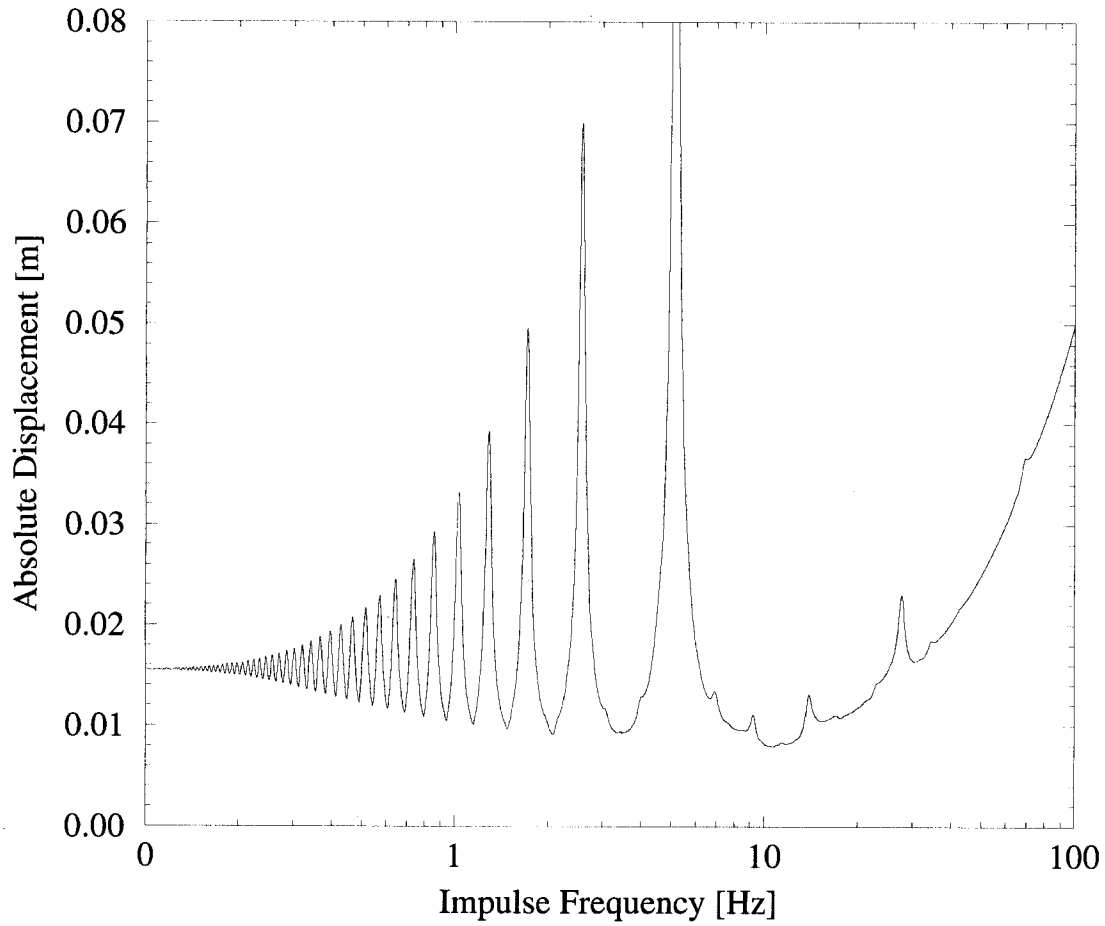

Fig. 4.35. Absolute maximum steady state midspan displacement of a pinned-pinned tube driven by sequential impulses.

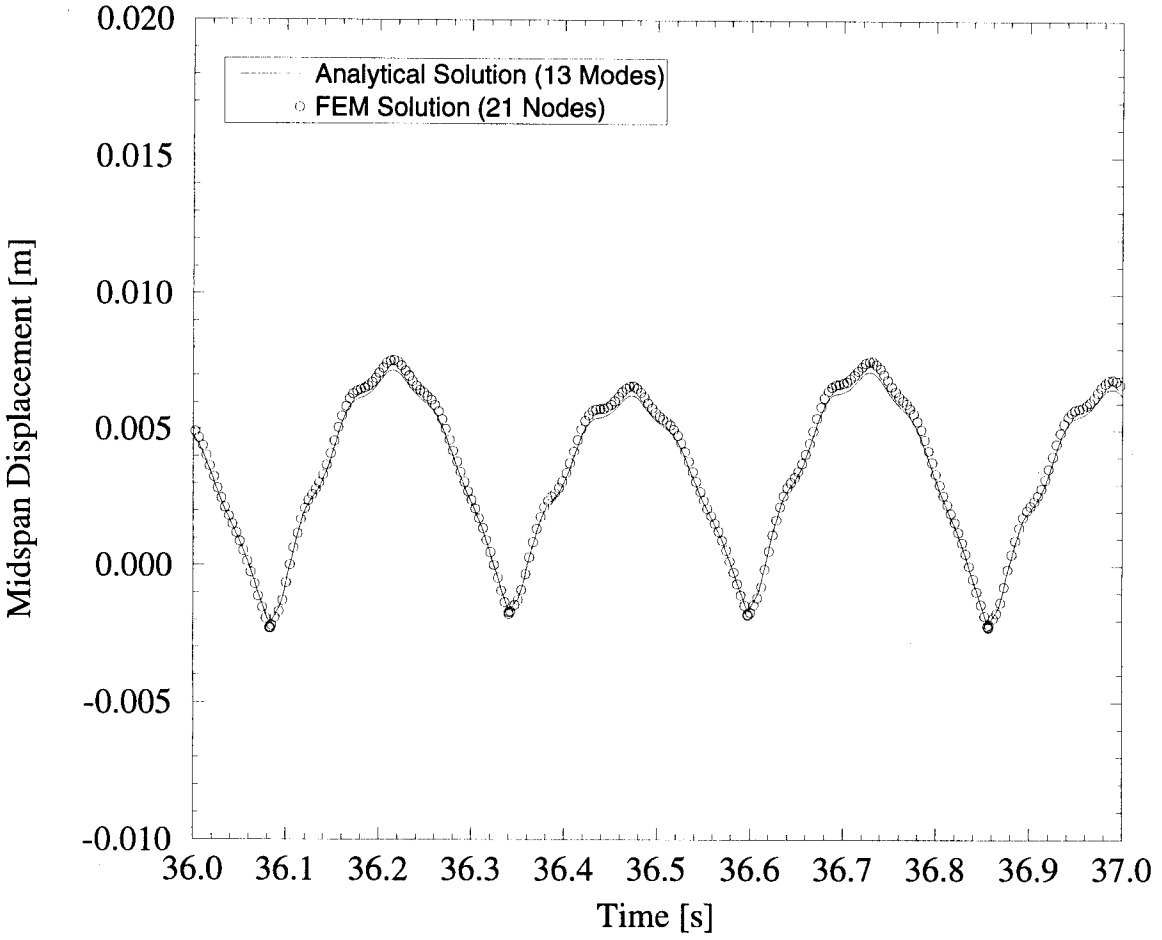

Fig. 4.36. Comparison between the analytical S-Tube code and a FEM-Tube code.

4.7 References

[1] Cousseau, P. L., "Vibration of Perforated Circular Cylinders," Ph.D. Thesis Proposal, Mechanical Engineering Department, University of Wisconsin - Madison, 1996.

[2] Cousseau, P., Schlax, M., Engelstad, R. and Lovell, E., "Natural Frequencies of Perforated Cylindrical Shells," *Proceedings of the 16th International Modal Analysis Conference*, Santa Barbara, CA, February 1998.

[3] Peterson, P. F. and Scott, J. M., "The Mini-Chamber, an Advanced Protection Concept for NIF," *Proceedings from the 12th Annual Conference of the American Nuclear Society*, Reno, NV, June 1996.

[4] Sprague, M. A., "The Vibration of Perforated Hemispherical Shells," B.S. Thesis, Mechanical Engineering Department, University of Wisconsin - Madison, 1997.

[5] Kaap, D. L., "Dynamic Effective Elastic Constants for Perforated Plates with Square or Triangular Penetration Patterns," M.S. Thesis, Mechanical Engineering Department, University of Wisconsin - Madison, 1997.

[6] Kaap, D. L., Lovell, E. G. and Engelstad, R. L., "Natural Frequencies of Plates with Uniform Perforations," *Proceedings of the 16th International Modal Analysis Conference*, Santa Barbara, CA, February 1998.

[7] Mogahed, E. A., Cousseau, P., et al., "A Novel First Wall Protection Scheme for Ion Beam ICF," *Proceedings of the 16th IEEE/NPSS Symposium on Fusion Engineering*, Champaign, IL, October 1995.

[8] Leissa, A. W., "Vibrations of Shells," NASA SP-288, 1973.

[9] Forsberg, K., "Influence of Boundary Conditions on the Modal Characteristics of Thin Cylindrical Shells," *American Institute of Aeronautics and Astronautics Journal*, Vol. 2, No. 12, 1964, pp. 2150-2157.

[10] Forsberg, K., "A Review of Analytical Methods used to Determine the Modal Characteristics of Cylindrical Shells," National Aeronautics and Space Administration CR-613, Washington, D.C., 1965.

[11] Ludwig, A. and Krieg, R., "An Analytical Quasi-Exact Method for Calculating Eigenvibrations of Thin Cylindrical Shells," *Journal of Sound and Vibration*, Vol. 74, No. 2, 1981, pp. 155-174.

[12] Powers, J. W., "Structural and Fatigue Analysis of the Sandia Laboratory Microfusion Reactor Chamber," M.S. Thesis, Department of Mechanical Engineering, University of Wisconsin-Madison, 1991.

[13] Adler, D. P., "The Effect of End Conditions on the Axisymmetric Vibrations of Cylindrical Shells," M.S. Thesis, University of Wisconsin-Madison, 1993.

[14] Love, A. E. H., A Treatise on the Mathematical Theory of Elasticity, Dover, New York, 1944.

[15] Markus, S., "The Mechanics of Vibrations of Cylindrical Shells," Elsevier Science Publishing, New York, 1988.

[16] Soedel, W., *Vibrations of Shells and Plates*, Marcel Dekker, Inc., New York, 1993.

[17] Blevins, R. D., *Formulas for Natural Frequency and Mode Shape*, Robert E. Krieger Publishing Co., Malabar, Florida, 1987.

[18] Eikrem, A. K. A., and Doige, A. G., "Natural Frequencies of a Hemispherical Shell," *Experimental Mechanics*, December, 1972, pp. 575-579.

[19] Singh, A. V., and Mirza, S., "Asymmetric Modes and Associated Eigenvalues for Spherical Shells," *Journal of Pressure Vessel Technology*, 1985, Vol. 107, pp. 77-82.

[20] CODAP, Code Francais de Construction des Appareils a Pression, 1985.

[21] ASME Boiler and Pressure Vessel Code - 1995, Section III - Division 1 - Appendices, Article A-8000, pp. 210-223, 1995.

[22] Osweiller, F., "Evolution and Synthesis of the Effective Elastic Constants Concept for the Design of Tubesheets," *Journal of Pressure Vessel Technology*, Vol. 111, pp. 209-217, 1989.

[23] Slot, T., "Stress Analysis of Thick Perforated Plates," Technomic Publishing, Westport, CT, 1972.

[24] Leissa, A. W., "Vibration of plates," NASA SP-160, 1969.

[25] Engelstad, R. L., "Vibration and Stability of Vertical Tubes Conveying Fluid Subjected to Planar Excitation," Ph.D. Thesis, Engineering Mechanics Department, University of Wisconsin - Madison, 1988.

[26] Lee, Y.-M., "Nonlinear Vibration and Stability of a Beam Subjected to Planar Excitations," Ph.D. Thesis, Mechanical Engineering Department, University of Wisconsin - Madison, 1994.

[27] B. Badger et al., "LIBRA-SP - A Light Ion Fusion Reactor Design Study Utilizing a Self-Pinched Mode of Ion Propagation, Report for the Period Ending June 30, 1995," University of Wisconsin Fusion Technology Institute Report UWFDM-982, June 1995.

U.S. Department of Energy

Contract No. DE-AS08-88DP10754

The Development and Application of
Advanced Analytical Methods
to Commercial ICF Reactor Chambers

Task 5
Final Report

Analysis of Self-Consistent Target Chamber Clearing

Fusion Technology Institute
University of Wisconsin-Madison

Cavity Clearing

1. INTRODUCTION

In Inertial Confinement Fusion (ICF) reactors, the performance of the reactor cavity is of paramount importance to the overall qualification of the reactor. Controlling the initial conditions of the gas in the reactor cavity prior to every microexplosion is the key to many crucial aspects related to the performance of the reactor cavity. The immediate pre-explosion gas pressure and the concentration (mass density) of different species in the reactor cavity atmosphere have a strong direct effect on the efficiency and performance of the reactor.

Predicting the initial conditions of the gas in the reactor cavity prior to every microexplosion with a reasonable degree of accuracy is highly desirable to insure a successful reactor design. Clearing the products of the microexplosion (condensable vapors, noncondensable gases, target fragments, etc.) is normally achieved by either self-pumping of the high pressure/temperature gases through ports in the reactor cavity walls or by mechanical evacuation. These ports are usually connected to a large dumping tank. Hard vacuum pumps are connected to the dumping tank to assure constant low pressure during reactor operation. There is a major additional contribution from the vapor condensation process either in droplet form or from thin film condensation on various cold surfaces in the cavity. The dynamics of this system from the time of the target explosion until the time of next explosion (This period of time is proportional to the reciprocal of the repetition rate.) is the subject of this proposed work.

The goals of this project are to:

1. Analyze the transient hydrodynamics of the clearing system.
2. Evaluate the effects of the evaporation and recondensation of the first wall and target materials.
3. Evaluate the needed rate of pumping.

2. BACKGROUND

The cavity atmosphere is primarily dictated by the requirements needed to propagate the beams to the target with minimum loss due to stripping and charge exchange. The equilibrium pressure of the noncondensable gases (D_2, T_2, and He, Ar, Xe, etc.) has to be maintained reasonably low, although its effect on beam propagation is not as great as the vapor of liquid or solid metals at the same number density. Furthermore, the noncondensable partial pressure has

to be kept low because it constitutes a continuous source of molecules migrating into the beam lines where the pressure must be kept at a very low value depending upon whether heavy ion, light ion, or laser drivers are used.

Immediately after a shot, the gas pressure in the cavity reaches as high as 100 torr. Immediately near the cavity inner surfaces the local pressure exceeds that value by many orders of magnitude due to the vaporization of the surface material for dry wall designs or due to the vaporization of the liquid metals for designs using wetted walls. Due to rapid expansion near the wall droplet formation is expected and the internal surfaces of the cavity act as a condenser for the remainder of the condensable vapors. Accurate prediction of the condensation state either on the cavity cold internal surfaces or in the form of droplets is required to insure that the condensation is rapid enough to achieve the desired repetition frequency of several hertz.

3. PROBLEM FORMULATION

The issue of metal vapor condensation, either from the wetted or dry wall concept, may be divided into three fundamental problems:

1. Homogeneous droplet nucleation in a supersaturated vapor within the body of the gas-vapor mixture inside the cavity.
2. Heterogeneous droplet nucleation.
3. Liquid film condensation on the rather cold surfaces of the cavity interior.

The three fundamental problems will be addressed briefly in the next discussion.

3.1. Homogeneous Droplet Nucleation

Clearly, as condensation progresses, the mass fraction of liquid metal will change. Thus, the partial pressure of the metal vapor will be affected. Now we will consider the nucleation rate equation.

The single-component nucleation rate is given from classical liquid drop nucleation theory as discussed by Hill, et al. [1], as:

$$J = \left(\frac{P_v}{KT}\right)^2 \frac{M}{N_A \rho_l} \sqrt{\frac{2\sigma}{\pi m}} \exp\left(\frac{-4\pi\sigma r_c^2}{3KT}\right) \tag{1}$$

where

J Nucleation rate per unit volume

P_v Local vapor partial pressure of liquid metal

K Boltzman constant = 1.38054×10^{-23} J/molecules K

M Molecular weight

N_A Avogadro's number = 6.03×10^{26} molecules/kg mol

ρ_l Liquid density

m Molecular mass = M/N_A

T Local vapor flow temperature

σ Surface tension

r_c Critical radius

The critical radius is the radius where the drop has equal probability of growth or decay, and is given by:

$$r_c = \frac{2\sigma}{\rho_l R\, T \ln\left(\frac{P_v}{P_{s\infty}}\right)} \tag{2}$$

where

ρ_l Liquid density

R Universal gas constant

P_v Partial pressure of liquid metal

$P_{s\infty}$ Flat film saturation pressure

The number of molecules in the droplet n_e is found as

$$n_e = \frac{4}{3}\frac{\pi r_c^3 \rho_l N_A}{M}. \tag{3}$$

Using Eq. (2) to eliminate r_c from the previous expression for the nucleation rate per unit volume J, Eq. (1) becomes:

$$J = \left(\frac{P_v}{KT}\right)^2 \frac{M}{N_A \rho_l}\sqrt{\frac{2\sigma}{\pi m}} \exp\left(\frac{-16\pi\sigma^3}{3KT^3(\rho_l R)^2}\left(\ln\left(\frac{P_v}{P_{s\infty}}\right)\right)^{-2}\right) \tag{4}$$

where

J Nucleation rate per unit volume ($m^{-2}\ s^{-1}$)

P_v Local vapor partial pressure of liquid metal

K Boltzman constant = 1.38054×10^{-23} J/molecules K

M Molecular weight

N_A Avogadro's number = 6.03×10^{26} molecules/kg. mol

ρ_l Liquid density

m Molecular mass = M/N_A

T Local vapor flow temperature

σ Surface tension

The drop is in equilibrium only if the vapor is supersaturated. In other words, the drop is in equilibrium at a specified temperature only if the pressure of the surrounding vapor exceeds its saturation pressure $P_{s\infty}$. An equilibrium of a drop with its vapor is unstable since the drop will grow if its diameter suddenly experiences either an infinitesimal size increase as a result of condensation or sudden infinitesimal size to decrease due to evaporation. The initial drop size must therefore be larger than the critical size for the droplet to grow. Hill, et al. [1] concluded that the initial droplet size corresponding to a zero probability of decay is achieved around 1.3 times the critical radius. The minimum drop size cannot be smaller than the average distance between liquid molecules; such a limitation allows an estimate of the maximum supersaturating or the minimum subcooling that can exist without condensation.

The supersaturating limit data for lead are compared with the corresponding limits predicted by Eq. (4) with J taken to be 10^{14} m^{-3} s^{-1}. The choice of $J = 10^{14}$ m^{-3} s^{-1} for droplet nucleation was made by Frurip and Bauer [2] to provide a best fit to droplet nucleation available data. The value of $(P_v)_{SSl}$ the vapor pressure at the supersaturating limit for $T = T_v$, predicted by Eq. (4) varies weakly with J, so uncertainty in J does not strongly affect the accuracy of the predicted supersaturating limit.

Figure 1 shows the supersaturation limit of PbLi as a function of temperature. Figure 2 shows the supersaturation limit pressure ratio for lead, $J = 10^{14}$ m^{-3} s^{-1}. To determine $(T_v)_{SSl}$ for a given vapor pressure P_v using Eq. (4) with $J = 10^{14}$ m^{-3} s^{-1} requires an iterative calculation because of the implicit temperature dependence of $P_{s\infty}$ and σ. However, it can be shown that the following relation approximates Eq. (4) to a high degree of accuracy (to within less than 0.5%):

$$\frac{(P_v)_{SSl}}{P_{s\infty} T_v} = \exp\left\{\left[\frac{E^*(-\ln J^*)^{1/2}}{2\left(E^*\right)^{1/2} + (-\ln J^*)^{3/2}}\right]^{1/2}\right\}$$

where the dimensionless variables J^* and E^*, which are functions only in T_v, are

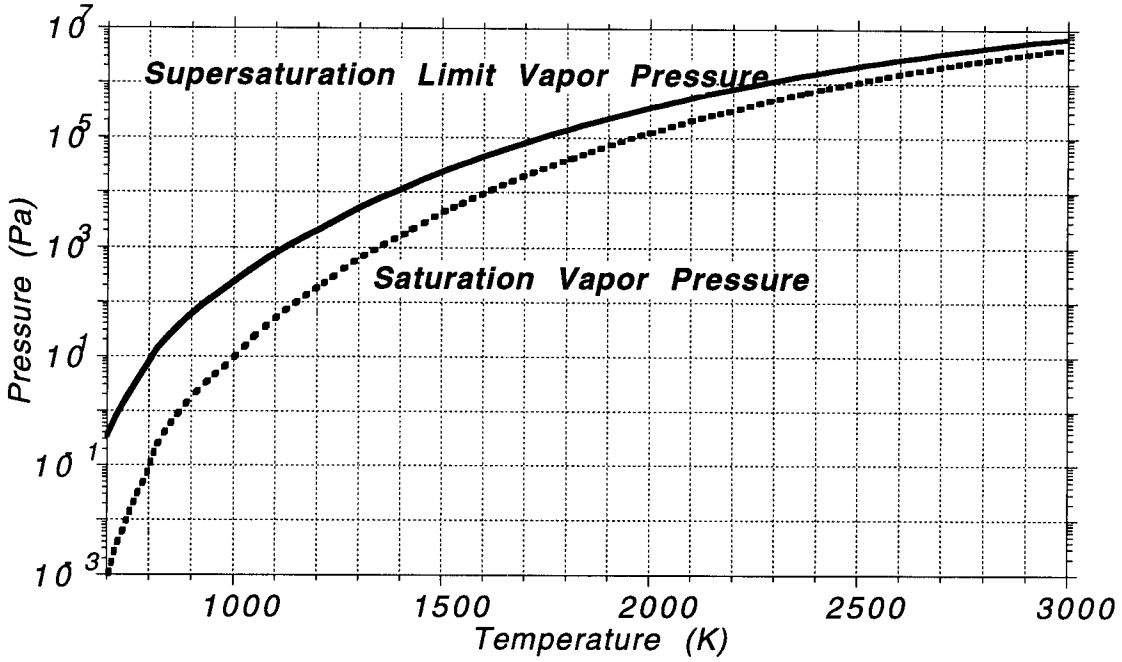

Figure 1. The supersaturating limits predicted by Eq. (4) with J taken to be 10^{14} m^{-3} s^{-1} for lead are compared with the corresponding saturation vapor pressure at the same temperature T_v.

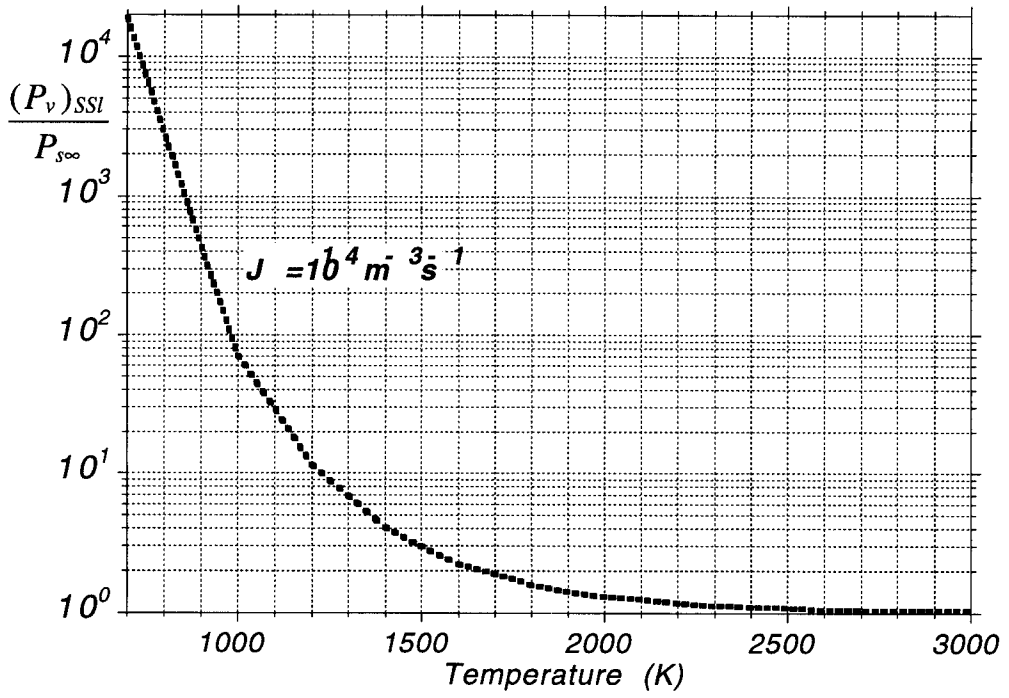

Figure 2. The supersaturating limit pressure ratio for lead with J taken to be 10^{14} m^{-3} s^{-1}.

$$J^* = \frac{\rho_l MJ}{N_A}\left(\frac{\pi M}{2\sigma N_A}\right)^{1/2}\left[\frac{RT_v}{P_{s\infty}(T_v)}\right] \quad \text{and} \quad E^* = \frac{16\pi\sigma^3}{3KT_v{}^3(\rho_l R)^2}.$$

The following are the physical data of liquid lead used in these calculations:

Atomic weight (based on ^{12}C)	207.19
Atomic volume (cm^3/g-atom)	18.27
Atomic radius (Å)	1.75
Surface tension σ(T) (N/m)	$0.514 - 9 \times 10^{-5}$ T(K)
Liquid density ρ_l(T) kg/m^3	1.07×10^4 - 1.2 T(K)
Melting point/Boiling point (K)	600.4/2022
ΔH_{fus} (kJ/mol	4.772
ΔH_{vap} (kJ/mol)	179.5 (866345.6 J/kg)
Saturation vapor pressure (Pa)	133.3224 exp(17.86-22300/T(K)).

To estimate the degree of subcooling $T_{s\infty} - T_v$ we utilize the Clausius-Clapeyron equation [3], relating saturation pressure and temperature,

$$T\frac{dP}{dT} = \frac{h_{fg}}{v_v - v_l} \tag{5}$$

where

v_v Specific volume of vapor = $1/\rho_v$

v_l Specific volume of liquid = $1/\rho_l$

h_{fg} Latent heat of vaporization per mole.

To obtain, assuming the vapor to be a perfect gas and $v_v \gg v_l$,

$$\ln\left(\frac{P_v}{P_{s\infty}}\right) = h_{fg}\frac{1/T_v - 1/T_{s\infty}}{R} \tag{6}$$

The critical radius r_c in terms of subcooling $T_{s\infty} - T_v$ is estimated to be

$$r_c = \frac{2\sigma}{\rho_l h_{fg}}\frac{T_{s\infty}}{T_{s\infty} - T_v} = \frac{2\sigma}{\rho_l h_{fg}}\frac{1}{\left(1 - \frac{T_v}{T_{s\infty}}\right)} \tag{7}$$

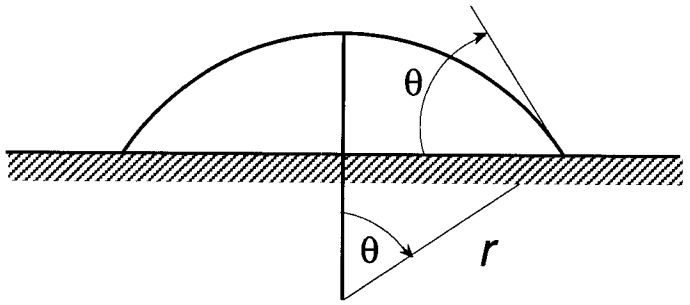

Figure 3. An embryo liquid droplet formed at an idealized liquid-solid interface.

where

T_v Vapor temperature

$T_{s\infty}$ Saturation temperature.

Fig. 4 shows graphically the relationship between r_c, $(\frac{T_v}{T_{s\infty}})$ and $\frac{P_v}{P_{s\infty}}$. It is clear from the above discussion that it is in fact possible for a vapor to be in a highly supersaturated state without condensation occurring. This behavior can play a major role in many circumstances of practical interest, including cloud (fog) formation and precipitation in the ICF reaction chambers during rapid expansion of liquid metal-gas mixture.

3.2. Heterogeneous Nucleation in Vapor

In most applications involving condensation, the process is initiated by removing heat through the walls of the structure containing the vapor to be condensed. In our present case, the microexplosion provides enough energy to heat up the gas in the cavity and to evaporate some of the liquid metal coolant. If enough heat is removed by the coolant, the vapor near the rather cold wall may be cooled below its equilibrium saturation temperature for the specified system pressure. Since the heat removal process will establish a temperature field in which the temperature is lowest right at the wall of the containment, the formation of a liquid droplet embryo is most likely to occur right on the solid-vapor surface. The formation of a liquid embryo at the interface between a metastable super-saturated vapor and another solid phase is one type of heterogeneous nucleation. Figure 3 shows a schematic of such an embryo. Figures 4 and 5 show the relationship between the critical radius, temperature ratio and pressure ratio for different vapor temperatures for lead.

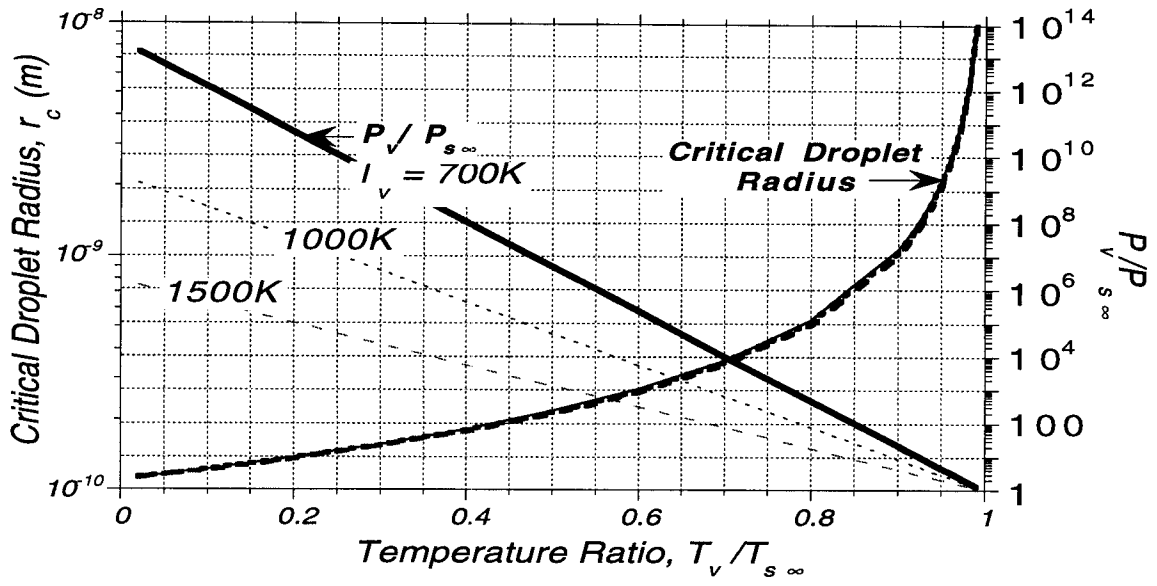

Figure 4. The relationship between r_c, $\frac{T_v}{T_{s\infty}}$ and $\frac{P_v}{P_{s\infty}}$. for different vapor temperatures T_v.

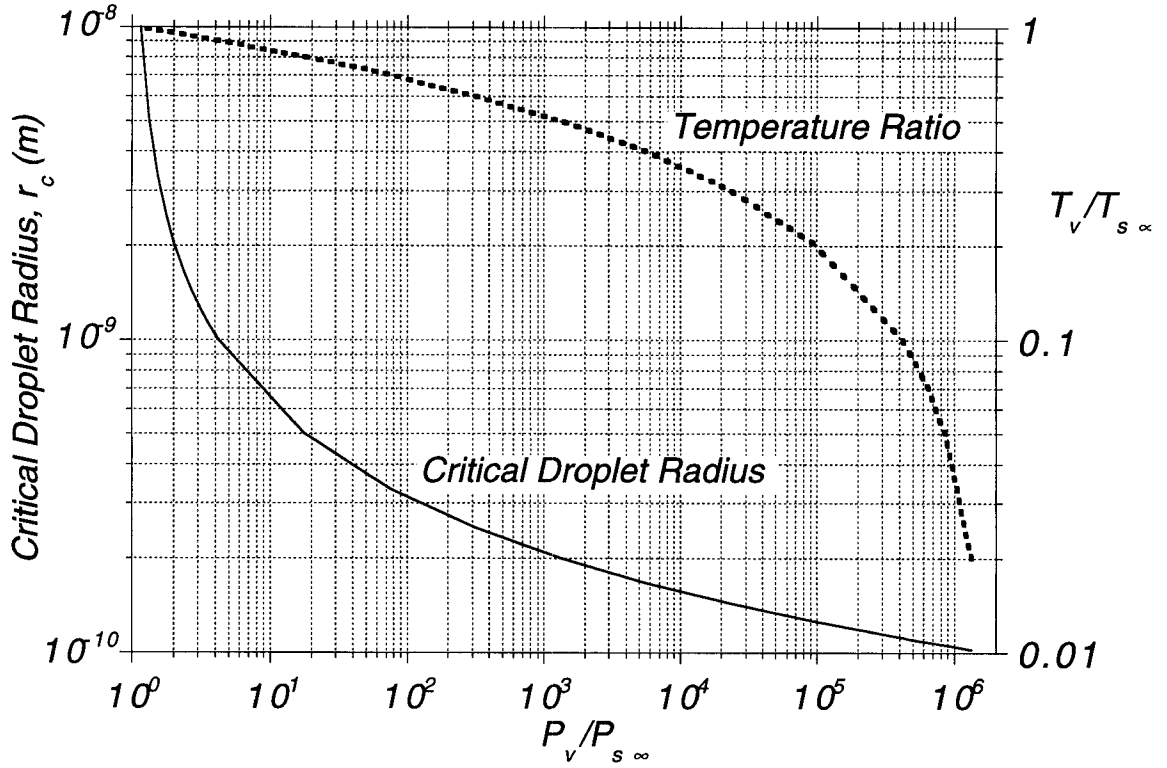

Figure 5. The relations between r_c, $\frac{T_v}{T_{s\infty}}$ and $\frac{P_v}{P_{s\infty}}$ for different vapor temperature T_v.

As in the case of heterogeneous nucleation of vapor bubbles, the analysis of homogeneous nucleation of liquid droplets can be extended to heterogeneous nucleation at a solid-vapor interface. Because the analysis of the kinetics of the heterogeneous nucleation process is very similar to that described in the previous section for the comparable homogeneous nucleation process, the analysis for heterogeneous nucleation will be only briefly summarized here. If the solid surface is idealized as being perfectly smooth, in general, the shape of a droplet at the surface will be dictated by the shape of the surface itself, the interfacial tension σ, and the contact angle θ. For a flat, solid surface, the embryo liquid droplet will have a profile like that shown in Figure 3. We will specifically consider the heterogeneous nucleation process in which formation of a droplet embryo occurs in a system held at constant temperature T_V and pressure P_V. If the embryo shape is idealized as being a portion of a sphere, it follows directly from its geometry that the embryo volume V_l and the areas of the liquid-vapor (A_{lv}) and the solid-liquid interfaces (A_{sl}) are given by:

$$V_l = [\pi r^3/3] (2 - 3 \cos \theta + \cos^3 \theta) \tag{8}$$

$$A_{lv} = 2 \pi r^2 (1 - \cos \theta) \tag{9}$$

$$A_{sl} = \pi r^2 (1 + \cos \theta) . \tag{10}$$

In the above relations, θ is the liquid contact angle and r is the spherical cap radius indicated in Fig. 3.

The availability function ($\Delta\Psi(r)$) of the system is usually associated with the maximum (reversible) work that can be extracted from the system to bring it entirely to an equilibrium reference state at T_l and P_l:

$$\Delta\Psi (r) = (4/3) \pi r_e^2 \sigma_{lv} F - (4/3) \pi \sigma_{lv} F [2 + P_l/P_{ve}] (r - r_e)^2 + \ldots \tag{11}$$

where F is defined by:

$$F = (2 - 3 \cos \theta + \cos^3 \theta)/4 .$$

Noting that the term in square brackets in Eq. (11) is approximately equal to 2, because $P_l \ll P_{ve}$. The expansion of $\Delta\Psi(r)$ indicates that $\Delta\Psi$ has a local maximum at $r = r_e$. $\Delta\Psi$ also approaches zero as $r \rightarrow 0$.

It is known from basic thermodynamic considerations that equilibrium requires that the change in the total availability approach zero, and the total availability of the system (Y) must be

a minimum for stable equilibrium. Spontaneous internal changes always result in a decrease in the availability of the system.

It follows directly from the same arguments presented for the homogeneous case in the previous section that the equilibrium condition corresponds to a maximum value of the change of the availability of the system ($\Delta\Psi$) and is therefore an unstable equilibrium. As in the homogeneous case, $\Delta\Psi$ is expected to increase to a maximum and then decrease with increasing radius r. This once again leads to the conclusion that embryos having a radius less than r_e spontaneously disappear, while those having a radius greater than r_e spontaneously grow.

The determination of the kinetic limit of supersaturation of the heterogeneous nucleation is similar to that for the homogeneous nucleation case considered previously. The details are virtually identical to those of the homogeneous nucleation analysis presented, and hence they will not be presented here. There are, however, two important differences in the heterogeneous nucleation analysis. First, as an initial step in the analysis, it is postulated that, at equilibrium, the number density of embryos containing n molecules per unit of interface area N_n is given by:

$$N_n = N_v^{2/3} \exp [- \Delta\Psi(r)/\mathrm{K}\, T_v] \qquad (12)$$

where N_v is the number density of vapor molecules per unit volume and $\Delta\Psi(r)$ is the availability function previously defined. For the heterogeneous nucleation process considered here, only vapor molecules near the solid surface can participate in embryo droplet formation. To account for this condition, the factor multiplying the exponential term in Eq. (12) is taken to be $N_v^{2/3}$, which is representative of the number of vapor molecules immediately adjacent to the solid surface per unit of surface area.

The second different aspect of the heterogeneous analysis is the relationship between the number of molecules n in the embryo and its radius:

$$n = [N_A \pi \mathrm{r}^3/ 3M v_l] (2 - 3 \cos\theta + \cos^3\theta) . \qquad (13)$$

This relation differs from that used in the analysis of homogeneous nucleation because the embryo geometry is different. Analysis of the kinetics of the heterogeneous nucleation process incorporates these two changes and makes use of the expansion for $\Delta\Psi$ developed for this case.

Carrying the analysis to completion yields the following relation between the rate of embryo formation J ($\mathrm{m}^{-2}\ \mathrm{s}^{-1}$) and the system conditions and properties:

$$J = \left(\frac{2\sigma F N_A}{\pi M}\right)^{1/2}\left(\frac{P_v}{RT_v}\right)^{5/3}\left(\frac{N_A}{M}\right)^{2/3} v_l F$$
$$\left(\frac{1-\cos\theta}{2}\right)\exp\left(\frac{-16\pi(\sigma F / RT_v)^3 v_l{}^2 N_A}{3M\left\{\ln[P_v / P_{s\infty}]\right\}^2}\right) \qquad (14)$$

where F is defined as before.

Hence if the equilibrium contact angle θ is zero (i.e. if there is complete "wetting" of the substrate by the condensate), the critical free energy of droplet formation equals zero and nucleation will be most rapid. If θ is taken to be 180° and $N_v^{2/3}$ is replaced by N_v, corresponding to no "wetting" at all, then Eq. (14) becomes

$$J = \left(\frac{P_v}{KT}\right)^2 \frac{M}{N_A \rho_l}\sqrt{\frac{2\sigma}{\pi m}}\exp\left(\frac{-16\pi\sigma^3}{3KT^3(\rho_l R)^2}\left(\ln\left(\frac{P_v}{P_{s\infty}}\right)\right)^{-2}\right) \qquad (15)$$

where

J Nucleation rate per unit volume (m^{-2} s^{-1})
P_v Local vapor partial pressure of liquid metal
K Boltzman constant = 1.38054×10^{-23} J/molecules K
M Molecular weight
N_A Avogadro's Number = 6.03×10^{26} molecules/kg mol
ρ_l Liquid density
m Molecular mass = M/N_A
T Local vapor flow temperature
σ Surface tension

obtained in the previous section for homogeneous droplet nucleation analysis.

As in the homogeneous nucleation case, J is interpreted as the rate at which embryos of critical size are generated. As J increases, the probability that a bubble/droplet will exceed critical size and grow spontaneously becomes greater. If a threshold value of J is specified as corresponding to the onset of nucleation, the corresponding vapor temperature $T_v = (T_v)_{SSL}$ for the specified system pressure can be determined from Eq. (14). Alternatively, for the specified threshold J value, the limiting supersaturation pressure can be determined for a given system temperature.

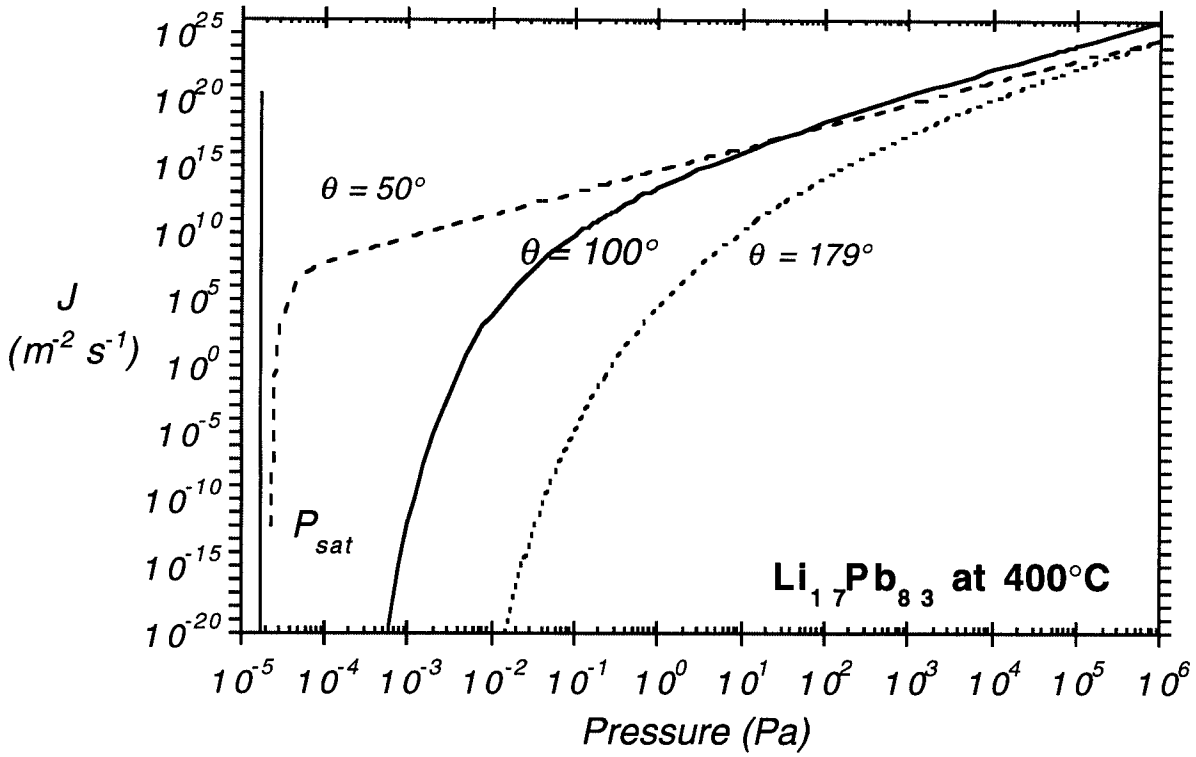

Figure 6. Variation of the rate of embryo formation at a $Li_{17}Pb_{83}$-solid interface with vapor pressure as predicted for different contact angles by analysis of the kinetic of embryo droplet formation.

For $Li_{17}Pb_{83}$ vapor at 400°C, the variation of J with vapor pressure as predicted by Eq. (14) is shown in Figure 6 for several values of liquid contact angle. It is clear from the graph that J at high values of P_v is not sensitive for the value of conact angle.

Assuming that a fixed threshold value of J would apply for all contact angles, it is clear that the predicted value of $(P_v)_{SSL}$ decreases with decreasing contact angle toward the normal saturation vapor pressure. At a liquid contact angle of 50° or less, the difference between the predicted $(P_v)_{SSL}$ value and $P_{sat}(T_v)$ is negligible for virtually any threshold value of J between 10^{-11} and 10^{6}.

Contact angles for virtually all real systems lie between zero and about 110°, and for metal surfaces with nonmetallic liquids, the contact angle is often below 50°. The results of the above analysis therefore suggest that condensation can be initiated at a solid surface in contact with the vapor at supersaturation levels significantly below those required for homogeneous nucleation, if the liquid phase of the vapor wets the surface reasonably well.

It is quite possible for a thin microfilm of liquid to be absorbed on all or part of a solid surface. This is particularly true for high-energy surfaces such as metals. In addition, when water is the liquid, its polar nature can enhance the tendency of water molecules to attach to portions of the solid surface. (Many oxides and corrosion-produced compounds on metal surfaces are hydrophilic.) Patches of adsorbed liquid molecules on the solid surface can thus serve as nuclei for condensation of the liquid phase when the vapor is supersaturated. Condensation on the surface can begin as the formation of very small droplets on the surface at the sites of these nuclei. This so-called dropwise condensation process is, in fact, commonly observed when water vapor in air condenses on a cold beverage glass. This is usually interpreted as being a direct consequence of the fact that the liquid poorly wets the glass, except at nuclei locations where water molecules have adsorbed to crevices (scratches) or foreign matter (such as dust particles) on the surface. Dropwise condensation is discussed further in the next section.

3.3. Dropwise Condensation

Dropwise condensation may occur on a solid surface cooled below the saturation temperature of a surrounding vapor when the surface is poorly wetted except at locations where well-wetted contaminant nuclei exist. The poorly wetted surface condition can result from contamination or coating of the surface with a substance that is poorly wetted by the liquid phase of the surrounding vapor. In practice, this can be achieved for liquid metal condensation by permanently coating the surface with a low surface-energy polymer or a noble metal. This method of promoting dropwise condensation is of particular interest because it holds the prospect of providing continuous dropwise condensation. Dropwise condensation is generally the preferred mode of condensation because the resulting heat transfer coefficient may be as much as an order of magnitude higher than that for film condensation under comparable circumstances. Recent studies by Westwater and co-workers [4, 5] have demonstrated that dropwise condensation of steam can be consistently obtained on gold and silver surfaces. The occurrence of dropwise condensation on gold and silver surfaces would appear to contradict the reasoning that high-surface-energy metal surfaces should be well wetted by the liquid phase, producing film condensation instead of dropwise condensation. During dropwise condensation, the condensate is usually observed to appear in the form of droplets, which grow on the surface and coalesce with adjacent droplets. When droplets become large enough, they are generally removed from the surface by the action of gravity or drag forces resulting from the motion of the surrounding gas. As the drops roll or fall from the surface, they merge with droplets in their path, effectively sweeping the surface clean of droplets. Droplets then begin to grow anew on the freshly exposed solid surface. This sweeping and renewal of the droplet growth process is responsible for the high heat transfer coefficients associated with dropwise condensation. Despite

numerous studies of dropwise condensation over the years, its mechanism remains the subject of debate. Two different types of models have been proposed. The first model type is based on the premise that droplet formation is a heterogeneous nucleation process like that described in Section 3.2. Droplet embryos are postulated to form and grow at nucleation sites, while portions of the surface between the growing droplets remain dry. Experimental evidence supporting this physical model of the condensation process has emerged from several experimental investigations. A model of the dropwise condensation process that includes droplet nucleation, growth, removal, and renucleation on re-exposed sites was developed by Gose et al. [6]. In the second type of dropwise condensation model, it is postulated that condensation occurs initially in a filmwise manner, forming an extremely thin film on the solid surface. As condensation continues, this film eventually reaches a critical thickness, estimated to be about 1 μm, at which point it ruptures and droplets form. Condensation then continues on the surface between the droplets that form when the film ruptures. Condensate produced in these regions is drawn to adjacent drops by surface-tension effects. Droplets also grow by direct condensation on the droplet surfaces themselves. The results of several investigations seem to support this type of interpretation of the condensation process. These results indicate that condensation occurs entirely between droplets on a very thin liquid film. In contrast, it is postulated in the first model described above that condensation occurs only on the droplets, and not on the surface between them. The rate of condensation on the larger droplets is less than on the smaller ones because of the higher resistance to heat conduction through larger drops. The large drops therefore grow primarily through coalescence. This model implies that most of the heat transfer during dropwise condensation is transferred to that portion of the surface covered with the smallest droplets. Detailed modeling of dropwise condensation heat transfer based on the first model hypothesis has, in fact, been attempted by several investigators. These models generally idealize the heat transfer process. Correlations for the heat transfer coefficient associated with dropwise condensation have been proposed by a number of investigators. One example is the following correlation, proposed by Peterson and Westwater [7] for dropwise condensation of steam and ethylene glycol:

$$\mathrm{Nu} = 1.46 \times 10^{-6} (\mathrm{Re}^*)^{-1.63} \prod_k^{1.16} \mathrm{Pr}_l^{0.5}$$

where

$$\mathrm{Nu} = \frac{2h\sigma T_{sat}}{\rho_l h_{lv} k_l (T_{sat} - T_w)}$$

$$\mathrm{Re}^* = \frac{k_l(T_{sat} - T_w)}{\mu_l h_{lv}}$$

$$\Pi_k = -\frac{2\sigma T_{sat}}{\mu_l^2 h_{lv}} .$$

While correlations of this type can be made to agree quite well with data for a specific surface and fluid combination their general applicability has not been demonstrated. The use of such a correlation for circumstances other than those for which it was developed is questionable at best. Further discussion of correlation for dropwise condensation is provided in the review article by Merte [8].

3.4. Other Factors Affecting Condensation

a. Nucleation of Droplets on Gaseous Ions

This very important case was first investigated by Thomson who showed that vapor molecules form stable clusters about all gaseous ions. The analysis showed that even at zero supersaturation the ion is surrounded by a stable shell of vapor molecules. Of course, a finite supersaturation ratio (P_l/P_e) > 1 is required for nucleation of macroscopic droplets.

b. Nucleation of Droplets on Foreign Particles of Subcritical Size

The presence of vapor impurities like dust, bring about nucleation of droplets and fog formation even though the vapor is unsaturated with respect to pure material. It is understood that this phenomenon is due to their effects in greatly lowering the vapor pressure P_e, giving rise to a large negative to the Gibbs free energy of formation of a critical cluster. Also, the presence of vapor immiscible impurities enhance the nucleation rate because of their effect in reducing the surface tension by adsorption.

4. METHODOLOGY OF CALCULATIONS

The calculations start with the final condition in the cavity after the x-rays hit the first wall (dry or wet). The amount of vaporized material, the pressure and temperature are readily calculated. The cold surface of the cooled first wall is the main sink for condensation. Then the heterogeneous nucleation in vapor would be the major condensation mechanism. Applying the relationship of the heterogeneous nucleation with the decaying background conditions of pressure/temperature linked to the amount of vapor left in the cavity gives the time change of the

mass density of the vapor between shots (microexplosion). If, at the end of the time of (1/frequency) the conditions in the cavity are not suitable for the next shot, an external means of clearing should be sought and a new set of calculations need to be performed. In the meantime, the conditions in the cavity are known; the homogeneous droplet nucleation analysis would be checked to make sure that no rain or fog will form during this period. In such a case, other methods should be sought to prevent such formation of either rain, fog or both.

4.a. Case Study:

Reactor	LIBRA-SP [9]
Coolant	PbLi
FW protection	wet FW by PbLi
Mass blown into chamber/shot	1.15 mg/cm^2
Initial pressure in the cavity	100 torr
Final pressure required in the cavity	0.52 torr
Number of PbLi molecules blown into chamber/shot	3.34×10^{22}

From Figure 6 for a contact angle of 100°, the relationship between J and P_v can be approximated by the following:

$$J\,(1/\mathrm{m}^3\mathrm{s}) = 1.1681 \times 10^{14}\ P_v^{2.0477}\,(\mathrm{Pa})\ .$$

If we assume that the pressure will decay exponentially from the initial pressure in the cavity to the final pressure in 0.3 s, the following relation can be obtained:

$$P_v = 1.33 \times 10^4 \exp\,(-17.49\ \mathrm{t(s)})\ .$$

Calculating the number of condensed molecules at the end of this time will be:

$$\int_0^{0.3} J dt = \int_0^{0.3} 3.25 \times 10^{22} e^{-35.814t} dt = 10^{21}\ \text{molecules.}$$

Comparing this number with what is already evaporated shows that another means of evacuation is needed.

5. DISCUSSION AND CONCLUSIONS

In Inertial Confinement Fusion (ICF) reactors, the performance of the reactor cavity is of paramount importance to the overall qualification of the reactor. Controlling the initial conditions of the gas in the reactor cavity prior to every microexplosion is the key to many crucial aspects related to the performance of the reactor cavity. The immediate pre-explosion gas pressure and the concentration (mass density) of different species in the reactor cavity atmosphere have a strong direct effect on the efficiency and performance of the reactor.

Predicting the initial conditions of the gas in the reactor cavity prior to every microexplosion with a reasonable degree of accuracy is highly desirable to insure a successful reactor design. Clearing the products of the microexplosion (condensable vapors, noncondensable gases, target fragments, etc.) is normally achieved by either self-pumping of the high pressure/temperature gases through ports in the reactor cavity walls or by mechanical evacuation. These ports are usually connected to a large dumping tank. Hard vacuum pumps are connected to the dumping tank to assure constant low pressure during reactor operation.

There is a major additional contribution from the vapor condensation process either in droplet form or from thin film condensation on various cold surfaces in the cavity. The dynamics of this system from the time of target explosion until the time of the next explosion is greatly affected by too many factors. The cavity atmosphere is primarily dictated by the requirements needed to propagate the beams to the target with minimum loss due to stripping and charge exchange. The equilibrium pressure of the noncondensable gases (D_2, T_2, and He, Ar, Xe, etc.) has to be maintained reasonably low, although its effect on beam propagation is not as great as the vapor of liquid or solid metals at the same number density. Furthermore, the noncondensable partial pressure has to be kept low because it constitutes a continuous source of molecules migrating into the beam lines where the pressure must be kept at a very low value depending upon whether heavy ion, light ion, or laser drivers are used.

Immediately after a shot, the gas pressure in the cavity reaches as high as 100 torr. Near the cavity inner surfaces, the local pressure exceeds that value by many orders of magnitude due to the vaporization of the surface material in the case of dry wall designs or due to the vaporization of the liquid metals in designs using wetted walls. Due to rapid expansion near the wall, droplet formation is expected and the internal surfaces of the cavity act as condensers for the remainder of the condensable vapors. Accurate prediction of the condensation state either on the cavity internal cold surfaces or in the form of droplets is required to insure that the condensation is rapid enough to achieve the desired repetition frequency.

The issue of metal vapor condensation, either from the wetted or dry wall concepts, may be divided into three fundamental problems:

1. Homogeneous droplet nucleation in a supersaturated vapor within the body of the gas-vapor mixture inside the cavity.
2. Heterogeneous droplet nucleation.
3. Liquid film condensation on the rather cold surfaces of the cavity interior.

The three fundamental problems have been addressed in this report.

a) In the case of the first problem it is clear from the above discussion that it is possible for a vapor to be in a highly supersaturated state without condensation occurring. This behavior can play a major role in many circumstances of practical interest, including cloud (fog) formation and precipitation in ICF reaction chambers during rapid expansion of liquid metal-gas mixtures.

b) Addressing the second problem, it is quite possible for a thin microfilm of liquid to be absorbed on all or part of a solid surface. This is particularly true for high-energy surfaces such as metals. In addition, when water is the liquid, its polar nature can enhance the tendency of water molecules to attach to portions of the solid surface. (Many oxides and corrosion-produced compounds on metallic surfaces are hydrophilic.) Patches of adsorbed liquid molecules on the solid surface can thus serve as nuclei for condensation of the liquid phase when the vapor is supersaturated. Condensation on the surface can begin as the formation of very small droplets on the surface at the sites of these nuclei. This so-called dropwise condensation process is, in fact, commonly observed when water vapor in air condenses on a cold beverage glass. This is usually interpreted as being a direct consequence of the fact that the liquid poorly wets the glass, except at nuclei locations where water molecules have adsorbed to crevices (scratches) or foreign matter (such as dust particles) on the surface.

c) For the third problem, dropwise condensation may occur on a solid surface cooled below the saturation temperature of a surrounding vapor when the surface is poorly wetted except at locations where well-wetted contaminant nuclei exist. The poorly wetted surface condition can result from contamination or coating of the surface with a substance that is poorly wetted by the liquid phase of the surrounding vapor. In practice, this can be achieved for liquid metal condensation by permanently coating the surface with a low surface-energy polymer or a noble metal. This method of promoting dropwise condensation is of particular interest because it holds the prospect of providing continuous dropwise condensation. Dropwise condensation is generally the preferred mode of condensation because the resulting

heat transfer coefficient may be as much as an order of magnitude higher than that for film condensation under comparable circumstances.

d) Some other factors affecting condensation:

i) Nucleation of droplets on gaseous ions: This very important case was first investigated by Thomson who showed that vapor molecules form stable clusters about all gaseous ions. The analysis showed that even at zero supersaturation the ion is surrounded by a stable shell of vapor molecules. Of course, a finite supersaturation ratio $(P_l/P_e) > 1$ is required for nucleation of macroscopic droplets.

ii) Nucleation of droplets on foreign particles of subcritical size. The presence of vapor impurities like dust, bring about nucleation of droplets and fog formation even though the vapor is unsaturated with respect to pure material. It is understood that this phenomenon is due to their effects in greatly lowering the vapor pressure P_e, giving rise to a large negative Gibbs free energy of formation of a critical cluster. Also, the presence of vapor-immiscible impurities enhances the nucleation rate because of their effect in reducing the surface tension by adsorption.

REFERENCES

1. P. G. Hill, H. Witting, and E. P. Demetri, "Condensation of Metal Vapors During Rapid Expansion," J. of Heat Transfer, Nov. 1963, pp. 303-317.

2. D. J. Frurip and S. H. Bauer, "Homogeneous Nucleation in Metal Vapors. 3. Temperature Dependence of the Critical Supersaturation Ratio for Iron, Lead, and Bismuth," The Journal of Physical Chemistry, 81(10) (1977).

3. Louis C. Burmeister, "Convective Heat Transfer," John Wiley & Sons, New York, 1983, pp. 678.

4. D. M. Woodruff, and J. W. Westwater, "Steam Condensation on Various Gold Surfaces," J. Heat Transfer, 103, 685-692 (1981).

5. G. A. O'Neil and J. W. Westwater, "Dropwise Condensation of Steam on Electroplated Silver Surfaces," Int. J. Heat Mass Transfer, 27, 1539-1549 (1984).

6. E. Gose, A. N. Mucciordi, and E. Bear, "Model for Dropwise Condensation on Randomly Distributed Sites," Int. J. Heat Mass Transfer, 10, 15-22 (1967).

7. A. C. Peterson, and J. W. Westwater, "Dropwise Condensation of Ethylene Glycol," Chem. Eng. Prog. Symp. Ser., 62(64), 135-142 (1966).

8. H. Merte, "Condensation Heat Transfer," Adv. Heat Transfer, 9, 181-272 (1973).

9. B. Badger, et al. "LIBRA-SP, A Light Ion Fusion Power Reactor Design Study Utilizing a Self-Pinched Mode of Ion Propagation," University of Wisconsin Fusion Technology Institute Report UWFDM-982.